Directed Assembly of Hybrid Colloids for Optics

Rajam Elancheliyan

université de BORDEAUX

THÈSE PRÈSENTÉE POUR OBTENIR LE GRADE DE

DOCTEUR DE L'UNIVERSITÉ DE BORDEAUX

l'ÉCOLE DOCTORALE DES SCIENCES CHIMIQUES

Spécialité doctorale "Physico-Chimie de la Matière Condensée"

présentée et soutenue publiquement par

Rajam Elancheliyan

le 9 Octobre 2020

Directed Assembly of Hybrid Colloids for Optics

Devant le jury :

Sébastien Bidault,	Chargé de Recherche	Rapporteur
Fabienne Gauffre,	Directrice de Recherche	Examinatrice
Brigitte Pansu,	Professeure	Rapportrice
Cécile Zakri,	Professeure	Examinatrice
Olivier Mondain-Monval,	Professeur	Directeur de Thèse
Virginie Ponsinet,	Directrice de Recherche	Directrice de Thèse

UNIVERSITÉ DE BORDEAUX
CNRS, Centre de Recherche Paul Pascal (CRPP)
UMR 5031, 33600 Pessac, France

Directed Assembly of Hybrid Colloids for Optics

Thesis presented by,
Rajam Elancheliyan

Thesis Director
Olivier Mondain-Monval
Virginie Ponsinet

Université de Bordeaux
Sciences et technologies
351 cours de la Libération CS 10004
33 405 Talence CEDEX, France

Unité de recherche:
Centre de Recherche Paul Pascal (CRPP)
UMR5031, CNRS & Université de Bordeaux
115 Avenue du Dr Albert Schweitzer,
33600, PESSAC, France

ACKNOWLEDGEMENT

This Ph.D. thesis is the result of a challenging journey and it could not have been accomplished if not for the assistance, patience and support of many individuals. At the end of this journey, it is a pleasant task to express my thanks to all those people who made this thesis possible and an unforgettable experience for me.

First and foremost, I would like to express my gratitude to my thesis supervisors **Olivier Mondain Monval** and **Virginie Ponsinet** for mentoring me over the course of my PhD. Thank you for giving me an opportunity to be a part of the METAMAT group. You have helped me through extremely difficult times over the course of the analysis and the writing of the dissertation and for that I sincerely thank you for your confidence in me. Thank you for always being very patient with me and providing me with a very positive working environment.

I would then like to extend my gratitude to Philippe Barois and Alex Baron for their support and guidance especially in the optical analysis part. I would also like to extend my appreciation to all the members of the METAMAT group for welcoming me into their group and supporting me during the last three years. I truly enjoyed all the METAMAT group meetings not only due to the delicious cakes but also because of all the insightful discussions and suggestions.

During this thesis work, I also had the opportunity to collaborate with the Soft Micro Systems group to perform the microfluidic experiments and I would like to thank Jean Christophe Baret and Thomas Beneyton for their help with these experiments.

I would like to thank Mona Tréguer-Delapierre and Glenna L. Drisko for guiding me through the course of my PhD. Your constant encouragement and scientific advice have helped me progress further in my PhD.

I would like to thank Ahmed Bentaleb for his help on small angle X-rays scattering. Thanks to Einat Nativ-Roth and Oren Regev for performing the CRYO-TEM experiments. Thanks to Sabine Castino for helping me with the IR meansurements and analysis.

Huge thanks to all my friends in CRPP, for the moments we spent together, not only in the working environment but also in our leisure time. Thanks to Maeva Riegert and Manu Picheau for helping me with all the administrative procedures. Thank you Simone Oldenburg for being such a good friend and also for putting up with me being late all the time.

Finally I would like to extend my deepest gratitude to my parents Elancheliyan Sengotavellu and Barathi Elancheliyan without whose love and support I could never have completed this doctoral degree. You have put up with me being distracted and distant for the past three years and I'm very grateful for your patience and understanding. Thank you for always believing in me, I never would have made it otherwise.

Abstract

Keywords: *Metasurface, Optical Resonators, Emulsions, Huygens Scatterers.*

Optical metamaterials are artificially structured materials engineered to exhibit extraordinary electromagnetic properties which are not accessible to naturally occurring materials. Metamaterials are typically composed of an assembly of repeating units called 'meta-atoms' or 'resonators'. These artificial structures have the capability to control the light propagation by tuning the amplitude, the phase and/or the polarization of the propagating beam. Resonators can also be arranged into thin sub-wavelength layers to create a metasurface (MS), which is a two dimensional analog of a 3D metamaterial. Due to their miniaturized size, MS have the advantage to diminish losses and can be incorporated into nanophotonic systems. The optical functionalities of MS depend upon the structural parameters of the resonators. With the help of simulations, different designs for the resonators have been proposed and also experimentally realized.

Simulations performed within the *Metamaterials* group at CRPP have shown that an assembly of N gold nanoparticles (NPs), of diameter d_{NP} distributed quasi-homogeneously within a spherical volume of radius R of a so called NP-cluster, can potentially be used to create 'Huygens MS'. The functioning of such devices are based on the Huygens-Fresnel principle and can be used to achieve directional scattering properties. The main objective of this thesis is to establish an experimental method to produce these clusters and to study their optical properties.

This thesis can be divided into two main parts. In the first part, we detail the fabrication technique which was used to synthesize clusters made of gold nanoparticles. The technique involved emulsifying a suspension of gold nanoparticles in water into an oil phase using adapted surfactants. This step is followed by the controlled evaporation of the water from the droplets under low pressure. The surface of the gold nanoparticles were previously functionalized in order to retain their surface plasmon resonance properties in the final assembly. The control over the size of this grafted layer provided an additional lever to control the structure of the clusters, investigated using small angle x-ray scattering (SAXS), and more particularly their internal gold volume fraction f. Both the values of f and of the cluster radius R are shown to strongly influence their resulting optical properties. Doing so, we synthesized clusters with radius around 100 nm, and varied their volume fraction f from roughly 20 to 50%. The structures of these clusters are also investigated using both transmission electron microscopy and cryogenic transmission electron microscopy.

Attempts to achieve a better control of the initial emulsions size and size distributions

using microfluidics are also presented in the manuscript. However this method suffers from many technical difficulties which were not all overcome during this thesis.

The second part of the thesis focuses on developing a variable angle polarization resolved static light scattering setup to study both the spectral and angular scattering properties of suspensions of the synthesized clusters. The data measured using this setup was analysed and also compared to theoretical calculations and simulations. The influence of the size R and the volume fraction f of the clusters on their scattering properties were experimentally measured and compare qualitatively well with simulations. The presence of electric and magnetic multipoles and their contribution to the scattering properties are experimentally demonstrated. We also show that the synthesized clusters with radius $\approx$ 120 nm and volume fraction ≥ 0.3 exhibit exceptional directional scattering properties.

Résumé

Mots-clés: *Métasurface, Résonateurs optiques, Émulsions, Diffuseurs de Huygens.*

Les métamatériaux optiques sont des matériaux structurés artificiellement qui présentent des propriétés électromagnétiques extraordinaires qui ne sont pas accessibles aux matériaux naturels. Les métamatériaux sont généralement composés d'un assemblage de petites unités appelées 'méta-atomes' ou 'résonateurs'. Ces structures artificielles permettent de piloter la propagation de la lumière en modifiant, de façon contrôlée, l'amplitude, la phase et/ou la polarisation du faisceau incident. Les résonateurs peuvent également être disposés en couches minces, c'est-à-dire de taille 'sub-longueur d'onde', pour former ce que l'on appelle alors une métasurface (MS). Il s'agit ainsi d'un analogue bidimensionnel d'un métamatériau 3D. En raison de leur très faible épaisseur, les pertes, inhérentes à tous phénomènes de résonances, y sont très limitées et ces structures peuvent être miniaturisées et incorporées dans des systèmes nanophotoniques. Les fonctionnalités optiques des MS dépendent des paramètres structurels des résonateurs. À l'aide de simulations numériques, des résonateurs de différentes structures internes ont été proposés et réalisés expérimentalement.

Ainsi, des simulations réalisées au sein du groupe *Métamatériaux* du CRPP ont montré qu'un assemblage de N nanoparticules d'or (NPs), de diamètre d_{NP} distribuées de manière quasi homogène dans un volume sphérique de rayon R, appelé par la suite 'clusters', peut potentiellement être utilisé pour créer ce que l'on appelle des 'MS de Huygens'. Le fonctionnement de tels dispositifs est basé sur le principe de Huygens-Fresnel et peut être utilisé pour obtenir des propriétés de diffusion directionnelle. L'objectif principal de cette thèse est d'établir une méthode expérimentale pour produire ces clusters et d'étudier leurs propriétés optiques.

Cette thèse peut être divisée en deux parties principales. Dans une première partie, nous détaillons la technique de fabrication qui a été utilisée pour synthétiser ces clusters de nanoparticules d'or. La technique consistait à émulsionner une suspension de nanoparticules d'or dans l'eau dans une phase huileuse à l'aide de tensioactifs adaptés. Cette étape est suivie de l'évaporation contrôlée de l'eau des gouttelettes sous basse pression. La surface des nanoparticules d'or a été préalablement fonctionnalisée afin de conserver leurs propriétés de résonance plasmonique de surface dans l'assemblage final. Le contrôle de la taille de cette couche greffée s'est avéré ensuite constituer un levier supplémentaire pour contrôler la structure des clusters, étudiée par diffusion des rayons X aux petits angles (SAXS), et plus particulièrement leur fraction volumique interne en or f. Ainsi, nous avons montré que les valeurs de f et du rayon R des clusters influencent fortement leurs propriétés optiques résultantes. Ce faisant, nous avons synthétisé des

clusters de rayon environ égal à 100 nm et de fraction volumique f comprise entre environ 20 et 50 %. Les structures de ces clusters ont été également étudiées en utilisant à la fois la microscopie électronique à transmission et la cryo-microscopie électronique à transmission.

Des tentatives pour obtenir un meilleur contrôle de la taille et de la distribution en taille des émulsions initiales, réalisées en microfluidique, sont également présentées dans le manuscrit. Malheureusement, les nombreuses difficultés rencontrées lors de l'utilisation de cette technique n'ont pas pu être surmontées au cours de cette thèse.

Dans la deuxième partie de la thèse, nous avons développé et utilisé un montage de diffusion statique de la lumière à angle variable pour étudier à la fois les propriétés de diffusion spectrale et angulaire des dispersions de clusters synthétisés. Les données obtenues ont été analysées et comparées à des calculs théoriques et des simulations. L'influence de la taille R et de la fraction volumique f des clusters sur leurs propriétés de diffusion a été mesurée expérimentalement et se les résultats obtenues sont qualitativement bien décrits par les simulations numéraiques. La présence de multipôles électriques et magnétiques et leur contribution aux propriétés de diffusion sont démontrées expérimentalement. Nous montrons également que les clusters synthétisés de rayon $\approx$ 120 nm et de fraction volumique $\geq$ 0,3 présentent des propriétés de diffusion directionnelle.

Contents

Liste of figures

List of Tables

General introduction

Contents

Summary: In this introductory chapter we first briefly discuss on the concept of metamaterials and metasurfaces. We then describe the structure and outline of this thesis.

0.1 Introduction

Nanophotonics, a branch dedicated to study the behaviour of light when it interacts with matter on the nanometer scale, has garnered a lot of attention due to its capability to manipulate light in the subwavelength regime. It offers a wide scope of applications in imaging, sensing, photodetection, lighting and displays, communications, opto-electronics, etc.

A new branch of nanophotonics dedicated to metamaterials (MMs) has seen many developments in the recent years. MMs are artificial materials composed of repeating units of nanostructures called meta-atoms organized in a matrix. The fundamental properties of MMs involve the manipulation of light propagation by controlling both the electric and magnetic responses of a material to light. Although the electric response of a material to light is ubiquitous, the magnetic response is negligible in natural materials. That is, at optical frequencies, the magnetic permeability (μ) of all natural materials is set to $\mu = 1$. Artificial materials, which can present a strong magnetic response to the electromagnetic radiation, are interesting to increase the capability of light modulation. The presence of a magnetic polarizability in addition to the electric, indeed paves the way to many groundbreaking electromagnetic phenomena such as negative refractive index, invisibility cloaking, perfect absorption, artificial chirality... etc, which are not available with conventional and natural materials.

Although many promising applications may emerge from this concept, optical MMs are challenging, time consuming and often expensive, to produce at large scales due to their structural complexity and nanometer lengthscales, that require 3D high-tech nanofabrication methods. Moreover, they usually present high dissipation losses, making it impractical for light to propagate through a bulk portion of the MMs.

Metasurfaces (MSs) are the two dimensional analogs of MMs and, due to their subwavelength thickness, exhibit much less dissipation losses. MSs are built by arranging nanostructures termed as nanoresonators or meta-atoms onto a thin, sub-wavelength layer. Both top-down and bottom up techniques have been used to build such structures. Top-down fabrication methods, such as lithography and nanoprinting have been successfully implemented to fabricate MSs. However, if these techniques allow for the realization of experimental devices with a very high degree of precision in their structure, they also present the important drawback of being both rather expensive and time consuming, which precludes the fabrication of large areas of materials. Thus, the bottom-up approach based on wet-chemistry and self-assembly processes do present a good alternative for the fabrication of MSs. MSs can thus be used to overcome the challenges of a large volume MMs and allow optical funtionalities that are difficult to attain with conventional optical devices.

The optical functionalities attained using MSs depend upon the geometrical param-

eters such as shape, size as well as the distance between its building units (meta-atoms). Different designs of meta-atoms have been proposed with the help of simulations. Some of these designs have been successfully produced using wet-chemistry processes. These designs include plasmonic raspberries [1], plasmonic dodecapods [2], high refractive index materials such as silicon nanoparticles [3] etc. These structures demonstrated low to moderate magnetic response to the electromagnetic wave.

0.2 Aim and structure of the thesis

0.2.1 Motivation

The above mentioned optical resonators, although possessing a large magnetic response to the electromagnetic wave, are difficult to fabricate and requires multiple steps to yield very few objects. In this thesis work, we aim to establish a fabrication technique capable of producing larger quantities of resonators which can potentially be used to build MSs.

In this project, we were interested in fabricating resonators which can further be used to build what is called a "Huygens MS". The functioning of Huygens MSs is based on the Huygens-Fresnel principle which states that every point in space that receives an electromagnetic wave becomes a secondary source for the outgoing waves. Analogous to the Huygens concept, each resonator on a Huygens metasurface will scatter the incident wave forward and thus act as a secondary source of wavelets. The new wavefront is the combination of all the secondary wavelets and therefore by engineering the resonators phase response, one can manipulate the phase of new wavefronts. These resonators, therefore will have the potential to give rise to directional scattering properties.

For this purpose a new design of meta-atoms consisting of NP clusters proposed by Rockstuhl *et al.* [4] and Dezert *et al.* [5] was considered. The design proposed by Dezert *et al.* ([5]) consists in an assembly of N nanoparticles (NPs) of diameter d_{NP} distributed quasi-homogeneously within the spherical volume of radius R of a so-called NP-cluster. The study showed that interesting optical properties are obtained if the constituting NPs are either plasmonic (metallic NPs) or of a high refractive index (silicon or titanium dioxide for instance). In such cases, the optical index of the NP clusters can be tailored by varying the cluster filling fraction $f = \mathrm{N}(d_{\mathrm{NP}}/2\mathrm{R})^3$.

Assembly of NPs into dense clusters has been achieved using different colloidal assembly routes such as block copolymer self assembly [6], hydrophobic interactions [7] for example. In this project, we choose to use an inverse emulsion ripening process via dehydration of water droplets containing gold NPs, to produce these clusters in large quantity.

0.2.2 Thesis outline

The aim of this PhD project was therefore to synthesize these gold NP clusters and to study their optical properties using a polarization resolved static light scattering technique.

The detailed outline of each chapter are given below:

- **Chapter 1:** In this chapter we first aim to provide a complete understanding of the electromagnetic properties of different materials, starting with the optical properties of bulk matter and later on optical properties of nanomaterials. We also elaborate on the potential influence of metamaterials and metasurfaces in the field of optics. This chapter also aims at providing a detailed bibliographic study on different resonators, their fabrication and the optical characterization techniques employed to study their optical properties.

- **Chapter 2:** The aim of this chapter is to introduce all the experimental techniques and provide a brief background on the analytical tools used to characterize the suspension of resonators. We also provide a detailed description of the analytical techniques used to characterize all the samples. Finally, we introduce the fabrication technique employed to synthesize the resonators.

- **Chapter 3:** This chapter provides a detailed description of the formulation route employed to synthesize clusters of gold nanoparticles. The first part of this chapter focuses on the bulk emulsion formulation and the ripening of water droplets to form the final clusters. We also detail on the different parameters that influence the structure of the gold NP clusters. The influence of different experimental parameter on the cluster structure is shown using SAXS and electron microscopy. In the second part of this chapter, we detail on the droplet based microfluidic technique used to produce monodisperse emulsion.

- **Chapter 4:** This chapter is dedicated to the study of optical properties of the synthesized clusters. We first introduce the experimental setup used to study the optical property. We then show the influence of the cluster structure on their optical properties. This chapter also attempts to compare the experimental and simulation data.

- **General conclusion and prospects:** In this conclusion we summarize the main results and achievements of this thesis and highlight possible research directions that would be worth exploring in the future.

0.3 Reference

[1] V. Ponsinet, P. Barois, S. M. Gali, P. Richetti, J.-B. Salmon, A. Vallecchi, M. Albani, A. Le Beulze, S. Gomez-Grana, E. Duguet, *et al.*, "Resonant isotropic optical mag-

netism of plasmonic nanoclusters in visible light," *Physical Review B*, vol. 92, no. 22, p. 220414, 2015. 3

[2] V. Many, R. Dézert, E. Duguet, A. Baron, V. Jangid, V. Ponsinet, S. Ravaine, P. Richetti, P. Barois, and M. Tréguer-Delapierre, "High optical magnetism of dodecahedral plasmonic meta-atoms," *Nanophotonics*, vol. 8, no. 4, pp. 549–558, 2019. 3

[3] M. L. De Marco, S. Semlali, B. A. Korgel, P. Barois, G. L. Drisko, and C. Aymonier, "Silicon-based dielectric metamaterials: Focus on the current synthetic challenges," *Angewandte Chemie International Edition*, vol. 57, no. 17, pp. 4478–4498, 2018. 3

[4] C. Rockstuhl, F. Lederer, C. Etrich, T. Pertsch, and T. Scharf, "Design of an artificial three-dimensional composite metamaterial with magnetic resonances in the visible range of the electromagnetic spectrum," *Physical review letters*, vol. 99, no. 1, p. 017401, 2007. 3

[5] R. Dezert, P. Richetti, and A. Baron, "Isotropic huygens dipoles and multipoles with colloidal particles," *Physical Review B*, vol. 96, no. 18, p. 180201, 2017. 3

[6] C. Durand-Gasselin, N. Sanson, and N. Lequeux, "Reversible controlled assembly of thermosensitive polymer-coated gold nanoparticles," *Langmuir*, vol. 27, no. 20, pp. 12329–12335, 2011. 3

[7] A. Sánchez-Iglesias, M. Grzelczak, T. Altantzis, B. Goris, J. Perez-Juste, S. Bals, G. Van Tendeloo, S. H. Donaldson Jr, B. F. Chmelka, J. N. Israelachvili, *et al.*, "Hydrophobic interactions modulate self-assembly of nanoparticles," *ACS nano*, vol. 6, no. 12, pp. 11059–11065, 2012. 3

Chapter 1

State of the Art

Contents

Summary: The aim of this chapter is to introduce basic optical concepts of materials and further elaborate on the emergence of optical metamaterials and metasurfaces. This chapter also provides a brief summary on fabrication of different materials to create a metasurface and discusses the different methods that have been employed in the literature to study their optical properties.

1.1 Optical Properties of Materials

1.1.1 Optical properties of bulk materials

The optical properties of a material define its response to light in terms of propagation and absorption. The interaction between light, which is composed of an oscillating electromagnetic field (EM), and matter is dominated by forces exerted by the incident electric (and magnetic) field on the electric charges of the atoms of the materials. The interaction and propagation of electromagnetic radiation within matter is macroscopically described by Maxwell's equation, a set of four equations postulated by James Clerk Maxwell, which defines the spatial and temporal characteristics of electric and magnetic fields. Maxwell's Equations for EM fields in matter are shown below:

$$\nabla \times \mathbf{E} = -\frac{\partial \mathbf{B}}{\partial t} \qquad \text{(Faraday's law of induction)} \tag{1.1a}$$

$$\nabla.\mathbf{B} = 0 \qquad \text{(Gauss' law of magnetism)} \tag{1.1b}$$

$$\nabla.\mathbf{D} = \rho \qquad \text{(Gauss' law of electricity)} \tag{1.1c}$$

$$\nabla \times \mathbf{B} = \mathbf{J} + \frac{\partial \mathbf{D}}{\partial t} \qquad \text{(Ampere's law)} \tag{1.1d}$$

These equations describe the interrelationships between fields, source and material properties. The first two equations (1.1a) and (1.1b) are structural equations of the EM field and the last two equations (1.1c) and (1.1d) connect the fields to fixed or mobile charges. Here, **E**, **B**, ρ and **J** denotes the electric field [V.m^{-1}], magnetic flux density [T], electric charge density [C.m^{-3}] and the electric current density [A.m^{-2}] respectively. **D** and **H** are electric displacement [C.m^{-2}] and magnetic field strength [A.m^{-1}], they describe the polarization of the material in response to **E** and **B** respectively. Hence, Maxwell's equation establishes a connection between **E** and **B**.

The electric component of the EM wave displaces the electrons in an atom (in case of bound electrons) to form an electric dipole which oscillates with the same frequency as the incident field. Therefore each atom becomes an electric dipole with a dipole moment 'p'. These dipole moments scatter light in all directions and the scattered light depends upon the shape, size and composition of the irradiated material [1]. The dipole moments add up to create a macroscopic net polarization **'P'** which is defined as the average dipole moment per unit volume. The relation between **P** and **E** is given by Equation 1.2

$$\mathbf{P} = \epsilon_o \, \chi_e \, \mathbf{E} \tag{1.2}$$

where, ϵ_o is a fundamental constant known as permittivity of vacuum (ϵ_o = 8.854 × 10^{-12} F$m.^{-1}$) and χ_e is a dimensionless proportionality constant known as electric sus-

ceptibility of matter. The electric polarization contributes to the electric displacement as expressed in Equation 1.3.

$$\mathbf{D} = \epsilon_o \mathbf{E} + \mathbf{P} = \epsilon_o (1 + \chi_e) \mathbf{E} \tag{1.3}$$

This defines the dielectric constant ϵ of the bulk matter as:

$$\epsilon = 1 + \chi_e \tag{1.4}$$

ϵ and χ_e are constant values for any bulk material under consideration. In the presence of free electrons in the bulk material (for example metals), **E** causes additional electric current with current density J_c, which is defined as shown below:

$$J_c = \sigma \, \mathbf{E} \tag{1.5}$$

where J_c and σ represents current density due to conduction electrons and conductivity $[S/m]$ of the material respectively.

Similarly to the electric field **E**, the magnetic field **H** induces magnetic dipole in the bulk matter resulting in the magnetic polarization **'M'** which can be defined as the average magnetic moment per unit volume. The **M** contributes to the magnetic flux density as shown in Equation 1.6.

$$\mathbf{B} = \mu_o \, \mathbf{M} + \mu_o \, \mathbf{H} = \mu_o \, (1 + \chi_m) \, \mathbf{H} = \mu \, \mu_o \, \mathbf{H} \tag{1.6}$$

where, μ_o is once again a fundamental constant known as permeablity of vacuum with $\mu_o \approx 4\pi 10^{-7} [H.m^{-1}]$, χ_m is the magnetic susceptibility and μ is the relative permeability of the bulk material. However, unlike the electric dipoles, at frequencies ranging from far-infrared to infinity, the induced magnetic dipoles are too inert to follow the oscillating magnetic field of the incident EM wave, hence all conventional materials do not exhibit a scattering magnetic dipole in the above mentioned spectral range. Thus, the relative permeability of bulk matter at optical frequency can be assumed to be $\mu = 1$ [2]

The electromagnetic phenomena are thus dependent on the fundamental properties (ϵ and μ) of the bulk material in consideration. Therefore it is essential to study the basic physical properties of these materials to understand their optical behaviour. Bulk materials can be classified into three categories based on their resistivity or resistance to the flow of current. The first one concerns "dielectric materials" also called insulators and the second are conductors. Insulators do not have any free charge carriers, contrary to metals which are a conductors. There also exist a third category called semi-conductors. A classical way to distinguish these materials is to use the energy band theory as shown in Figure 1.1.

The band gap between the valence and conduction band represent the energy barrier

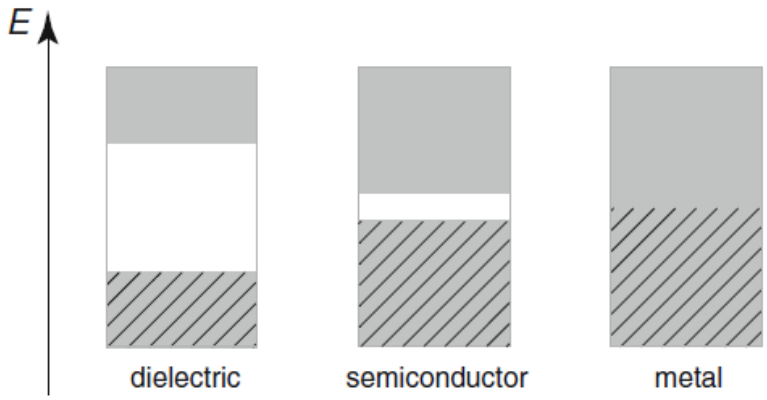

Figure 1.1: Energy band diagrams for different categories of materials. Shaded and light grey regions represent the valence and conduction band respectively [3].

that electrons must overcome to take part to the electric conduction process. In a dielectric material, the flow of current is prohibited due to the wide energy gap between the conduction and valence bands. The energy from the visible light of the optical spectrum is not sufficient enough to promote the transition of an electron from the valence band to the conduction band. Therefore, unless doped with dyes, they are in most cases transparent in the visible spectrum. The moderate gap in semiconductors makes it possible to promote an electron from the valence to conduction band with a small excitation energy. Finally, in the case of metals the two bands overlap and therefore free electrons can create a current flow.

The electronic structure of these materials cannot fully explain their optical properties. For example, Indium Tin Oxide, a metal-like material is optically transparent as would be a dielectric material. Therefore it is essential to look at other parameters to understand the optical properties of materials.

The light-matter interaction is defined by the complex refractive index ($\overline{n}(\omega)$) as shown in Equation 1.7

$$\overline{n}(\omega) = n'(\omega) + i\,n''(\omega) \tag{1.7}$$

where n' is the real part of the refractive index, which is defined as the ratio of the speed of light in vacuum ($C_o = 3.10^8\ m.s^{-1}$) to the speed of light in a given medium. n'' is the imaginary part of the refractive index and represents the absorption coefficient, also noted as 'κ', of the medium as the electromagnetic (EM) wave passes through it.

The refractive index of any material in turn, depends on the fundamental material property: electric permitivity (ϵ) and magnetic permeability (μ) through the following equation:

$$n = \sqrt{\epsilon\mu} \tag{1.8}$$

1.1.1.1 Optical properties of a dielectric medium

In optics, semiconductors are treated as dielectric materials and their band gap specify the shortest wavelength (critical wavelength (λ_c)) at which the dielectric remains transparent, meaning, that no electronic transition occurs below this wavelength. λ_c is related to the band gap energy (E_g) as shown in Equation 1.9

$$\lambda_c = \frac{hc}{E_g} = \frac{1.98644568 \times 10^{-25}\,\mathrm{J}.m}{E_g} \tag{1.9}$$

where h is the Planck constant [J.s] and c is the speed of light [m/s]. The interaction of light with dielectrics are again analyzed using Maxwell's equations (refer Equation: 1.1-1.6). Since $\chi_m \approx 0$ in any conventional material for reasons specified in Section 1.1.1, the refractive index most of the time reads as $n = \sqrt{\epsilon}$.

At optical frequencies, oscillation of the electric field is too fast for the bound charges in the molecules and therefore they do not follow the oscillation in time. Hence Equation 1.3 has to be modified to include the response to electric field at not only at time 't' but at all past time, which in Fourier space reads as:

$$\mathbf{D}(\omega) = \epsilon_o\, \epsilon(\omega)\, \mathbf{E}(\omega) = \epsilon_o\, [1 + \chi_e(\omega)]\, \mathbf{E}(\omega) \tag{1.10}$$

Where, $\epsilon(\omega)$ is the frequency dependent dielectric permittivity describing the wavelength dependent response of the dielectric material.

Due to the absence of free charge carriers in a dielectric material, they respond to electric field by locally displacing the bound charges relative to their lattice atoms. When the photon energy is below the band gap, the dielectric constant is real and positive thus making the refractive index purely real. This means that the loss of energy due to absorption in a dielectric medium is very low. When the photon energy is equal to the band gap energy, a resonance takes place and the permittivity may become negative. The $\epsilon(\omega)$ of a typical transparent dielectric material is plotted in Figure 1.2, where ω_1 corresponds to resonance due to lattice vibration and ω_2 is resonance due to the band gap. Below the IR regime, due to the absence of resonance, the dielectric medium has negligible loss. But at resonance (ω_1 and ω_2) the medium incurs losses due to absorption (which is materialised by the high values of $Im(\epsilon)$ at resonances, see Figure 1.2).

The square-root relationship between the refractive index and the permittivity still holds in the frequency domain.

$$n(\omega) = n'(\omega) + i n''(\omega) = \sqrt{\epsilon(\omega)} \tag{1.11}$$

The imaginary part of the refractive index n'' can be characterized using the absorption coefficient α which is obtained using Beer Lambert's law (shown in Equation 1.12). It states that the intensity of light I_o will decrease as it travels a distance z through the

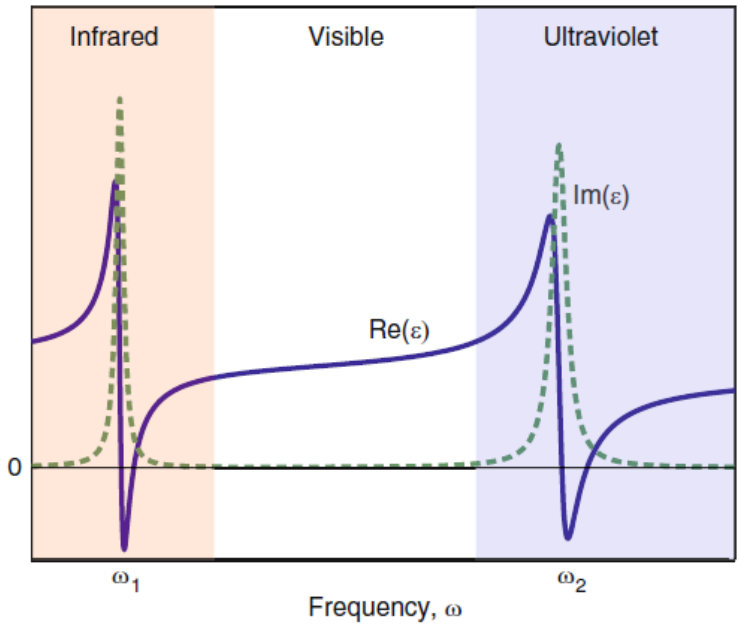

Figure 1.2: Real and imaginary part of a frequency dependent dielectric function [3].

medium:

$$I = I_o \exp(-\alpha z) \tag{1.12}$$

α is usually represented in the units of cm^{-1} and connected to n'' by the following equation:

$$\alpha = \frac{4\pi n''}{\lambda_o} \tag{1.13}$$

where λ_o is the wavelength of the incident light.

1.1.1.2 Optical properties of a Metal

Optical properties of metals are drastically different from the one of dielectrics due to two main characteristics. First, metals are opaque and secondly they are highly reflective. Metals are very commonly used for applications such as mirrors due to these properties. As explained before, unlike dielectric materials, metals have free charge carriers and therefore photon energy from any part of the electromagnetic spectrum is sufficient to excite these free electrons. This means that light from any part of the electromagnetic spectrum will be absorbed by metals.

The frequency dependent permittivity can once again be used to explain the optical behavior of metals and this can be expressed using a Lorentzian oscillator model as shown in Equation 1.14. The permittivity of metal due to the free electrons does not exhibit a resonance frequency as they are able to freely move in the metal lattice without any restoring forces, unlike the bound electrons which will exhibit a resonant behavior

similar to dielectrics. The permittivity of metals can thus be defined in terms of free and bound electrons.

$$\epsilon(\omega) = \epsilon_b(\omega) + \epsilon_f(\omega) \tag{1.14a}$$

$$\epsilon_b(\omega) = 1 + \frac{\rho_1^2}{\omega_o^2 - \omega^2 - i\,\gamma\,\omega} \tag{1.14b}$$

$$\epsilon_f(\omega) = 1 - \frac{\omega_p^2}{\omega^2 + i\,\omega\,\Gamma} \tag{1.14c}$$

where, the first term $\epsilon_b(\omega)$ represents the permitivity due to bound electrons in the metals and the second term $\epsilon_f(\omega)$ represents the free electrons. ω_p and ω_o represents the plasma frequency at which the density of the electron gas oscillates and resonance frequency of bound electrons. ρ_1, γ and Γ are the density of bound electrons, damping of bound electrons and damping constant of free electrons respectively. ω_p and Γ read:

$$\omega_p = \sqrt{\frac{n\,e^2}{\epsilon_o\,m}} \quad \text{and} \quad \Gamma = \frac{\nu_F}{l} \tag{1.15a}$$

where e is the electron charge [C], m is the electron mass $9.1 * 10^{-31}$Kg), n represents the density of free electrons [m^{-3}], ν_F is the Fermi velocity [m/s] and l is the mean free path [m] of the electrons.

As opposed to dielectric materials, which have a positive dielectric permitivity, the metals have a negative permitivity at optical frequency. This implies that the free electrons in metals oscillate out of phase with the incident electric field. Consequently, the imaginary part of the refractive index for metals at optical frequency is very high and the losses due to absorption in metals are also very high. The electromagnetic wave at optical frequencies thus get absorbed before they can penetrate through the material, this makes metals opaque in nature.

To summarize, the electromagnetic phenomena of any materials can be explained through their effective material properties, namely the relative dielectric permittivity (ϵ) and the relative magnetic permeability (μ). And this can be schematically representend as shown in Figure 1.3, which depicts the real parts of μ in the y-axis and the real parts of ϵ in the x-axis.

The first (top right) quadrant represents dielectric materials with both parameters being positive. The second (top left) quadrant represents metals with a negative ϵ (the electric field inside the material is in the opposite direction to the field outside the material).

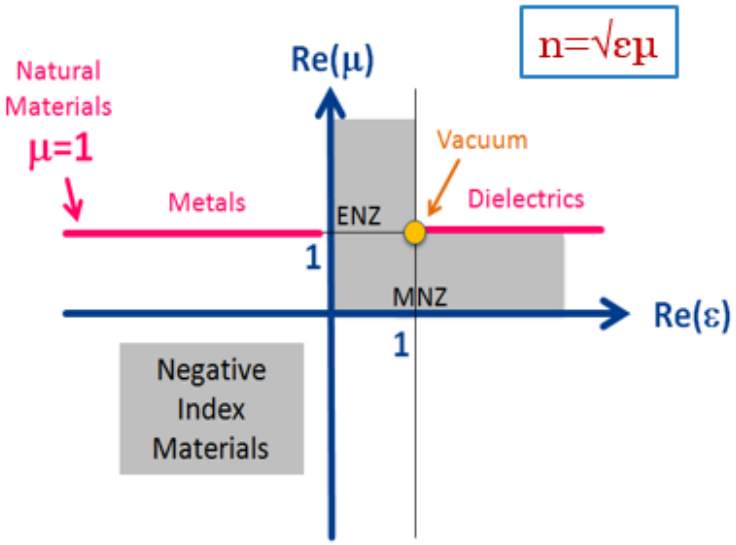

Figure 1.3: Representation of material parameters defining the optical properties of a material. Bold red line stands for natural materials.

Quadrant 4 (bottom right), where μ is negative and $\epsilon > 0$, means that the magnetic field inside the material is in opposite direction to that of field outside the material. The third quadrant (bottom left), where both parameters are negative, represents a class of materials known as negative index materials. When light encounters such a medium, the angle of refraction is negative at the interface

At optical frequency, conventional materials can be placed in the narrow region where μ=1 (bold line on Figure 1.3), thus largely reducing the attainable optical properties in bulk materials.

1.1.2 Optical resonances of nanoparticles and Mie theory

The transition from bulk materials to nanomaterials introduces many changes in the properties of material, this includes increase in mechanical strength, chemical selectivity etc, indicating that the size of an object plays a key role in almost all physical properties when brought down to less than 100 nm. In optics, the decrease in size of metallic materials leads to the resonant absorption of light. This phenomena also known as the surface plasmon resonances (SPR), schematically represented in Figure 1.4, occurs due to the collective excitation of the conduction electrons caused by the incident electromagnetic wave. Metallic nanoparticles (NPs) host a plasma made of its conduction electrons. This plasma can resonate around the particle with a natural frequency determined by particle parameters such as material, shape, size, and the dielectric nature of the surrounding environment. When a metallic NP is irradiated by EM waves, some energy is absorbed by the NPs as light causes oscillation of the electron cloud. The energy absorption is at its maximum when the frequency of the incoming light matches with the natural frequency

of the electron cloud. This collective absorption of light waves from NPs produces a color from the nanoparticle dispersion. This phenomena has also been widely used since the early medieval period by incorporating glasses with small inclusions of gold and silver NPs of different sizes to obtain various color.

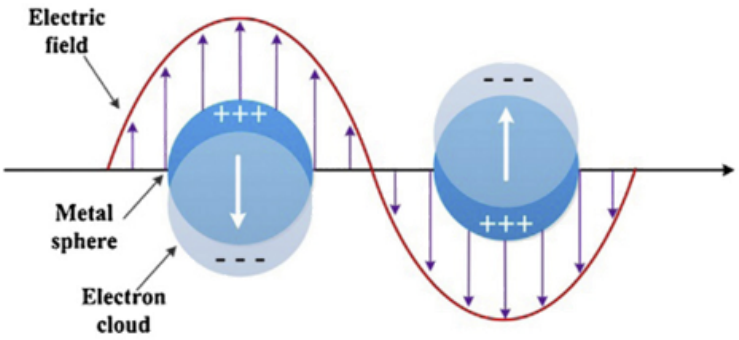

Figure 1.4: Schematic illustration of Surface plasmon resonance of metallic NPs.

The optical properties of nanoparticles depend on

- their size compared to the wavelength of the electromagnetic radiation,
- their shape,
- the chemical nature of the material and
- the optical material constants of both the NPs and their surrounding system.

The absorption spectra of gold NPs with varying size and shape is shown in Figure 1.5, the resonance peak, λ_{max}, characteristic of the size of the Au NPs, occurs when the light is in resonance with the surface plasmon oscillation leading to absorption. As the size of the NPs increases, a small red shift in λ_{max} of the absorption spectra can be observed, this is due to the change in the oscillation frequency. In case of anisotropic objects, such as nanorods, two resonance peaks can be observed, one due to the transverse and one due to the longitudinal oscillation of free electron with respect to the particles long axis. As the aspect ratio of the nanorods is increased, the longitudinal SPR increases.

Similarly, a shift in the λ_{max} is observed when the gold NPs are capped with different stabilizing agent such as Poly(vinylpyrrolidone) (PVP), Polyethylene-glycol (PEG-SH) etc. This shift is due to the change in the refractive index of the immediate surrounding of the NPs (Figure 1.6).

In the case of semiconductors, the decrease in size (typically in the nm range) leads to the quantum confinement of the electrons. When the size of the semiconductor is decreased (to the nm range), the charge carriers motion is confined thus increasing the

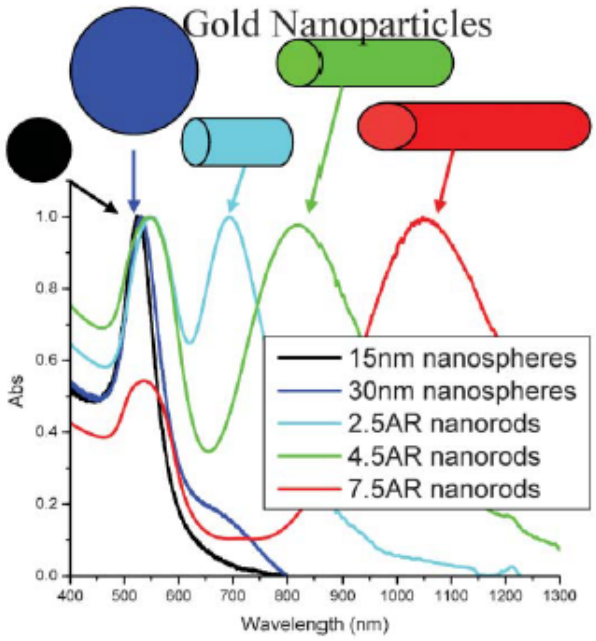

Figure 1.5: Absorption spectra of various size and shape of gold NPs. Adapted from reference [4].

bandgap of the material. Therefore the colour of the semiconducting NPs (which is a function of the bandgap) becomes largely dependent on the size and shape of the NPs.

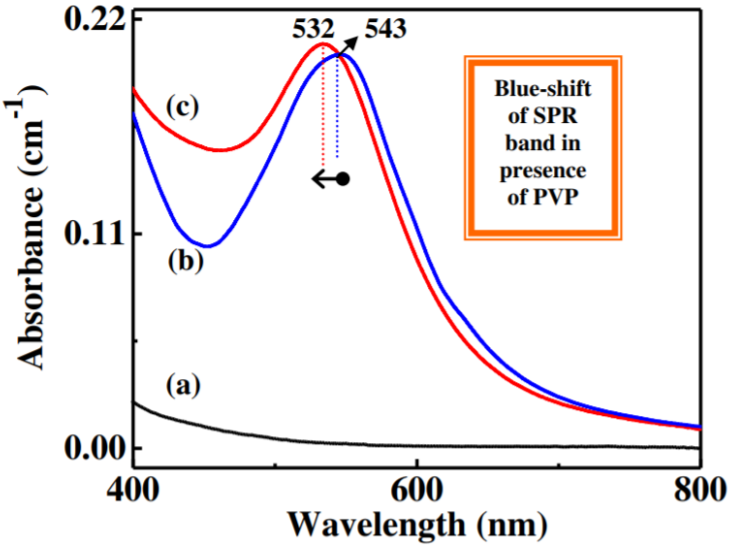

Figure 1.6: Absorption spectra of Au NPs capped with and without PVP [5].

The Optical properties of a colloidal suspension of NPs also depend on their concentration and aggregation state. A dilute NPs system is different from a densely packed one, as the increase in concentration leads to interaction between the NPs which alter their optical material constant of the surrounding environment. In a dense system of NPs, the particles are electromagnetically coupled and therefore each particle is not only excited by the external field but also by the scattered field of the neighboring particles, thus altering their absorption and extinction cross-section. The influence of the aggregation

state of NPs on their extinction cross-section has been studied by using UV-Visible spectroscopy [6]. It was found that the extinction peaks are strongly red-shifted in comparison with the single NP resonance. The red shift is mainly due to the electrostatic coupling between the NPs. This method has been used to characterize optical properties of clusters of NPs and will be further elaborated in Section 1.4.1.

The optical properties of NPs can be theoretically calculated by solving the Maxwell's equations (shown in Equation 1.1). This can be achieved by either using the Rayleigh scattering or the Mie scattering theories. Rayleigh scattering theory is applicable to particles with size much smaller than the wavelength of the incident light:

$$\frac{2\pi}{\lambda} \times d << 1 \tag{1.16}$$

where λ and d represent the wavelength and size of the particle respectively.

In the case of a spherical object, Mie theory can be used to calculate the absorption and extinction coefficient. Mie theory, named after Gustav Mie, provides a generalized solution to the Maxwell's equation describing the scattering of an electromagnetic wave by a homogeneous spherical particle suspended in a medium whose refractive index is different from the one of the particle. Unlike Rayleigh scattering, Mie scattering is applicable to spheres of all sizes, refractive indices and for radiation at all wavelengths. The Mie solution takes the form of an infinite series of multipole expansion of the polarization in a spherical medium due to an incident plane wave. The electric and magnetic field contribution of such polarization can also be expressed as an infinite series in which each element represents the contribution of one particular order of multipole expansion. The scattering (Q_s)and extinction (Q_e) efficiency of the particle can be expressed as:

$$Q_s = \sigma_s / \pi R^2 = \frac{2}{x^2} \sum (2n+1) \left[\left| a_n \right|^2 + \left| b_n \right|^2 \right] \tag{1.17a}$$

$$Q_e = \sigma_e / \pi R^2 = \frac{2}{x^2} \sum (2n+1) \left[Re(a_n) + Re(b_n) \right] \tag{1.17b}$$

where x represents the relative size of the particle to the incident wavelength:

$$x = (\frac{2\pi}{\lambda})(\frac{d}{2}) \tag{1.18}$$

where, σ_s, σ_e and πR^2 stands for the total scattering cross-section, the total extinction cross-section and the particle geometrical cross section respectively. n is the order of the multipole, with the coefficients a_n and b_n representing the electric and magnetic modes respectively. For instance, a_1 and b_1 are the coefficients of the electric (ED) and magnetic dipoles (MD) respectively and a_2 and b_2 are the coefficients for the electric(EQ) and magnetic quadrupoles (MQ) respectively. These coefficients are a function of the in-

cident wavelength, the relative refractive index of the particle n_p with respect to the one of the surrounding medium n_s, m ($m = \frac{n_p}{n_s}$), as described in Equation 1.19:

$$a_n = \frac{m\psi_n(mx)\psi'_n(x) - \psi_n(x)\psi'_n(mx)}{m\psi_n(mx)\xi'_n(x) - \xi_n(x)\psi'_n(mx)} \tag{1.19a}$$

$$b_n = \frac{\psi_n(mx)\psi'_n(x) - m\psi_n(x)\psi'_n(mx)}{\psi_n(mx)\xi'_n(x) - m\xi_n(x)\psi'_n(mx)} \tag{1.19b}$$

where, ψ and ξ are Riccati-Bessel function. n once again, defines the order of the multipole. As the relative refractive index m becomes equal to 1, all the coefficients vanish as if there was no particle in the medium. Mie theory can thus be used to predict the optical properties of spherical NPs in terms of each induced electric and magnetic multipole moment. Typically for any material with a refractive index 'n', the contribution from higher order multipoles occurs at shorter wavelengths whereas, the dipolar contribution occurs at longer wavelengths.

Thus, the interaction between the electromagnetic radiation and NPs leads to the occurrence of EM resonances. There are two possible resonances, which are : Plasmonic resonance and Mie resonance. The former occurs due to the presence of surface plasmons in metallic NPs. Mie resonance occurs due to the interaction of EM radiation and dielectric spheres with size comparable to the incident wavelength.

This thesis will focus mainly on the usage of plasmonic resonances of gold NPs to create metasurfaces.

1.2 Metamaterials and metasurfaces

In the past 20 years, a lot of efforts have been devoted to the theoretical and experimental study of optical metamaterials (MMs). The term metamaterial, constructed around the Greek prefix "meta", meaning "to go beyond", signifies materials with properties beyond those of conventional materials. MMs are thus artificially structured materials engineered to exhibit unconventional optical properties, which are not found in naturally occurring materials. It consists of an assembly of units organized in a matrix. Unlike natural materials, whose optical properties depend on their chemical composition, metamaterials inherit their optical properties from these structures. These elements are also known as "meta-atoms" or "resonators" and their size as well as the spacing between them must be small when compared to the wavelength of light to avoid any diffraction effects. These resonators strongly resonate with the incoming wave at a specific resonance frequency. This property can be due to the strong difference of optical index between the inclusion and the matrix (Mie resonance) or may also come from the Surface Plasmon Resonance (SPR)

of metallic nanoparticles composing the resonators. When there is a sufficient amount of resonators dispersed in the matrix, they can tune the response of the material to obtain some targeted electromagnetic properties. Therefore, MMs are not constrained by the electromagnetic response of natural materials and their composition, but by the nature, structure and size of the resonators. It is thus possible to obtain new electromagnetic functionalities using these meta-atoms, when dispersed in a matrix in sufficient amount.

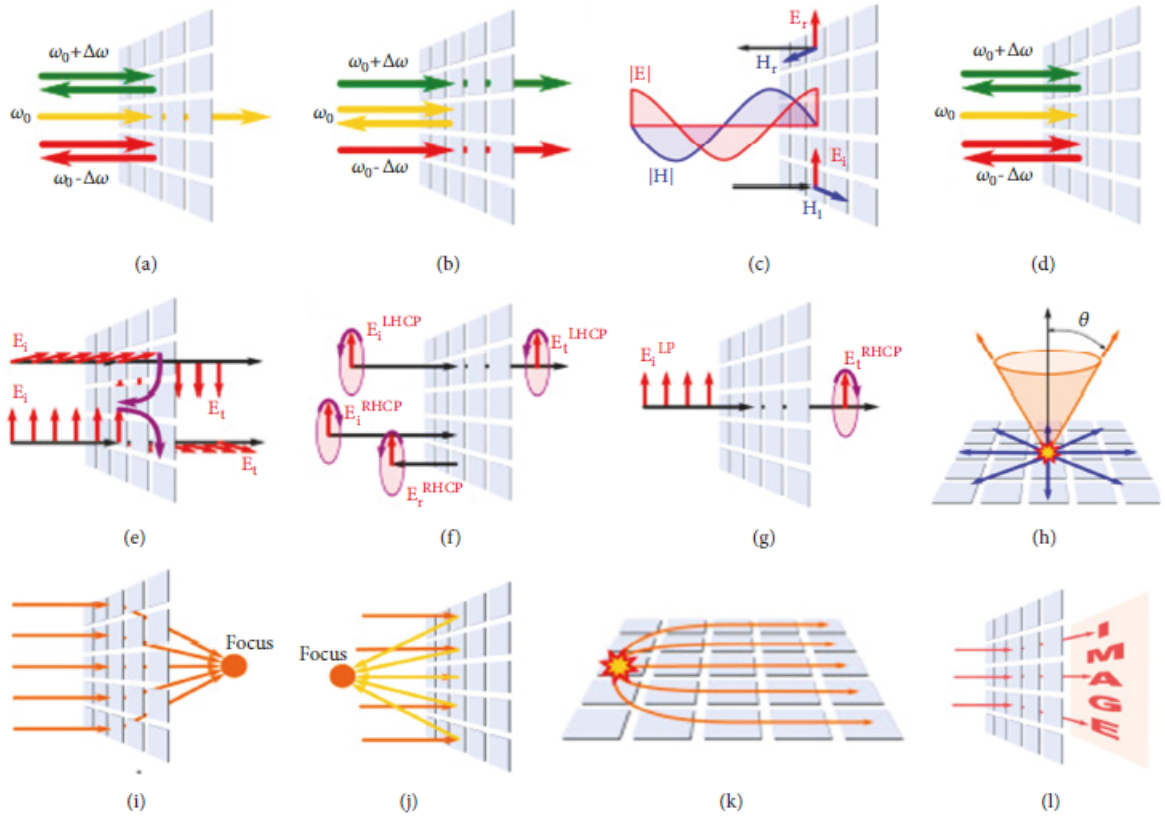

Figure 1.7: Application of MS (a) bandpass frequency selective surface; (b) bandstop frequency selective surface; (c) high-impedance surface; (d) narrowband perfect absorber; (e) twist polarizer; (f) right-handed circular-polarization frequency selective surface; (g) linear-to-circular polarization converter; (h) two-dimensional leaky-wave antenna with a conical-beam pattern; (i) focusing transmitarray; (j) focusing reflectarray; (k) flat Luneburg lens; (l) hologram [7].

Metamaterials thus provide a method to control the light matter interaction which can further be used to achieve groundbreaking electromagnetic properties, including negative refractive index [8], artificial chirality [9, 10], invisibility cloak [11]. It can be used to achieve a plethora of potential applications such as, sub-diffraction imaging [12], chemical and bio molecular sensing [13], communication and information processing [14]. MMs, although proven to have many interesting properties, face two main limitations, which prohibits their practical application. First, the fabrication of a micro-scale or nano-scale three-dimensional metamaterials often involves techniques such as lithography thus making them expensive and difficult to upscale. In addition, they present high intrinsic losses in the form of absorption as the EM wave propagates through the 3D structure.

On the other hand, Metasurfaces (MS), which are two dimensional analog of meta-

materials do not posses the same limitations as the 3D metamaterial. They consists of 2D assemblies of resonators and due to their extremely thin structure, MSs can easily be integrated in nanophotonics systems. They can thus be used to replace bulky optical components with flat optics.

The interaction of light with the nanoscale building blocks on a MS can be used to manipulate the polarization, spectrum, wavefront etc of an incident wave [15]. MS have been widely studied to obtain conventional functionalities such as lenses [16, 17], waveplates [18, 19], polarimeters [20, 21], beam deflectors [16, 22], holograms [23] etc. Schematic representations of some potential applications of MS are illustrated in Figure 1.7.

1.2.1 Huygens metasurface

A 2D array of resonators can be used to create a Huygens metasurface (HMSs), which can further be used to obtain uni-directional scattering surfaces. HMSs are based on Huygens Fresnel principle, developed by Christian Huygens in 1690 [24]. It is a well-known concept in electromagnetism and it provides a fundamental explanation to basic phenomenon such as reflection, refraction, diffraction and interference . It states that every point in space that receives an electromagnetic wave becomes a secondary source for the outgoing waves, therefore creating a gradual propagation of light (illustrated in Figure 1.8). Analogous to the Huygens concept, each resonator on a HMSs will scatter the incident wave and thus act as a secondary source of wavelets. The new wavefront is the combination of all the secondary wavelets and therefore by engineering the resonators phase response, one can manipulate the phase of new wavefronts.

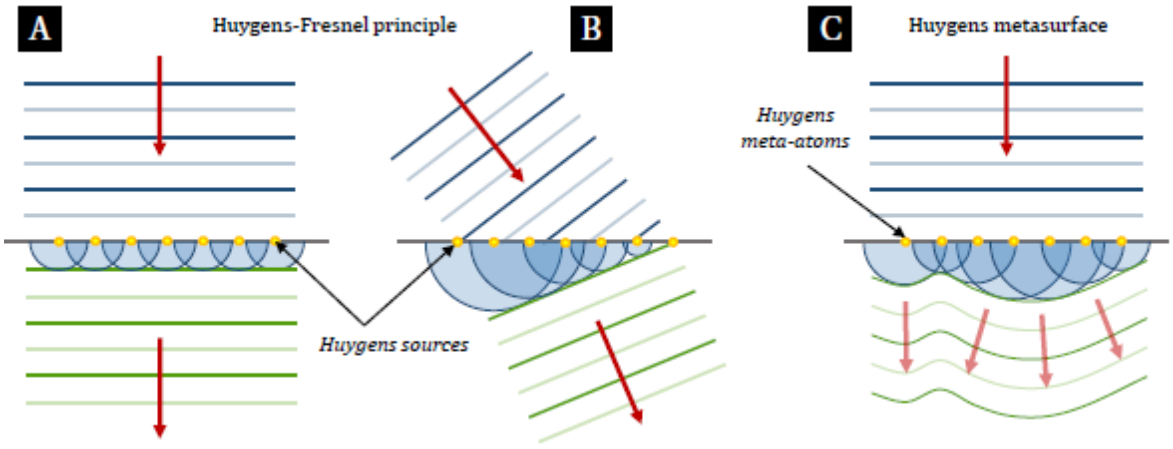

Figure 1.8: A) Illustration of the Huygens-Fresnel principle showing the gradual propagation of a plane wave through the excitation of secondary waves. B) Huygens-Fresnel principle applied to the refraction phenomenon. C) Illustration of the concept of Huygens metasurfaces. Assembling in a sub-wavelength array an ensemble of optical resonators exhibiting Huygens source features, it is possible to convert an incident plane wave into an arbitrarily shaped beam [25].

From Mie theory we know that, the electric field scattered by an arbitrary object can be

expressed in terms of multipolar expansion. The electromagnetic response of an object is thus the superposition of fields created by a set of simple point multipoles presenting well-known scattering patterns and properties. That is, the superposition of fields created by the multipoles define the scattering pattern of the object. Each multipole of a particular order exhibit a radiation pattern with a specific geometry. Dipoles present a toroidal radiation, with a zero in intensity along the excitation direction and a maximum isotropic radiation observed in the perpendicular plane. The quadrupoles exhibit a scattering mainly confined in four directions of space, while the octupoles show a scattering pattern with six lobes. Higher order multipoles exhibit a progressively increasing number of lobes, and as a result an angular distribution of the scattered intensity that increases in complexity. The radiation pattern of the dipoles and qudrupoles are shown in Figure: 1.9

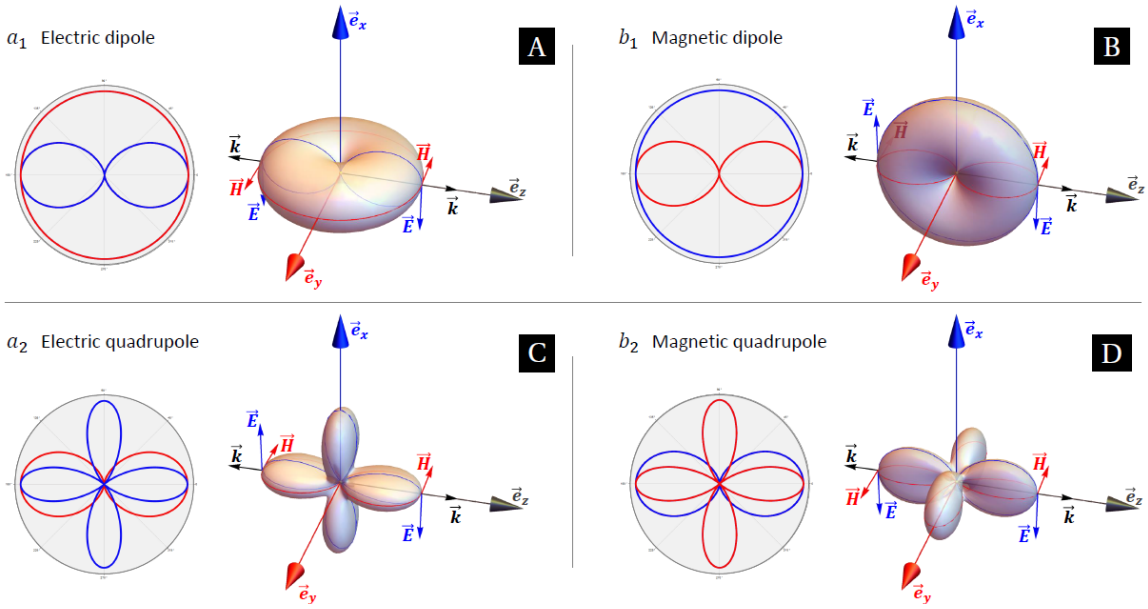

Figure 1.9: 3D representation of radiation pattern of dipoles and quadrupoles under a e_x polarized electromagnetic wave. The blue (red) 2D cuts show the radiation pattern in the electric (magnetic) plane. The electromagnetic field orientation is indicated by the blue and red arrows in both the forward ($\theta = 0°$) and backward ($\theta = 180°$) directions [25].

An important feature of electromagnetic multipoles that becomes essential for the study of multipolar interference and directional scattering, is the phase symmetry of their far-field radiation. It turns out that the radiated fields show different phases in the forward and backward directions with respect to the incident wave. It can be seen on Figure: 1.9 A and B, that the electric dipole radiation shows even parity (in electric field) while the magnetic dipole radiation shows odd parity, for which the radiated electric fields in the forward and backward directions are respectively in and out of phase. Regarding the higher order multipoles, both the electric quadrupole and magnetic octupole produce an odd-type pattern, while an even-type response is generated by the magnetic quadrupole and electric octupole terms [25].

In summary, the phase symmetries follow a simple rule: the scattering parities are

opposite for multipoles of same nature and adjacent order (for example even parity for the electric dipole and odd parity for the electric quadrupole), and for multipoles of same order but different nature (for example even for the electric octupole and odd for the magnetic octupole) [26]. We stress here that we discuss the parities in terms of electric fields, but reversed parities would be true in terms of magnetic fields, as can be seen on Figure: 1.9 , due to the electromagnetic duality.

A promising route to obtain a control over the phase of secondary wavelets is by engineering the resonators to exhibit a magnetic dipolar (MD) resonance in addition to the electric dipolar (ED) resonance. The advantage of this is that the resonators will not only interact with the electric component of light, but also with its magnetic component. As explained in Section 1.1.1 the ED mode is associated with a linear displacement current inside a resonator due to polarization, whereas, a MD mode is achieved due to a circular displacement current within the resonator. This has been experimentally realized by using high permittivity dielectric NPs such as silicon NPs, which possess Mie type magnetic and electric resonances [27, 28, 29] or a plasmonic geometry such as the split-ring resonator[30, 31], which exhibits a MD due to the induced current loop.

The presence of both the magnetic and electric dipolar resonances with equal amplitude, gives additional levers to control the scattering, and specifically its directionality. This is due to the difference in the radiation patterns of electric and magnetic field components of light of an ED and MD in opposite directions. As represented in Figure: 1.9 A and B, in case of an ED, the electric fields of light propagating in opposite directions are oriented parallel and the magnetic fields are oriented antiparallel. The situation is inverse for an MD. Therefore, by superimposing a crossed electric and magnetic dipole oscillating at the same frequency and in phase, the emitted fields interfere constructively in one direction and destructively in the opposite direction as illustrated in Figure: 1.10. Thus in order to achieve a unidirectional scattering, the two dipoles should exhibit equal scattering amplitudes and resonate at the same frequency. This condition is also known as the Kerker condition and was orginally devised by Kerker et al, for small spheres with a magnetic response at optical frequency [32].

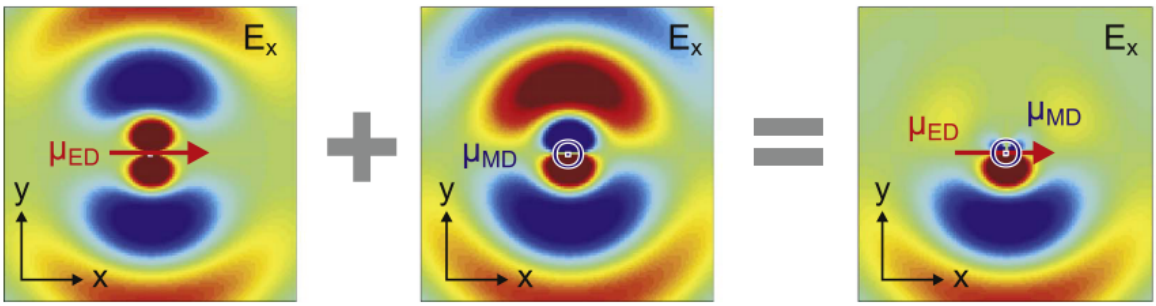

Figure 1.10: Illustration of constructive interference in one direction and destructive interference in the opposite direction due to the in-phase superposition of an electric and a magnetic dipole source with the same frequency [33].

Unidirectional scattering can also be achieved due to the response of higher order multipoles. The superimposition of electric and magnetic quadruples and hexapoles increases the directionality of scattered light as illustrated in Figure: 1.11 leading to an extreme forward or backward scattering of light. In fact, a complete forward scattering will be achieved whenever the Mie coefficients (presented in Equation 1.19) satisfy the condition $a_n = b_n$. This condition is also known as the First Kerker condition [34].

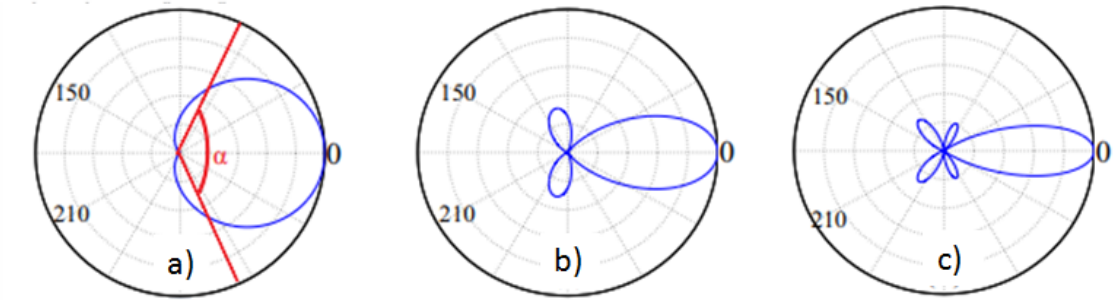

Figure 1.11: Schematic representation of the overlap of a) ED and MD, b) electric and magnetic quadruple . C) electric and magnetic hexapole.[35]. The overlap of higher order multipoles lead to the increase in the forward directionality of the scattered light.

Though the study by Kerker et al [32] established the conditions to obtain zero back scattering, this condition accounts only for unidirectional scattering occurring due to the overlap of in-phase magnetic and electric multipoles having the same order and magnitude. To account for the interference of EM multipoles of different order, Wei Liu et al [26] established the generalised kerker condition. This accounts for the overlap of even (ex; a_1, b_2 etc) and odd (ex; a_2, b_1 etc) parities of Mie coefficeints. Meaning, interference between pure electric response could also lead to directional scattering [26]. The generalized kerker condition can be expressed as shown below:

$$\sum_{n=}^{\infty} \mathscr{O}_n = \sum_{n=}^{\infty} \mathscr{E}_n \tag{1.20}$$

where, $\mathscr{O}_n$ and $\mathscr{E}_n$ represents odd and even multipoles respectively. It is clear that suppression of backward scattering can be obtained not only for perfectly matched pairs of multipoles of same order, but also for pairs of multipoles of same nature but with different orders. The combination of different multipoles to obtain directional scattering is shown in Fig: 1.12. The presence of higher order multipoles increases the directionality of the radiated field.

Resonators with such functionalities can be used to control scattering not only in the forward or backward directions, but also along all other possible scattering angles. These resonators, when deposited (or arranged) over a surface in a controlled manner to build a MS, can be used to manipulate the optical wavefront based on the interference of resonant multipolar excitations. Although this section focuses mainly on directional scat-

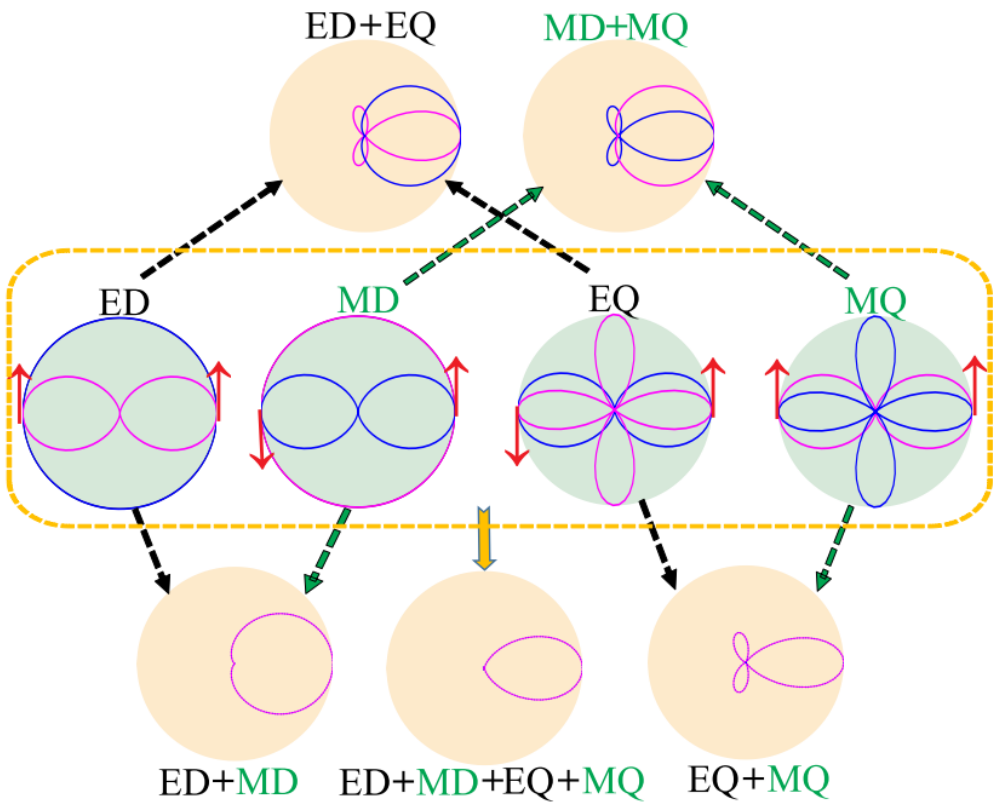

Figure 1.12: Illustration of combination of different multipoles leading to directional scattering. Red arrows indicate the radiated electric fields in the forward and backward directions, with upward and downward arrows corresponding to out-of-phase and in-phase fields with respect to the incident electric field, respectively. All the multipoles shown are resonantly excited and of the same magnitude in terms of backward scattering. For both individual and overlapped multipoles, only the in-plane (purple curves) and out-of-plane (blue curves) scattering patterns are shown for clarity [26].

tering, HMSs have been studied to obtain other properties such as perfect absorption [36, 37, 38], perfect transmission [39, 40], perfect reflection [41, 42]etc. The fabrication of MS face two main challenges, the first is the fabrication of resonators having the specific functionalities (such as presence of MD etc). Secondly, the deposition of the resonators to build a surface. In order to realize the required properties of a MS, the resonators have to be arranged in a very controlled manner. This study will focus only on the fabrication of resonators exhibiting forward scattering properties.

1.3 Resonators and their fabrication

Resonators of varies composition and structures have been synthesized using both top-down methods such as lithography and bottom-up approaches such as wet chemistry method. This section will shed light on some of their structures and fabrication techniques.

1.3.1 Dielectric nano resonantors

An "all dielectric" system, such as silicon (Si) NPs exhibits Mie resonances with electric and magnetic multipole. To achieve Mie resonances, the refractive index of the particle should be high compared to the index of the medium. A sphere with high refractive index traps the light within it, and enhances the electromagnetic field, exhibiting resonances for specific values of the wavelength (Figure 1.13). These resonances are the modes supported by the particle. The fundamental mode, corresponding to the scattering from a magnetic dipole, occurs when the wavelength inside the particle has approximately the same size as the particle. The second mode, corresponding to electric dipole scattering, is when the wavelength is half the size of the cavity, and so on.

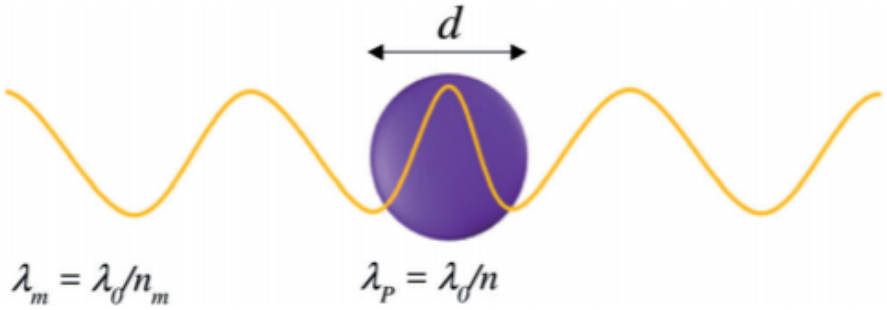

Figure 1.13: Magnetic dipole scattering is excited when the wavelength within the particles is of the same size, d, as the particle [43].

$$\lambda_{b_1} = \frac{\lambda_o}{n} \approx d \tag{1.21a}$$

$$\lambda_{a_1} = \frac{\lambda_o}{n} \approx \frac{d}{2} \tag{1.21b}$$

Si NPs are an attractive choice due to its availability and mature nano fabrication techniques. It has a high refractive index and negligible losses due to absorption. Si nanostructures of varies size and structures have been synthesized using top-down techniques such as electron beam lithography [44], focused ion beam milling [45], laser ablation [46], focused beam laser printing [47], etc. Figure 1.14 shows Si NPs of various sizes produced using laser ablation and their dark-field images. These techniques are however very expensive and time consuming. Instead the bottom-up approach are being developed to produce Si NPs in large quantity and cost efficiently. The different wet-chemistry techniques and their challenges are explained in reference [43].

Apart from Si NPs, other high refractive index materials such as germanium [48], gallium arsenide [49], titanium oxide [50] etc, have also been demonstrated to exhibit electric and magnetic Mie type resonances.

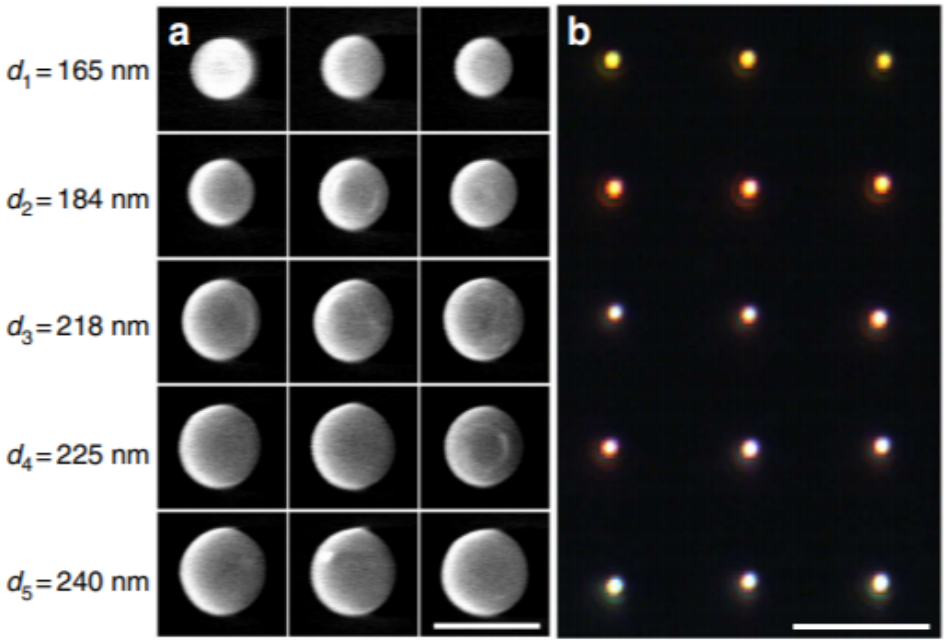

Figure 1.14: a) SEM images of Si NPs produced using laser ablation. Various sizes can be obtained by changing the pulse energy. b) Dark field microscopic images of Si NPs of various sizes witnessed by the change in color [47].

1.3.2 Corona structured nano resonantors

The design theoretically proposed by Simovski and Tretyakov [51], consists of a dielectric core surrounded by non-touching plasmonic NPs (1.15 a). Such system indeed presents isotropic magnetic and electric dipolar resonances at optical frequencies. The geometry of the core-corona structure is show in Fig 1.15. The magnetic response of such a structure is due to the Faraday effect of electromagnetic induction. Indeed, when illuminated by light, the plasmonic particles on the surface produce rings of plasmonic circular currents leading to a magnetic polarization (Figure: 1.15).

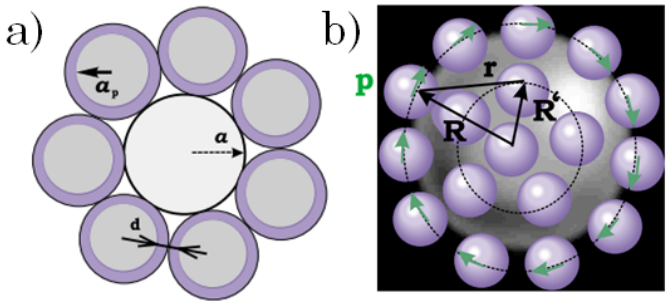

Figure 1.15: a) Schematic representation of a cluster of plasmonic nanocolloids at the surface of a dielectric core, b) Rings of plasmonic currents produced by nanocolloids along the z axis and the induced dipole moments are shown by bold green arrows, and the rings are equidistant (applied magnetic field is along the z-axis) [51].

As shown in section: 1.1.2, the resonance frequency (ω_p) of the plasmonic NPs is red

shifted due to the electromagnetic coupling of the plasmonic particles leading to two collective plasmonic resonances [6]. The first resonance is due to the coupling of the individual NP plasmon resonance which leads to an electric mode when all plasmon-induced electric dipoles are in the same direction. The second resonance is due to the magnetic mode which occurs due to the rotating geometry of the plasmon resonance. The artificial magnetism obtained largely depends upon the geometrical parameters such as, the radius of the dielectric core (a), the radius of the plasmonic particle (a_p) and the distance between the plasmonic particles (d).

The total number of plasmonic particles (N_{tot}) present on the dielectric core can be expressed as shown below:

$$N_{tot} = \left[\frac{4(a + a_p + \frac{d}{2})^2}{(a_p + \frac{d}{2})^2} \right] \tag{1.22}$$

These structures have also been experimentally produced using bottom-up fabrication technique. Raspberry like structures were fabricated using the electrostatic interaction between positively charged silica cores and negatively charged gold NPs [52, 53]. The same system has also been fabricated using thiol chemistry [53]. Similar structures with different dielectric cores, such as polystyrene [54], and plasmonic particles, such as silver NPs [55], have also been fabricated using bottom up approaches. Recently Many *et al.* [56], succeeded in increasing the magnetic response by controlling the number of NPs as well selectively placing the plasmonic nanoparticles on the silica core.

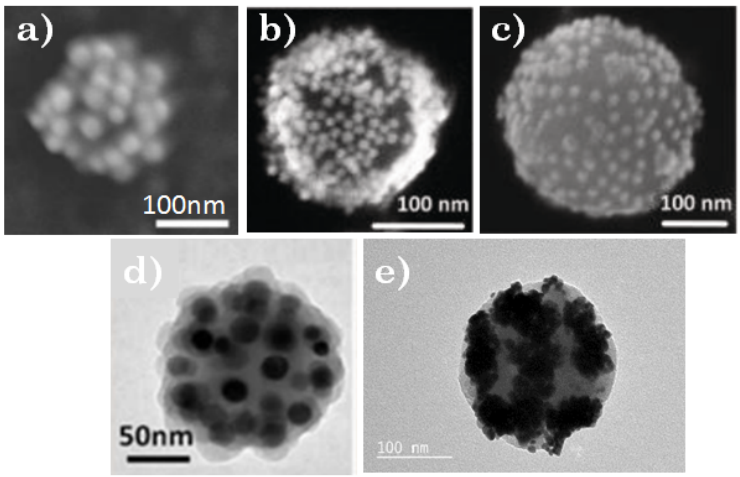

Figure 1.16: Electron microscopic images of a) Polystyrene core and silver NPs corona [54] , b) and c) Silica core and gold NPs as corona by two different fabrication method [53], d) Silica core and silver NPs as corona [55] and e) Dodecapods structure [56].

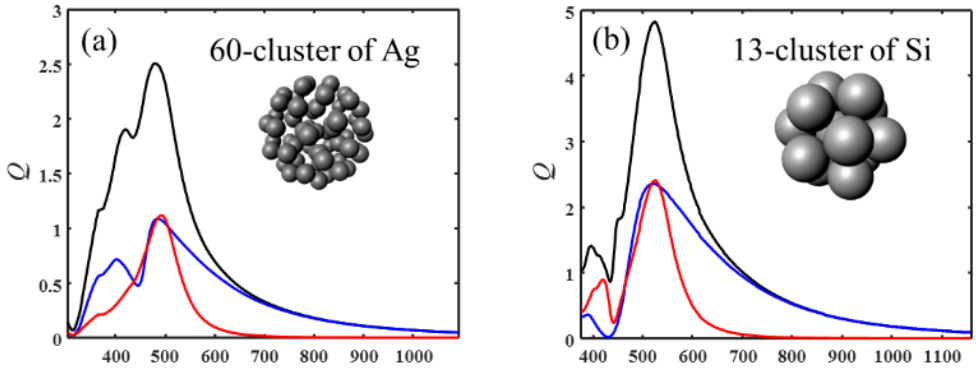

Figure 1.17: Scattering efficiency of a cluster of a) 60-Silver NPs b) 13-Silicon NPs. The black, red and blue curve represents total, electric and magnetic scattering efficiency respectively [59].

1.3.3 Nanoparticle clusters

The design proposed by Rockstuhl *et al.* [57] for meta-atoms involves an assembly of N NPs of radius r distributed homogeneously within a spherical volume of radius R of a so-called NP-cluster. The NP-clusters can then be described as effective medium spheres. The study shows that interesting properties are obtained if the constituting NPs are either plasmonic (metallic NPs) or of high refractive index (silicon or titanium oxide). In such case indeed, the optical index of the effective medium constituting the spheres can be tailored by varying the cluster filling fraction $f = \mathrm{N}(r/\mathrm{R})^3$. This optical index can then reach values not attainable with a natural material, and these clusters thus constitute a new class of adjustable Mie resonators. Indeed, if the values of r , R and the effective optical index can be tailored at the fabrication step, then a true capacity of engineering of the optical response of colloidal resonators can be attained. It can, in particular, allow tuning the index so that the magnetic and electric dipoles resonate at the same frequency, with no need to resort to non-spherical shapes [58]. The study was performed for two spherical clusters namely, clusters made of 60 silver NPs with $r = 15nm$ and $f = 20\%$ and clusters made of 13 silicon NPs with $r = 41nm$ and $f = 47\%$. Figure 1.17 shows the scattering efficiency of both clusters. Although the efficiency of silicon NPs is about 2 times the efficiency of silver NPs, attaining a volume fraction of 47% experimentally is very difficult.

The fabrication of these clusters has been achieved using bottom-up self assembly approach. According to simulations, such clusters of gold NPs synthesized using a solution based synthesis method in [60, 61] are expected to exhibit a magnetic response. Similarly, clusters of silver NPs were fabricated using a emulsion based method [6]. A two dimensional array of gold NP cluster was fabricated using a template directed colloidal self assembly [62]. To our knowledge, these works only mention simulation results but no direct measurements of the magnetic contribution. This will be discussed further in the next section.

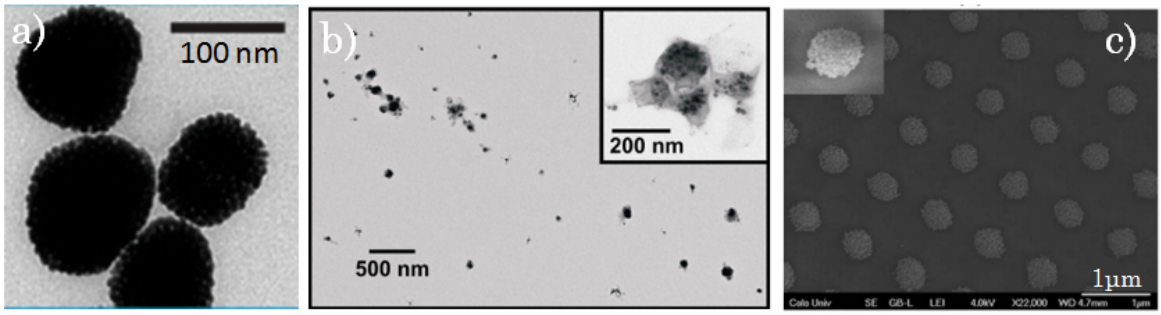

Figure 1.18: Transmission electron microscopy images of a) clusters of gold NPs [60] b) clusters of silver NPs [6] c) 2-D array of gold NP clusters [62].

1.4 Study of resonators

Experimental study of colloidal suspension as well as 2-D arrays of meta-atoms (resonators) have been performed using different light scattering techniques and compared with computational studies to indicate the presence of artificial magnetism. This section will provide a brief summary on these techniques and their results.

1.4.1 Extinction coefficient

Extinction spectra of colloidal dispersions of resonators have been widely used to indicate the presence of magnetic dipolar resonances in resonators. Dintinger *et al.* [6], investigated the extinction spectra of silver NP clusters and the influence of their size on the extinction spectra. These curves were are also compared to simulations performed using extended Mie theory [63]. The experimental and simulated extinctions are shown in Figure: 1.19. It is shown that the extinction peak of silver NP clusters is red shifted compared to the individual NPs. The simulation, where the size of the NP and the interparticle distance is fixed, shows a similar trend and it is evident that the red shift in wavelength is a function of the NP cluster size. The absence of the fine structure, seen in the simulation spectra (Figure: 1.19 b), in the experimental spectra can be attributed to discrepancy in the size or shape of clusters in the colloidal solution. The experimental spectra is dominated by the global shape of the cluster, whereas the fine structures in the simulation arises from the NP arrangement inside the cluster.

Similar studies were also performed on gold NP clusters [61], core-shell structures [52] and also on colloidal solutions of non-metallic materials such as selenium [64]. Although extinction spectra can be used to study the optical response of the meta molecules, the contribution of different multipoles cannot be directly extracted from the extinction spectra as this information is encoded in the spatial distribution of the scattered field [60, 65]. In the next section, we present an experimental way to extract this information using static light scattering technique.

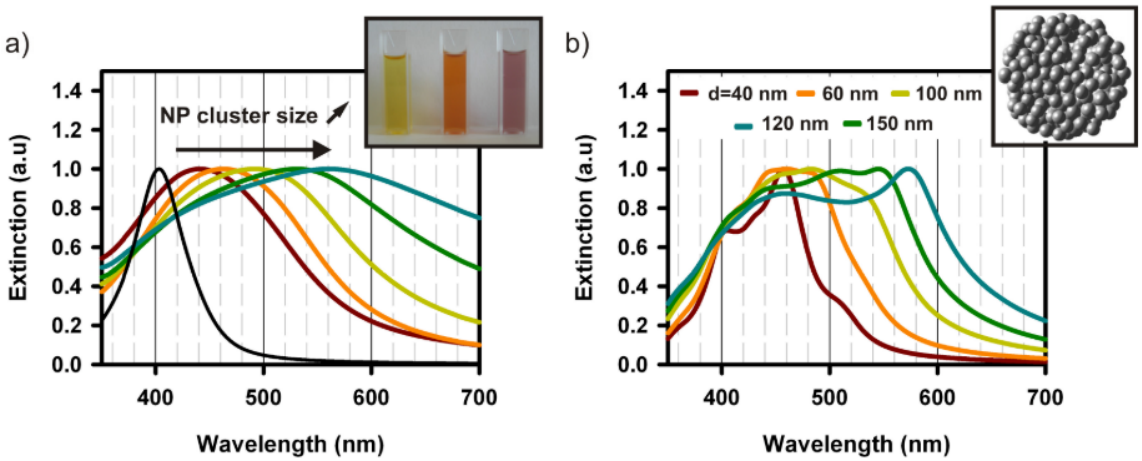

Figure 1.19: a) Experimental Uv-Vis extinction spectra (Insert: colloidal dispersion of silver NP clusters), b) Simulated extinction spectra [6].

1.4.2 Static light scattering

The use of light scattering experiments to observe the presence of magnetic dipole and/or electric quadrapole for an isotropic scatterer was first shown by Sharma [66]. This was achieved by observing the polarization and angular distribution of the scattered light in the plane perpendicular to the incident polarized laser beam. The spectra of scattered power for an aqueous suspension of polystyrene is shown in Figure: 1.20, the spectra was obtained at an angle $\theta = \pi/2$. At that angle the light scattered by the ED has a sine-squared angular dependence with respect to the transversely polarized incident beam, whereas the MD has a cosine-squared angular dependence to the axially polarized incident beam. The axial scattered electric field corresponds to a combined contribution of both MD and EQ. If both are present, it is not possible to separate the two contributions at $\theta = \pi/2$.

Static light scattering (SLS) measurements were performed to study core-corona particles made of a polystyrene core and covered with silver NPs by Sheikholeslami *et al.* [54]. The measurements were performed using a HeNe laser at $\lambda = 633$ nm. From simulations, the expected contribution from ED at this wavelength was assumed to be minimized. The ratio of MD to ED contribution to scattering was calculated to be 12%. However, this value may not correspond to the maximum one as the measurements were only performed at one wavelength.

In similar SLS measurements, Ponsinet *et al.* [52] established a method to study the optical response of isotropic scatterers across the whole visible spectrum. Figure 1.22 shows the schematic representation of the setup used to study the scattering properties of suspensions of scatterers. A supercontinuum white source was used to provide a monochromatic light beam at wavelength ranging from 400 nm to 800 nm. The light scattered in the transverse and axial plane is measured at a scattering angle of 90°. This setup was used to study various core-corona materials such as gold raspberries [52], silver

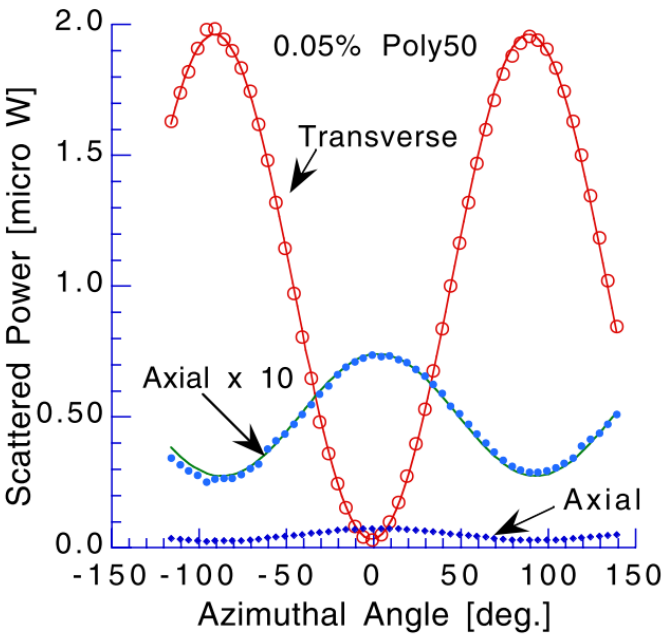

Figure 1.20: Angular distribution of light scattered by polystyrene spheres of radius $r \approx 50$ nm [66].

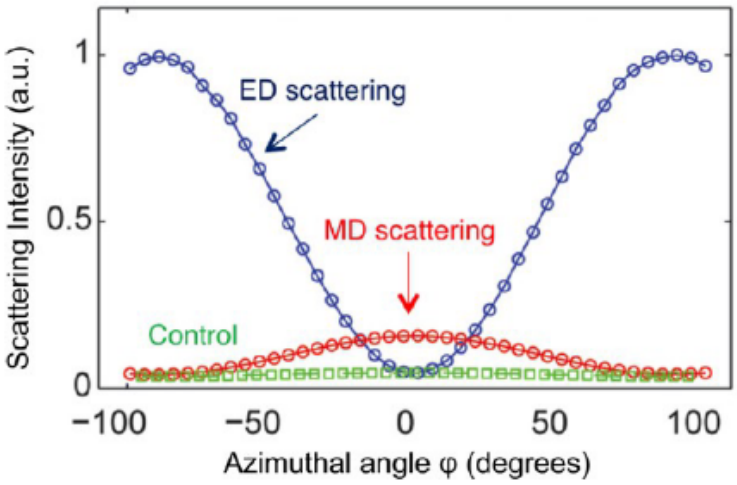

Figure 1.21: Experimental data of Angular distribution of light scattered by polystyrene spheres surrounded by silver NPs. [54].

raspberries [55], and dodecapods [56]. The magnetic to electric response obtained were 7, 28 and 14 % respectively. These results seem to be in good agreement with simulations. Although this new setup provides information across the whole visible spectrum, it is still not possible to separate the individual contributions from different multipoles. The axial data indeed contains the contribution from both MD and EQ. However the separation of each contribution can be achieved by varying the scattering angle θ. This is what we did in the present work and is further explained in Chapter 4.

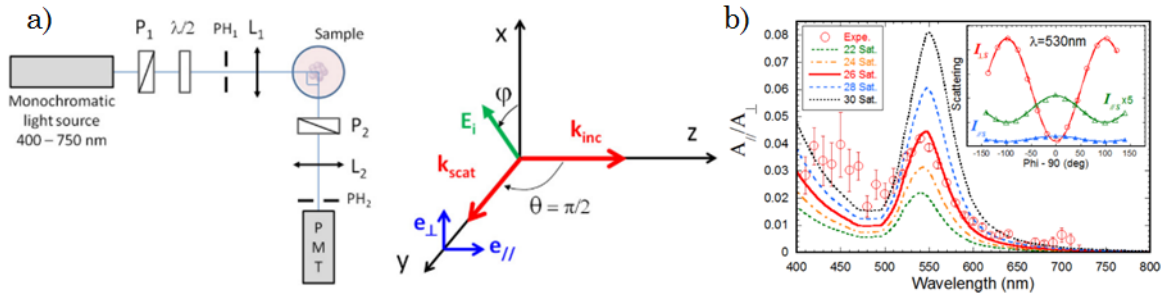

Figure 1.22: a) Schematic representation of the SLS setup (left) and scattering geometry (right) b) Experimental ratio of magnetic response to electric response for silica particles covered with Au NPs for various numbers of Au NPs (left insert). The right insert shows the angular dependency of transverse and axial scattering at λ = 530 nm. [52].

1.4.3 Dark field scattering

Dark field spectroscopy can be used to study the scattering properties of a single particle. This is achieved by selectively discarding the reflected or the transmitted light. The dark field spectrum, in addition to simulations, can be used to identify different multipolar contributions as shown in Fig 1.23.

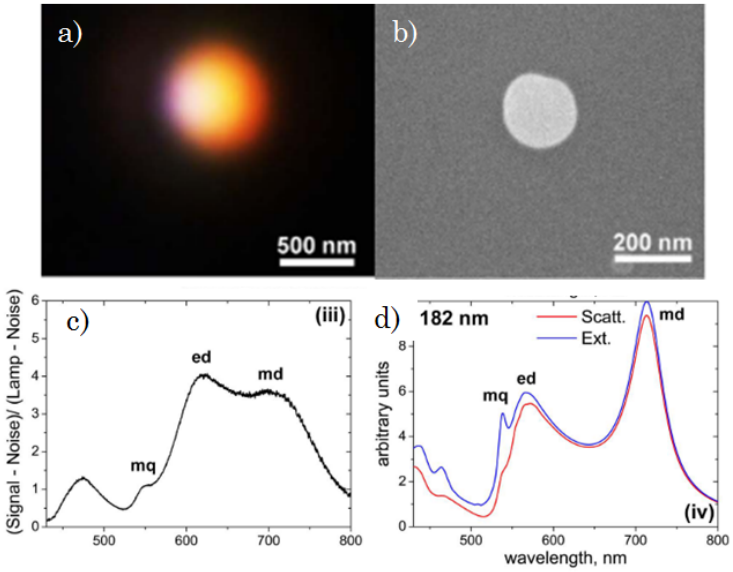

Figure 1.23: a) Image obtained from dark field microscopy of a single Si NP with r = 182 nm [46], b) Scanning electron microscopy of Si NP c) Dark field spectrum of the single Si NP shown above d) Mie scattering calculation of Si NP with r = 182 nm [46].

Dark field microscopy has also been used to study directional scattering of a single particle. Y.H.Fu *et al.* [27] measured the light scattered by a Si NP in the forward and backward direction, Fig: 1.24 shows the setup used for the measurements and the spectrum obtained for a Si NP. Si NPs were first deposited on a glass substrate which was then placed face down on the sample holder, to measure the forward scattering, the light from the upper dark-field condenser is sent onto the sample surface (orange lines), and the

light scattered in the forward direction (green arrows) is collected by the lower dark-field objective lens. In order to obtain backward scattering spectra, the light coming from the lower dark- field objective lens (orange lines), and the light scattered in the backward direction (blue arrows) were collected by the same lens.

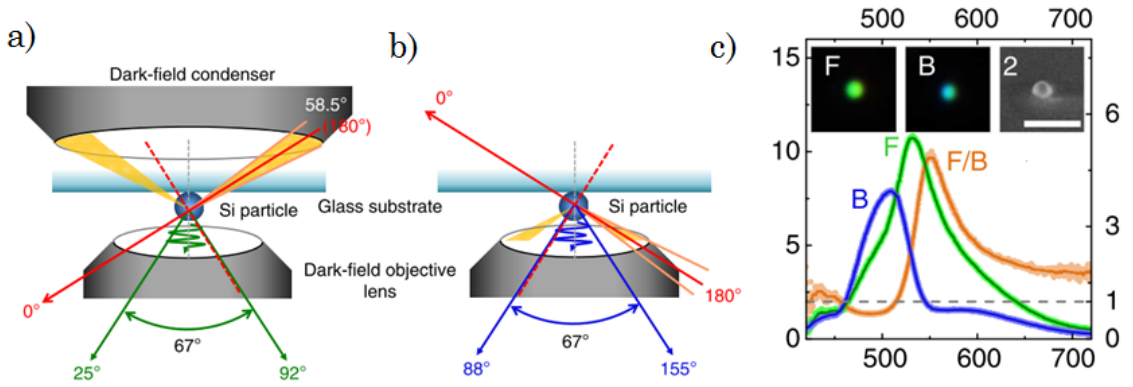

Figure 1.24: Schematic representation of the dark field setup used to measure the light scattered in the a) forward and, b) backward direction c) forward (green) and backward (blue) scattering intensities and the ratio of forward to backward scattering (f/b). Inserts: dark-field images of transmitted (f) and reflected (light) and SEM image of Si NP.[27].

1.4.4 Bulk 3D and 2D scattering analysis

1.4.4.1 Ellipsometry

Spectroscopic ellipsometry (SE) is an optical tool used to characterize the optical properties of thin films. SE measure the change of polarization of the reflected (or transmitted) light as a function of wavelength [67]. The reflection (or transmission) coefficients for the light polarized parallel (p-polarized) and perpendicular (s-polarized) to the incident plane are measured.

The optical constant, namely the electric permittivity ($\epsilon(\lambda)$), of a metasurface can be estimated using spectroscopic ellipsometry measurements. SE has been used in the literature to study the optical properties of hyperbolic metasurfaces [68], plasmonic metasurface [69], split-ring resonators [70], etc.

1.4.4.2 Spectrophotometry

A microspectrophotometer can be used to measure the optical response such as transmittance, reflectance, polarization etc of a metasurface. This tool can thus be used to characterize metasurfaces with novel optical properties such as 100% absorbance or unidirectional scattering.

The extinction spectra of a 2-D array of gold NP clusters was studied by Lee *et al.*, [62], the experimental spectra was obtained using a microscope coupled with a fiber spec-

trometer. These spectra were then compared to simulations which showed an excellent agreement with the experimental data.

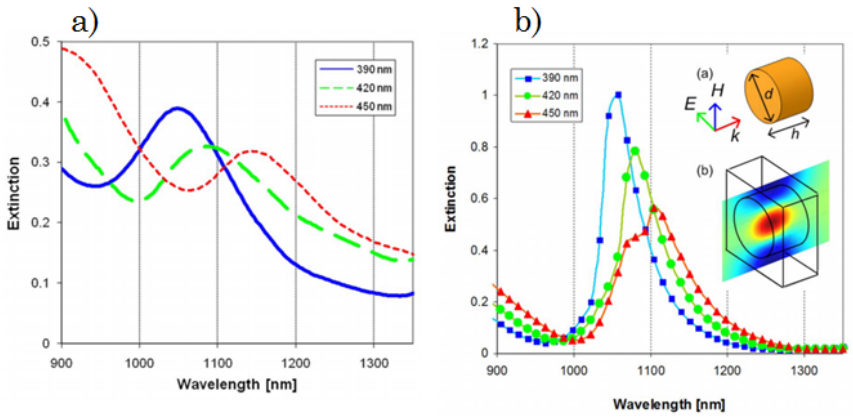

Figure 1.25: a) Experimental extinction spectra of a 2-D array of NP clusters as a function of cluster size, b) Simulated extinction spectra. The geometry is shown in the inserts a) electric field pattern at 1.08 μm and b) when d = 420 nm and h = 300nm [62].

1.5 Fabrication route

In this thesis work, we concentrated on synthesizing cluster nanoresonators using colloidal assembly of NPs with well controlled size, shape and internal volume fraction. As discussed previously, such an assembly can be used as building-blocks to create a metasurface. This section will provide a brief summary of different bottom up approaches that were used to synthesize clusters of NPs.

1.5.1 Introduction to cluster fabrication

Colloidal assembly of nanoparticles have been studied for various applications in a wide range of fields due to their unique properties compared to their bulk counterparts. Clustering them together not only allows the combination of their individual properties but also takes advantage of the interaction between neighboring NPs, which might results in new properties.

The temperature induced aggregation of gold NPs was achieved by coating the NPs with a thermo-sensitive polymer. When the temperature is higher than the polymer's phase transition temperature, the polymer precipitates leading to the aggregation of NPs [71]. The aggregation of NPs is reversed when the temperature is decreased, thus creating a reversible and controlled route to synthesize Au NP clusters. Similarly, solvent induced aggregation of NPs can be achieved by selectively capping the surface of the NPs with different amphiphilic block copolymers, which will begin to precipitate in the presence of selective solvents [72, 73]. Dense clusters of nanoparticles have been produced by other

chemical and physico-chemical routes, using smart polymer brush coverage [74], specific ligand association [6, 75], or electrostatic assembly [76, 77], for example. Figure 1.26 shows the TEM images of the clusters obtained from different synthesis approaches, it is evident from these images that these methods do not always produce dense clusters. More importantly there is no control over the shape or size of the final clusters.

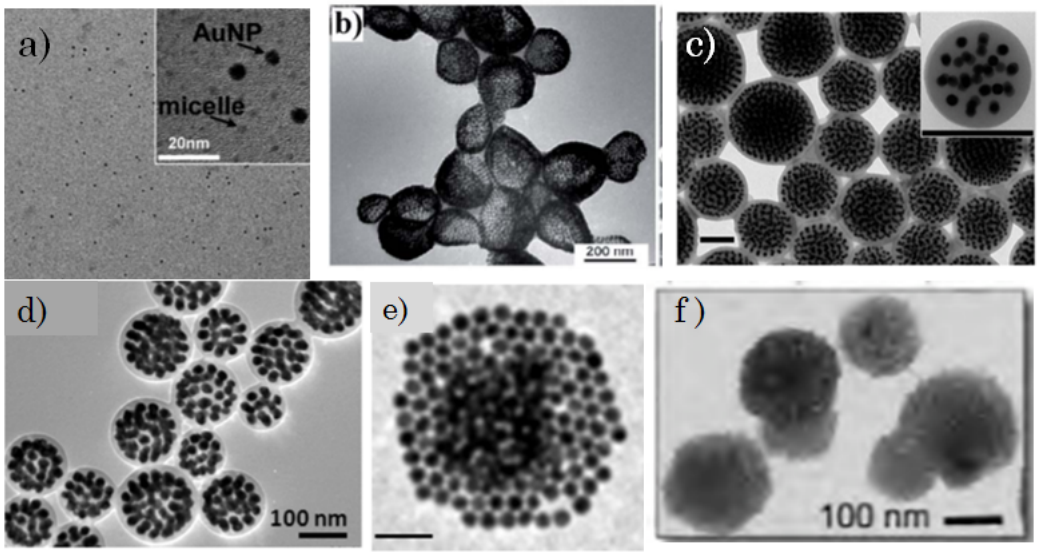

Figure 1.26: Transmission electron microscopy of clusterS of NPs taken from a) [71] b) [74] c) [73] scale bar is set to 200 nm d) [72] e) [77] scale bar is set to 50 nm f) [76].

1.5.2 Fabrication of resonators using the emulsion route

Confinement of nanoparticles in emulsion droplets has been considered as a powerful way to control their assembly both for a small [78, 79] or for a large numberN [80, 81, 82] of NPs in the cluster. This method involves the dispersion of NPs in phase 1 (water or oil), which is then dispersed in phase 2 (oil or water), this system is known as a water-in-oil (or oil-in-water) emulsion. Schematic illustration of clusters obtained from an oil-in-water emulsion is depicted in Figure 1.27. In the first step, an emulsion containing droplets of NPs suspension is created using surfactants (to reduce the surface tension of droplets). In the second step, the droplets are ripened to form the final clusters. The second step determines the shape and internal structure of the final clusters and this is explained in detail in the later part of this section.

Clusters of polystyrene NPs from water-in-oil emulsion were thus obtained by evaporating the water at 100° Celsius [78]. As the droplet size is reduced, the nanoparticles rearrange themselves within the droplets. The final structure of the as synthesized clusters were studied. A pictorial representation of the structural configuration of clusters for different number of particles is shown in Figure 1.28. The number of particles inside each droplet also plays a major role in determining the structural configuration of

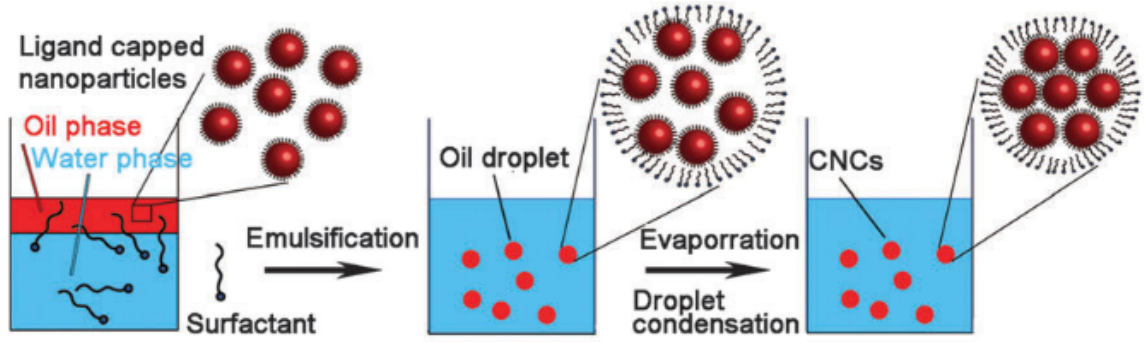

Figure 1.27: Schematic representation of clusters obtained by the ripening of an oil-in-water emulsion [83].

the final cluster. For low particles numbers, e.g. 3 or 4, triangular and tetrahedra configurations are respectively obtained, this coincides with the expected structure using a Lennard Jones potential [84]. For higher numbers, for instance at 8, a unique structure of two regular tetramers parallel to each other twisted by an angle of 45° is observed.

At much higher inner particles number,(i.e. $n \geq 40$, obtained with gold nanoparticles of size 6 nm), icosahedral (IC) and decahedral structures are obtained [80] as shown in Figure 1.29, the theoretical prediction was performed using Lennard-Jones potential [84].

Another important factor which affects the structure of the final cluster is the speed at which the droplet size of phase one is reduced. For example, in an article describing the water-in-oil emulsion synthesis of silica NP clusters, it was observed that, as the evaporation rate was increased (through the use of microwave radiation of increasing intensities to selectively evaporate the water molecules), amorphous clusters were obtained [85]. The low packing quality can be seen directly from the reflectance spectra of the colloidal crystals as a function of microwave intensity. It is obvious from the reflectance spectra in Figure 1.30 b, that the reflectance peak width increases (as their intensity decreases) with evaporation speeds, which indicates that the long range ordering of nanoparticles inside the cluster decreases. The maximum reflectance peak intensity is obtained for the slowest evaporation rate (0 W) and when a weak irradiation (170 W) is used. With a low evaporation rate, the particles have enough time to find the energetically optimal position thus forming a uniformly organized clusters.

The solubility of NPs in different liquid phases depends upon the composition and density of the ligand used to cover the surface of NPs. For instance, if hydrophobic nanoparticles are originally dispersed in water using adapted ligand while still conserving a partial hydrophobic nature, they tend to form a colloidal cluster in which the particles stick to the interface. As the droplet size is reduced, they come closer together and form a capsule (Figure 1.31 a)[86]. If the droplet size is further reduced, it may even form a non spherical structure. However, if the colloidal particles are confined to the interior of the droplet rather than at the interface, the interaction between nanoparticles leads to the formation

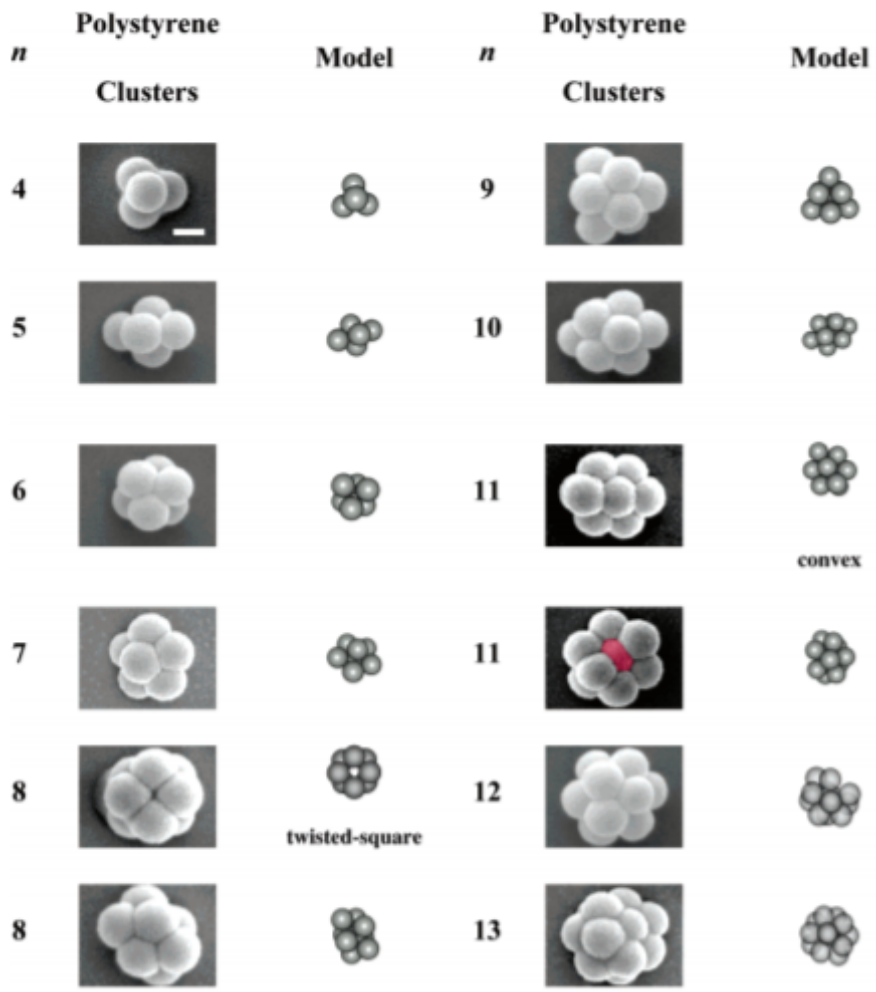

Figure 1.28: Structural configuration according to the number of inner particles [5]. Each particle is a PS latex bead of size 230 nm, the scale bar in the image above is 200 nm [78].

of a homogeneous cluster [86]. This can be achieved by tuning the wettability of the surface of nanoparticles with ligands (that may be polymers in certain cases). The ligands also prevent the nanoparticles from aggregating with each other, as the size of the droplet is reduced, nanoparticles come closer to each other but are still separated by the polymer corona.

Thus it can be concluded that the final structural arrangement of nanoparticles inside the clusters strongly relies upon the initial number of nanoparticles inside the initial droplets, the speed of droplet ripening and the ligand used to stabilize the NP's surface.

1.5.2.1 Ostwald ripening

The reduction in droplet size can also be achieved by a process called Ostwald ripening in which the smaller droplets shrink to the benefit of the larger droplets by the molecular diffusion of the dispersed phase molecules in the continuous phase [81]. As the size of the droplet decreases, the volume fraction of the NPs inside the droplet increases and this can lead to different structural organizations of the NPs. The formation of the nanocluster

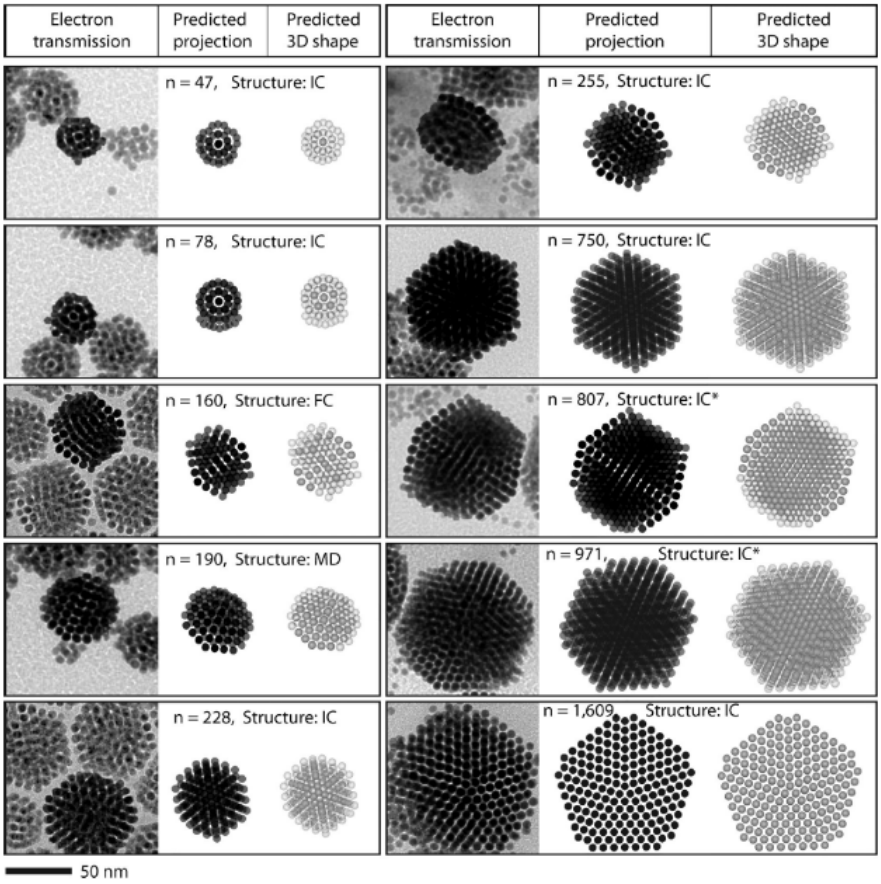

Figure 1.29: TEM images illustrating the structure of the cluster as the number of particles is varied [80].

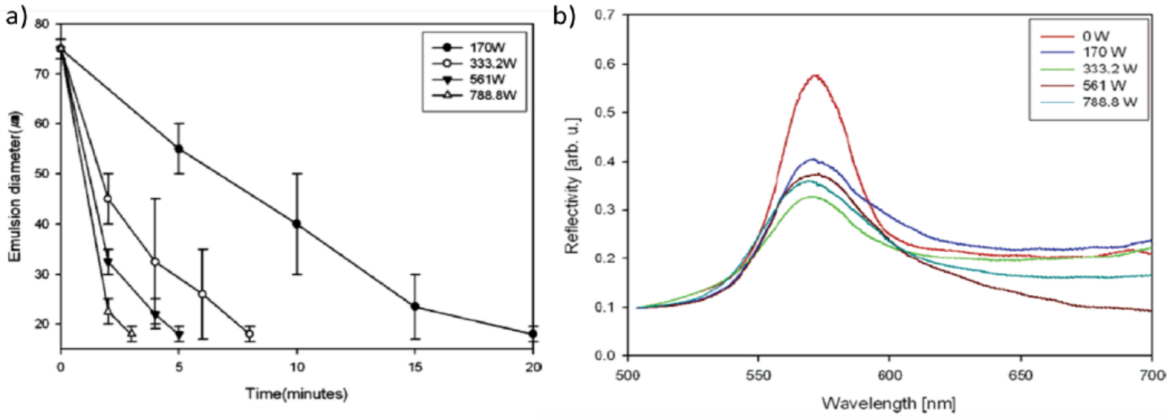

Figure 1.30: a) Evolution of the emulsion droplet diameter as a function of time for various microwave intensities; b) Reflectance spectra of the final silica cluster for various evaporation rates [85].

both depends on the NPs volume fraction (ϕ) and size. The NPs start to feel each other and interact in the droplet when the volume fraction inside the droplet reaches a critical value (ϕ^*). At the critical volume fraction, a coexistence between "free" and aggregated NPs is expected inside the droplet. When the volume fraction is further increased a complete crystallization of the NPs inside aggregates is obtained. The final cluster is obtained and a further increase in the volume fraction leads to a decrease in the lattice parameter

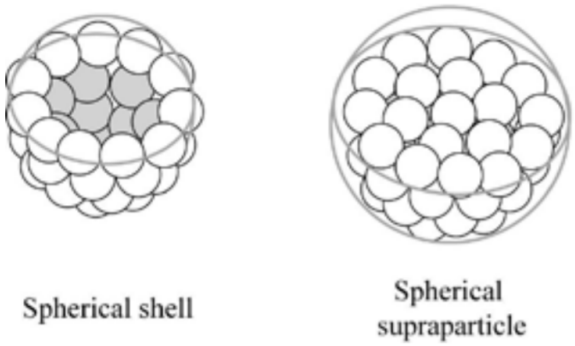

Figure 1.31: a) A shell like structure when nanoparticles stick to the interface, b) cluster formation when nanoparticles are confined to the interior of the droplet [86].

and to structural changes of the NPs organization in the cluster [81]. The NPs critical volume fraction is estimated by adding the diameter of the core NP and the twice the length of the ligand (polymer) to deduce the effective NPs/ligands diameter.

The apparent diameter of the nanoparticle is defined as:

$$D_{app} = D_c + 2e \tag{1.23}$$

Where D_c is the diameter of the nanoparticle and e is the thickness of the ligand adsorbed layer.

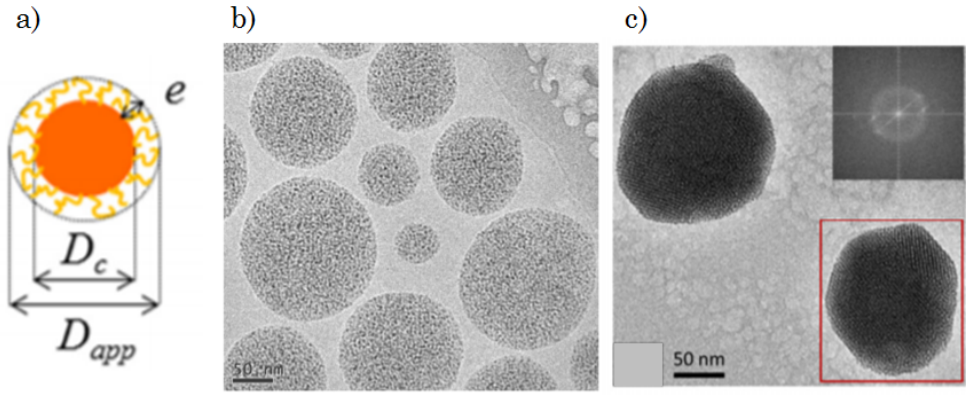

Figure 1.32: a) Apparent diameter of the nanoparticle surrounded by a polymer corona, Cryo-TEM images of b) water-in-oil emulsion c) clusters of gold NPs. Inset: Fourier transform of the TEM image (calculated for the region inside the red rectangle) [81].

1.6 Conclusion

This chapter summarized the basic optical characteristics of different materials and the constraints on final attainable optical properties of naturally occurring materials. It points out the need of artificial materials to attain the novel optical properties. The concept of 'meta atoms', 'metamaterials', and 'metasurfaces' were introduced. And a brief summary

on the synthesis of different resonators focusing on the use of emulsion templating and methods that can be employed to study their optical properties was given.

This thesis will focus on the synthesis of colloidal assemblies of Gold NPs with a control over their size, shape and volume fraction illustrated using different characterization techniques. The optical properties of these clusters were studied using light scattering technique and the influence of different experimental parameter on the final properties will be illustrated.

1.7 Reference

[1] M. Quinten, *Optical properties of nanoparticle systems: Mie and beyond*. John Wiley & Sons, 2010. 8

[2] L. D. Landau, J. Bell, M. Kearsley, L. Pitaevskii, E. Lifshitz, and J. Sykes, *Electrodynamics of continuous media*, vol. 8. elsevier, 2013. 9

[3] W. Cai and V. M. Shalaev, *Optical metamaterials*, vol. 10. Springer, 2010. xiii, 10, 12

[4] S. Eustis and M. A. El-Sayed, "Why gold nanoparticles are more precious than pretty gold: noble metal surface plasmon resonance and its enhancement of the radiative and nonradiative properties of nanocrystals of different shapes," *Chemical society reviews*, vol. 35, no. 3, pp. 209–217, 2006. xiii, 16

[5] M. Behera and S. Ram, "Spectroscopy-based study on the interaction between gold nanoparticle and poly (vinylpyrrolidone) molecules in a non-hydrocolloid," *International Nano Letters*, vol. 3, no. 1, p. 17, 2013. xiii, 16

[6] J. Dintinger, S. Mühlig, C. Rockstuhl, and T. Scharf, "A bottom-up approach to fabricate optical metamaterials by self-assembled metallic nanoparticles," *Optical Materials Express*, vol. 2, no. 3, pp. 269–278, 2012. xiv, 17, 27, 28, 29, 30, 35

[7] S. B. Glybovski, S. A. Tretyakov, P. A. Belov, Y. S. Kivshar, and C. R. Simovski, "Metasurfaces: From microwaves to visible," *Physics reports*, vol. 634, pp. 1–72, 2016. xiii, 19

[8] D. R. Smith, J. B. Pendry, and M. C. Wiltshire, "Metamaterials and negative refractive index," *Science*, vol. 305, no. 5685, pp. 788–792, 2004. 19

[9] S. S. Oh and O. Hess, "Chiral metamaterials: enhancement and control of optical activity and circular dichroism," *Nano Convergence*, vol. 2, no. 1, p. 24, 2015. 19

[10] Z. Wang, F. Cheng, T. Winsor, and Y. Liu, "Optical chiral metamaterials: a review of the fundamentals, fabrication methods and applications," *Nanotechnology*, vol. 27, no. 41, p. 412001, 2016. 19

[11] P. Alitalo and S. Tretyakov, "Electromagnetic cloaking with metamaterials," *Materials today*, vol. 12, no. 3, pp. 22–29, 2009. 19

[12] N. Fang, H. Lee, C. Sun, and X. Zhang, "Sub–diffraction-limited optical imaging with a silver superlens," *Science*, vol. 308, no. 5721, pp. 534–537, 2005. 19

[13] C. R. Williams, S. R. Andrews, S. Maier, A. Fernández-Domínguez, L. Martín-Moreno, and F. García-Vidal, "Highly confined guiding of terahertz surface plasmon polaritons on structured metal surfaces," *Nature Photonics*, vol. 2, no. 3, pp. 175–179, 2008. 19

[14] V. Logeeswaran, A. Stameroff, M. S. Islam, W. Wu, A. Bratkovsky, P. Kuekes, S. Wang, and R. Williams, "Switching between positive and negative permeability by photoconductive coupling for modulation of electromagnetic radiation," *Applied Physics A*, vol. 87, no. 2, pp. 209–216, 2007. 19

[15] A. V. Kildishev, A. Boltasseva, and V. M. Shalaev, "Planar photonics with metasurfaces," *Science*, vol. 339, no. 6125, p. 1232009, 2013. 20

[16] D. Lin, P. Fan, E. Hasman, and M. L. Brongersma, "Dielectric gradient metasurface optical elements," *science*, vol. 345, no. 6194, pp. 298–302, 2014. 20

[17] A. Arbabi, Y. Horie, A. J. Ball, M. Bagheri, and A. Faraon, "Subwavelength-thick lenses with high numerical apertures and large efficiency based on high-contrast transmitarrays," *Nature communications*, vol. 6, no. 1, pp. 1–6, 2015. 20

[18] Y. Zhao and A. Alù, "Tailoring the dispersion of plasmonic nanorods to realize broadband optical meta-waveplates," *Nano letters*, vol. 13, no. 3, pp. 1086–1091, 2013. 20

[19] N. Yu, F. Aieta, P. Genevet, M. A. Kats, Z. Gaburro, and F. Capasso, "A broadband, background-free quarter-wave plate based on plasmonic metasurfaces," *Nano letters*, vol. 12, no. 12, pp. 6328–6333, 2012. 20

[20] J. B. Mueller, K. Leosson, and F. Capasso, "Ultracompact metasurface in-line polarimeter," *Optica*, vol. 3, no. 1, pp. 42–47, 2016. 20

[21] F. Ding, Y. Chen, and S. I. Bozhevolnyi, "Metasurface-based polarimeters," *Applied Sciences*, vol. 8, no. 4, p. 594, 2018. 20

[22] Y. F. Yu, A. Y. Zhu, R. Paniagua-Domínguez, Y. H. Fu, B. Luk'yanchuk, and A. I. Kuznetsov, "High-transmission dielectric metasurface with 2π phase control at visible wavelengths," *Laser & Photonics Reviews*, vol. 9, no. 4, pp. 412–418, 2015. 20

[23] L. Wang, S. Kruk, H. Tang, T. Li, I. Kravchenko, D. N. Neshev, and Y. S. Kivshar, "Grayscale transparent metasurface holograms," *Optica*, vol. 3, no. 12, pp. 1504–1505, 2016. 20

[24] C. Huygens, *Traité de la lumière*. Pieter van der Aa, 1960. 20

[25] R. Dezert, *Theoretical study of isotropic Huygens particles for metasurfaces*. PhD thesis, Université de Bordeaux, 2019. xiii, 20, 21

[26] W. Liu and Y. S. Kivshar, "Generalized kerker effects in nanophotonics and meta-optics," *Optics express*, vol. 26, no. 10, pp. 13085–13105, 2018. xiv, 22, 23, 24

[27] Y. H. Fu, A. I. Kuznetsov, A. E. Miroshnichenko, Y. F. Yu, and B. Luk'yanchuk, "Directional visible light scattering by silicon nanoparticles," *Nature communications*, vol. 4, no. 1, pp. 1–6, 2013. xv, 22, 32, 33

[28] A. B. Evlyukhin, S. M. Novikov, U. Zywietz, R. L. Eriksen, C. Reinhardt, S. I. Bozhevolnyi, and B. N. Chichkov, "Demonstration of magnetic dipole resonances of dielectric nanospheres in the visible region," *Nano letters*, vol. 12, no. 7, pp. 3749–3755, 2012. 22

[29] B. Rolly, B. Stout, and N. Bonod, "Boosting the directivity of optical antennas with magnetic and electric dipolar resonant particles," *Optics Express*, vol. 20, no. 18, pp. 20376–20386, 2012. 22

[30] S. Linden, C. Enkrich, M. Wegener, J. Zhou, T. Koschny, and C. M. Soukoulis, "Magnetic response of metamaterials at 100 terahertz," *Science*, vol. 306, no. 5700, pp. 1351–1353, 2004. 22

[31] I. M. Hancu, A. G. Curto, M. Castro-López, M. Kuttge, and N. F. van Hulst, "Multipolar interference for directed light emission," *Nano letters*, vol. 14, no. 1, pp. 166–171, 2014. 22

[32] M. Kerker, D.-S. Wang, and C. Giles, "Electromagnetic scattering by magnetic spheres," *JOSA*, vol. 73, no. 6, pp. 765–767, 1983. 22, 23

[33] M. Decker and I. Staude, "Resonant dielectric nanostructures: a low-loss platform for functional nanophotonics," *Journal of Optics*, vol. 18, no. 10, p. 103001, 2016. xiv, 22

[34] R. Dezert, P. Richetti, and A. Baron, "Complete multipolar description of reflection and transmission across a metasurface for perfect absorption of light," *Optics express*, vol. 27, no. 19, pp. 26317–26330, 2019. 23

[35] W. Liu, J. Zhang, B. Lei, H. Ma, W. Xie, and H. Hu, "Ultra-directional forward scattering by individual core-shell nanoparticles," *Optics express*, vol. 22, no. 13, pp. 16178–16187, 2014. xiv, 23

[36] C. M. Watts, X. Liu, and W. J. Padilla, "Metamaterial electromagnetic wave absorbers (adv. mater. 23/2012)," *Advanced Materials*, vol. 24, no. 23, pp. OP181–OP181, 2012. 24

[37] D. G. Baranov, A. Krasnok, T. Shegai, A. Alù, and Y. Chong, "Coherent perfect absorbers: linear control of light with light," *Nature Reviews Materials*, vol. 2, no. 12, pp. 1–14, 2017. 24

[38] K. Aydin, V. E. Ferry, R. M. Briggs, and H. A. Atwater, "Broadband polarization-independent resonant light absorption using ultrathin plasmonic super absorbers," *Nature communications*, vol. 2, no. 1, pp. 1–7, 2011. 24

[39] H.-T. Chen, J. Zhou, J. F. O'Hara, F. Chen, A. K. Azad, and A. J. Taylor, "Antireflection coating using metamaterials and identification of its mechanism," *Physical review letters*, vol. 105, no. 7, p. 073901, 2010. 24

[40] C.-H. Sun, P. Jiang, and B. Jiang, "Broadband moth-eye antireflection coatings on silicon," *Applied Physics Letters*, vol. 92, no. 6, p. 061112, 2008. 24

[41] S. Collin, "Nanostructure arrays in free-space: optical properties and applications," *Reports on Progress in Physics*, vol. 77, no. 12, p. 126402, 2014. 24

[42] P. Lalanne and P. Chavel, "Metalenses at visible wavelengths: past, present, perspectives," *Laser & Photonics Reviews*, vol. 11, no. 3, p. 1600295, 2017. 24

[43] M. L. De Marco, S. Semlali, B. A. Korgel, P. Barois, G. L. Drisko, and C. Aymonier, "Silicon-based dielectric metamaterials: Focus on the current synthetic challenges," *Angewandte Chemie International Edition*, vol. 57, no. 17, pp. 4478–4498, 2018. xiv, 25

[44] I. Staude, A. E. Miroshnichenko, M. Decker, N. T. Fofang, S. Liu, E. Gonzales, J. Dominguez, T. S. Luk, D. N. Neshev, I. Brener, *et al.*, "Tailoring directional scattering through magnetic and electric resonances in subwavelength silicon nanodisks," *ACS nano*, vol. 7, no. 9, pp. 7824–7832, 2013. 25

[45] M. Kolíbal, T. Matlocha, T. Vystavěl, and T. Šikola, "Low energy focused ion beam milling of silicon and germanium nanostructures," *Nanotechnology*, vol. 22, no. 10, p. 105304, 2011. 25

[46] A. I. Kuznetsov, A. E. Miroshnichenko, Y. H. Fu, J. Zhang, and B. Luk'Yanchuk, "Magnetic light," *Scientific reports*, vol. 2, p. 492, 2012. xv, 25, 32

[47] U. Zywietz, A. B. Evlyukhin, C. Reinhardt, and B. N. Chichkov, "Laser printing of silicon nanoparticles with resonant optical electric and magnetic responses," *Nature communications*, vol. 5, no. 1, pp. 1–7, 2014. xiv, 25, 26

[48] M. Celebrano, M. Baselli, M. Bollani, J. Frigerio, A. Bahgat Shehata, A. Della Frera, A. Tosi, A. Farina, F. Pezzoli, J. Osmond, *et al.*, "Emission engineering in germanium nanoresonators," *Acs Photonics*, vol. 2, no. 1, pp. 53–59, 2015. 25

[49] S. Liu, M. B. Sinclair, S. Saravi, G. A. Keeler, Y. Yang, J. Reno, G. M. Peake, F. Setzpfandt, I. Staude, T. Pertsch, *et al.*, "Resonantly enhanced second-harmonic generation using iii–v semiconductor all-dielectric metasurfaces," *Nano letters*, vol. 16, no. 9, pp. 5426–5432, 2016. 25

[50] Z.-J. Yang, R. Jiang, X. Zhuo, Y.-M. Xie, J. Wang, and H.-Q. Lin, "Dielectric nanoresonators for light manipulation," *Physics Reports*, vol. 701, pp. 1–50, 2017. 25

[51] C. Simovski and S. Tretyakov, "Model of isotropic resonant magnetism in the visible range based on core-shell clusters," *Physical Review B*, vol. 79, no. 4, p. 045111, 2009. xiv, 26

[52] V. Ponsinet, P. Barois, S. M. Gali, P. Richetti, J.-B. Salmon, A. Vallecchi, M. Albani, A. Le Beulze, S. Gomez-Grana, E. Duguet, *et al.*, "Resonant isotropic optical magnetism of plasmonic nanoclusters in visible light," *Physical Review B*, vol. 92, no. 22, p. 220414, 2015. xv, 27, 29, 30, 32

[53] S. Mühlig, A. Cunningham, S. Scheeler, C. Pacholski, T. Bürgi, C. Rockstuhl, and F. Lederer, "Self-assembled plasmonic core–shell clusters with an isotropic magnetic dipole response in the visible range," *ACS nano*, vol. 5, no. 8, pp. 6586–6592, 2011. xiv, 27

[54] S. N. Sheikholeslami, H. Alaeian, A. L. Koh, and J. A. Dionne, "A metafluid exhibiting strong optical magnetism," *Nano letters*, vol. 13, no. 9, pp. 4137–4141, 2013. xiv, xv, 27, 30, 31

[55] S. Gómez-Graña, A. Le Beulze, M. Treguer-Delapierre, S. Mornet, E. Duguet, E. Grana, E. Cloutet, G. Hadziioannou, J. Leng, J.-B. Salmon, *et al.*, "Hierarchical self-assembly of a bulk metamaterial enables isotropic magnetic permeability at optical frequencies," *Materials Horizons*, vol. 3, no. 6, pp. 596–601, 2016. xiv, 27, 31

[56] V. Many, R. Dézert, E. Duguet, A. Baron, V. Jangid, V. Ponsinet, S. Ravaine, P. Richetti, P. Barois, and M. Tréguer-Delapierre, "High optical magnetism of dodecahedral plasmonic meta-atoms," *Nanophotonics*, vol. 8, no. 4, pp. 549–558, 2019. xiv, 27, 31

[57] C. Rockstuhl, F. Lederer, C. Etrich, T. Pertsch, and T. Scharf, "Design of an artificial three-dimensional composite metamaterial with magnetic resonances in the visible range of the electromagnetic spectrum," *Physical review letters*, vol. 99, no. 1, p. 017401, 2007. 28

[58] A. B. Evlyukhin, C. Reinhardt, and B. N. Chichkov, "Multipole light scattering by nonspherical nanoparticles in the discrete dipole approximation," *Physical Review B*, vol. 84, no. 23, p. 235429, 2011. 28

[59] R. Dezert, P. Richetti, and A. Baron, "Isotropic huygens dipoles and multipoles with colloidal particles," *Physical Review B*, vol. 96, no. 18, p. 180201, 2017. xiv, 28

[60] M. R. Bourgeois, A. T. Liu, M. B. Ross, J. M. Berlin, and G. C. Schatz, "Self-assembled plasmonic metamolecules exhibiting tunable magnetic response at optical frequencies," *The Journal of Physical Chemistry C*, vol. 121, no. 29, pp. 15915–15921, 2017. xiv, 28, 29

[61] S. Mühlig, C. Rockstuhl, V. Yannopapas, T. Bürgi, N. Shalkevich, and F. Lederer, "Optical properties of a fabricated self-assembled bottom-up bulk metamaterial," *Optics express*, vol. 19, no. 10, pp. 9607–9616, 2011. 28, 29

[62] J. H. Lee, Q. Wu, and W. Park, "Metal nanocluster metamaterial fabricated by the colloidal self-assembly," *Optics letters*, vol. 34, no. 4, pp. 443–445, 2009. xiv, xv, 28, 29, 33, 34

[63] Y.-l. Xu, "Electromagnetic scattering by an aggregate of spheres," *Applied optics*, vol. 34, no. 21, pp. 4573–4588, 1995. 29

[64] Y. Cho, J.-H. Huh, K. J. Park, K. Kim, J. Lee, and S. Lee, "Using highly uniform and smooth selenium colloids as low-loss magnetodielectric building blocks of optical metafluids," *Optics express*, vol. 25, no. 12, pp. 13822–13833, 2017. 29

[65] A. Vallecchi, M. Albani, and F. Capolino, "Collective electric and magnetic plasmonic resonances in spherical nanoclusters," *Optics Express*, vol. 19, no. 3, pp. 2754–2772, 2011. 29

[66] N. L. Sharma, "Nondipole optical scattering from liquids and nanoparticles," *Physical review letters*, vol. 98, no. 21, p. 217402, 2007. xiv, 30, 31

[67] R. M. Azzam, N. M. Bashara, and S. S. Ballard, "Ellipsometry and polarized light," *PhT*, vol. 31, no. 11, p. 72, 1978. 33

[68] M. Kildemo, X. Wang, V. Ponsinet, D. Chiappe, and F. B. de Mongeot, "Optical properties of self-assembled plasmonic hyperbolic metasurfaces and metamaterials extracted by (mueller matrix) spectroscopic ellipsometry," in *2016 10th International Congress on Advanced Electromagnetic Materials in Microwaves and Optics (METAMATERIALS)*, pp. 172–174, IEEE, 2016. 33

[69] G. Baraldi, M. García Pardo, J. Gonzalo, R. Serna, and J. Toudert, "Self-assembled nanostructured photonic-plasmonic metasurfaces for high-resolution optical thermometry," *Advanced Materials Interfaces*, vol. 5, no. 12, p. 1800241, 2018. 33

[70] N. Karl, M. S. Heimbeck, H. O. Everitt, H.-T. Chen, A. J. Taylor, I. Brener, A. Benz, J. L. Reno, R. Mendis, and D. M. Mittleman, "Characterization of an active metasurface using terahertz ellipsometry," *Applied Physics Letters*, vol. 111, no. 19, p. 191101, 2017. 33

[71] C. Durand-Gasselin, N. Sanson, and N. Lequeux, "Reversible controlled assembly of thermosensitive polymer-coated gold nanoparticles," *Langmuir*, vol. 27, no. 20, pp. 12329–12335, 2011. xv, 34, 35

[72] J. He, X. Huang, Y.-C. Li, Y. Liu, T. Babu, M. A. Aronova, S. Wang, Z. Lu, X. Chen, and Z. Nie, "Self-assembly of amphiphilic plasmonic micelle-like nanoparticles in selective solvents," *Journal of the American Chemical Society*, vol. 135, no. 21, pp. 7974–7984, 2013. xv, 34, 35

[73] A. Sánchez-Iglesias, M. Grzelczak, T. Altantzis, B. Goris, J. Perez-Juste, S. Bals, G. Van Tendeloo, S. H. Donaldson Jr, B. F. Chmelka, J. N. Israelachvili, *et al.*, "Hydrophobic interactions modulate self-assembly of nanoparticles," *ACS nano*, vol. 6, no. 12, pp. 11059–11065, 2012. xv, 34, 35

[74] L. Chen and H.-A. Klok, ""multifaceted" polymer coated, gold nanoparticles," *Soft Matter*, vol. 9, no. 45, pp. 10678–10688, 2013. xv, 35

[75] A. K. Boal, F. Ilhan, J. E. DeRouchey, T. Thurn-Albrecht, T. P. Russell, and V. M. Rotello, "Self-assembly of nanoparticles into structured spherical and network aggregates," *Nature*, vol. 404, no. 6779, pp. 746–748, 2000. 35

[76] J.-F. Berret, "Controlling electrostatic co-assembly using ion-containing copolymers: From surfactants to nanoparticles," *Advances in colloid and interface science*, vol. 167, no. 1-2, pp. 38–48, 2011. xv, 35

[77] Q. Yin, X. Han, V. Ponsinet, and H. Liu, "Controlled assembly of plasmonic nanoparticles using neutral-charged diblock copolymers," *Journal of colloid and interface science*, vol. 431, pp. 97–104, 2014. xv, 35

[78] Y.-S. Cho, G.-R. Yi, S.-H. Kim, D. J. Pine, and S.-M. Yang, "Colloidal clusters of microspheres from water-in-oil emulsions," *Chemistry of materials*, vol. 17, no. 20, pp. 5006–5013, 2005. xv, 35, 37

[79] H. K. Yu, G.-R. Yi, J.-H. Kang, Y.-S. Cho, V. N. Manoharan, D. J. Pine, and S.-M. Yang, "Surfactant-assisted synthesis of uniform titania microspheres and their clusters," *Chemistry of Materials*, vol. 20, no. 8, pp. 2704–2710, 2008. 35

[80] J. Lacava, P. Born, and T. Kraus, "Nanoparticle clusters with lennard-jones geometries," *Nano letters*, vol. 12, no. 6, pp. 3279–3282, 2012. xv, 35, 36, 38

[81] J. Schmitt, S. Hajiw, A. Lecchi, J. Degrouard, A. Salonen, M. Impéror-Clerc, and B. Pansu, "Formation of superlattices of gold nanoparticles using ostwald ripening in emulsions: transition from fcc to bcc structure," *The Journal of Physical Chemistry B*, vol. 120, no. 25, pp. 5759–5766, 2016. xv, 35, 37, 39

[82] I. Hussain, H. Zhang, M. Brust, J. Barauskas, and A. I. Cooper, "Emulsions-directed assembly of gold nanoparticles to molecularly-linked and size-controlled spherical aggregates," *Journal of colloid and interface science*, vol. 350, no. 1, pp. 368–372, 2010. 35

[83] Z. Lu and Y. Yin, "Colloidal nanoparticle clusters: functional materials by design," *Chemical Society Reviews*, vol. 41, no. 21, pp. 6874–6887, 2012. xv, 36

[84] J. Northby, "Structure and binding of lennard-jones clusters: 13≤ n≤ 147," *The Journal of chemical physics*, vol. 87, no. 10, pp. 6166–6177, 1987. 36

[85] S.-H. Kim, S. Y. Lee, G.-R. Yi, D. J. Pine, and S.-M. Yang, "Microwave-assisted self-organization of colloidal particles in confining aqueous droplets," *Journal of the American Chemical Society*, vol. 128, no. 33, pp. 10897–10904, 2006. xv, 36, 38

[86] V. N. Manoharan, "Colloidal spheres confined by liquid droplets: Geometry, physics, and physical chemistry," *Solid state communications*, vol. 139, no. 11-12, pp. 557–561, 2006. xv, 36, 37, 39

Chapter 2

Experimental techniques

Contents

Summary: This chapter provides a brief background on the different analytical tools used in this thesis to study the structure and optical properties of clusters of gold nanoparticles. This chapter also introduces the fabrication method and tools used for the synthesis of gold nanoparticle clusters.

2.1 Light scattering techniques

2.1.1 Dynamic light scattering

2.1.1.1 Background

Dynamic light scattering (DLS) is a technique used to measure the size and size distribution of colloidal particles suspended in a solution. DLS measures the characteristic time of diffusion of particles submitted to Brownian motion. Brownian motion, which is the random movement of the particles suspended in a solution, arises due to the collision between particles and the liquid molecules surrounding them. The size of the particles is estimated using the relationship between the diffusion coefficient and the particles size. This technique was used in this study to measure the size of individual gold NPs and gold NP clusters.

2.1.1.2 Measurement technique

The DLS measurements were carried out on particles suspended in a fluid (water or oil) of known viscosity. The measurement technique involves illuminating the sample with a primary source of light using a monochromatic laser. This induces an oscillating polarization of the outer electrons in the molecules of the sample. The oscillating electrons emit EM radiations in all directions.This radiation is also known as the secondary or scattered wave. The light scattered by different molecules interfere to give an interference pattern, which contains quantitative information about the spatial arrangement of the scattering objects. The particles suspended in a solution are under constant movement due to Brownian motion and this causes the interference pattern to changes as a function of time. This change is measured to estimate how fast the particles are moving in the fluid environment.

The change in the interference pattern is measured in terms of change in intensity fluctuations of the scattered light as a function of time. The ability of the scattering objects to move due to Brownian motion is defined by its translational diffusion coefficient (D) [$m^2.s^{-1}$] which is expressed as shown below:

$$\mathrm{D} = \frac{k\,\mathrm{T}}{6\,\pi\,\eta\,\mathrm{R_H}} \tag{2.1}$$

where, k, T, η, and $\mathrm{R_H}$ correspond to Boltzmann constant ($1.38\times10^{-23}\ m^2.kg.s^{-2}.\mathrm{K}^{-1}$), temperature [K], viscosity [Pa.s] and hydrodynamic radius [m] respectively. The hydrodynamic radius is the radius of the sphere that has the same translational diffusion coefficient as the scattering object. The estimated $\mathrm{R_H}$ from DLS can be bigger than the actual particle size since it not only depends on the size of the particle but also on the surface structure. For instance, an absorbed polymer layer projecting into the suspension will re-

duce the diffusion speed and therefore increase the R_H of the particles as shown in Fig: 2.1 a. The fluctuations in scattering intensity can thus be directly related to the size of the particles. The smaller particles move faster in a given solution when compared to larger particles and therefore their intensity fluctuates more rapidly as shown in Fig: 2.1 b.

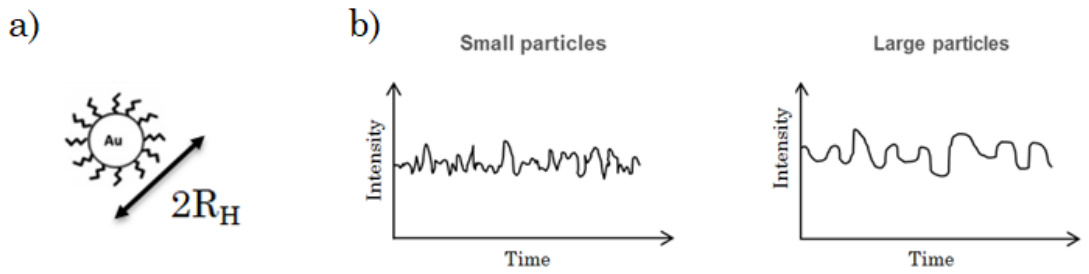

Figure 2.1: a) Dependence of R_H on the surface structure of the particle b) Comparison of intensity fluctuations spectra of a small and large particles in a given solution.

A digital autocorrelator is used to analyze the intensity fluctuations spectra. The correlator compares the intensity of the scattered light at time t and a small time later $t+\delta t$. The correlation of the scattering intensity reduces with time and above a characteristic time τ_c correlation are no longer observed in the system (Fig: 2.2).

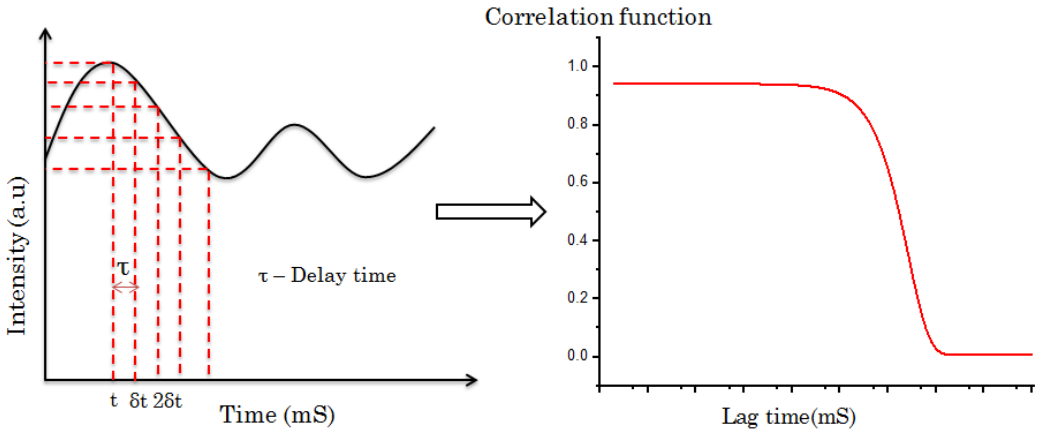

Figure 2.2: Fluctuation in scattering intensity on the left and typical correlogram on the right. Perfect correlation is indicated by unity and no correlation is indicated by zero.

The correlation function for a monodisperse suspension of particles is expressed as an exponential decay function of the decay time τ:

$$G(\tau) = A + B\exp(-\frac{\tau}{\tau_c}) \tag{2.2}$$

where, A is the baseline, B is the intercept, τ_c is the characteristic diffusion time such that $\tau_c = \frac{1}{2Dq^2}$. And the wave vector q reads:

$$q = \frac{4\pi n}{\lambda}\sin\frac{\theta}{2} \tag{2.3}$$

where, n, λ and θ are the refractive index of the dispersant, wavelength of the source and scattering angle respectively.

2.1.1.3 Particle size determination

The size and size distribution determination is less straight forward when dealing with polydisperse particles. In such cases, the size of the particles form the correlation curve can be obtained by using different algorithms [1]. These algorithms are based on two main methods: 1) A single exponential fit of the correlation curve to produce the mean size and an estimate of the polydispersity index. This is known as the Cumulant analysis method [2, 3]. 2) A fit of the data to a multiple exponential function that will permit to extract the particle size distribution.

The size of individual gold NPs suspended in water were measured using an ALV laser goniometer, with a 632.8 nm HeNe linearly polarized laser and an ALV5000/EPP multiple tau digital correlator. The DLS autocorrelation function was obtained at a scattering angle of 150° and at a temperature of 25 °C. The intensity–weighted relaxation time distributions were obtained using the CONTIN processing method. A single, relaxation mode corresponding to the translational diffusion of particles was found in that case.

To determine the size and polydispersity of gold NP clusters, with typical sizes close to the wavelength value, the autocorrelation functions were measured at several scattering angles (30°, 50°, 70°, 90°, 110°, 130° and 150°). The resulting correlation functions were analyzed using a second order cumulant expansion [4] as shown below:

$$\mathrm{I}_2(t) = \mathrm{I}_1^2(0) + \mathrm{I}_1^2(0)\,\exp\left[-2\mathrm{K}_1 t + \mathrm{K}_2 t\right] \tag{2.4}$$

where $\mathrm{I}_1^2(0)$ is the square of the correlation function of the electric field E at $t = 0$, and K_1 and K_2 are the first and second cumulants: K_1 is a characteristic relaxation frequency, and K_2 represents the deviation from a mono exponential decay [5].

When plotting the first cumulant K_1 vs q^2, one obtains a straight line with a slope corresponding to D. For a polydisperse system the average diffusion coefficient $< \mathrm{D} >$ is expressed as:

$$< \mathrm{D} > = \frac{k\,\mathrm{T} < \mathrm{R}^5 >}{6\,\pi\,\eta < \mathrm{R}^6 >} \tag{2.5}$$

The second cumulant K_2 is defined by,

$$\mathrm{K}_2 = q^4\,(< \mathrm{D}^2 > - < \mathrm{D} >^2) \tag{2.6a}$$

$$\mathrm{K}_2 = \left(\frac{k\,\mathrm{T}}{6\,\pi\,\eta}\right)^2 q^4\,\frac{< \mathrm{R}^4 >< \mathrm{R}^6 > - < \mathrm{R}^5 >^2}{< \mathrm{R}^6 >^2} \tag{2.6b}$$

Where $< R^n >$ is the moment of order n of the size distribution.

The gold NP clusters obtained from the bulk emulsion process have a polydispersity expected to follow a log-normal distribution (explained in Section 2.1.2). The probability density function (PDF), P(R) of a log-normal distribution is expressed in terms of the mean size (R_o) and the standard deviation (σ):

$$P(R) = \frac{1}{R\,\sigma\,2\,\pi}\exp\left(-\frac{Ln^2\,\frac{R}{R_o}}{2\,\sigma^2}\right) \tag{2.7}$$

R_o and σ are obtained by solving Equations 2.5 and 2.6 using the moments of log-normal distribution to obtain:

$$< R^n > = R_o^n \exp\left(\frac{n^2\sigma^2}{2}\right) \tag{2.8a}$$

$$\frac{K_1}{q^2} = \left[\frac{k\,T}{6\,\pi\,\eta}\right]\left[\frac{1}{R_o}\exp\left(\frac{-11}{2}\,\sigma^2\right)\right] \tag{2.8b}$$

$$\frac{K_2}{q^4} = \left[\frac{k\,T}{6\,\pi\,\eta}\right]^2\left[\exp(\sigma^2) - 1\right]\left[\frac{1}{R_o}\exp\left(\frac{-11}{2}\sigma^2\right)\right]^2 \tag{2.8c}$$

Using the value R_o and σ obtained from the above equations, the size distribution of the clusters is plotted using Equ: 2.7. Figure: 2.3 shows a model plot of the PDF of gold clusters with a most probable radius R_o = 120 nm and a standard deviation σ = 0.15.

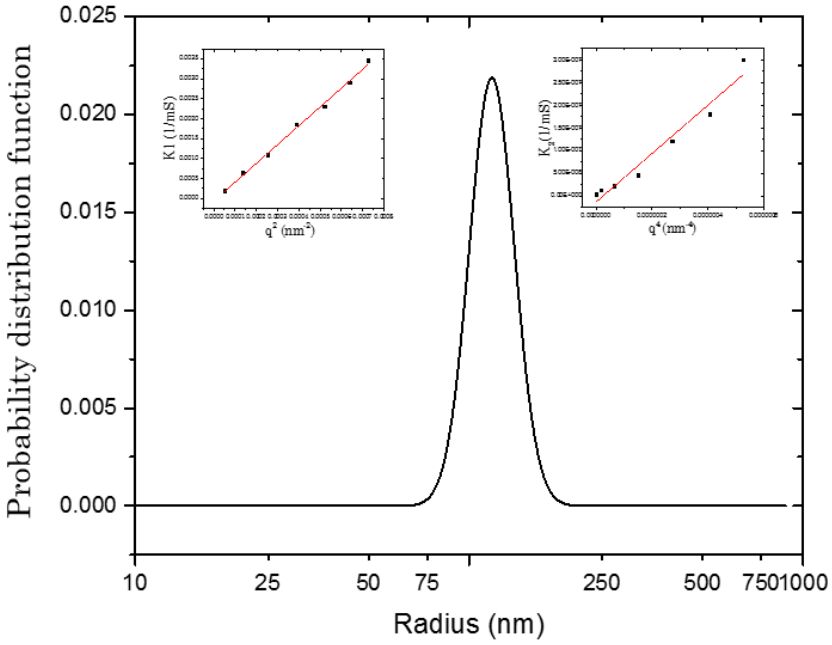

Figure 2.3: PDF of gold clusters. Insert: (left) K_1 vs q^2 and (right) K_2 vs q^4

.

2.1.2 Granulometry

2.1.2.1 Introduction

Granulometry, with a Malvern Nano-ZS, was used for the measurement of the initial emulsions droplet size distribution, as they were too turbid to be studied with the DLS setup. Granulometry uses Mie theory of light scattering to calculate the particle size distribution. It measures particle size distributions by measuring the angular variation in intensity of light scattered as a laser beam passes through a dispersed particulate sample.

2.1.2.2 Measurement setup and analysis

A schematic illustration of the setup used for the particle size analysis is shown in Fig 2.4. Dodecane is used as the dispersant for the measurement of the size of water droplets in a water-in-oil emulsion. A few drops of the emulsion is added to the dispersant and a laser beam (blue light) is passed through the dispersion. Large particles scatter light at small angles relative to the laser beam and small particles scatter light at large angles. Scattering of particles with the same size, in the same plane of scattering is superimposed on the detector.

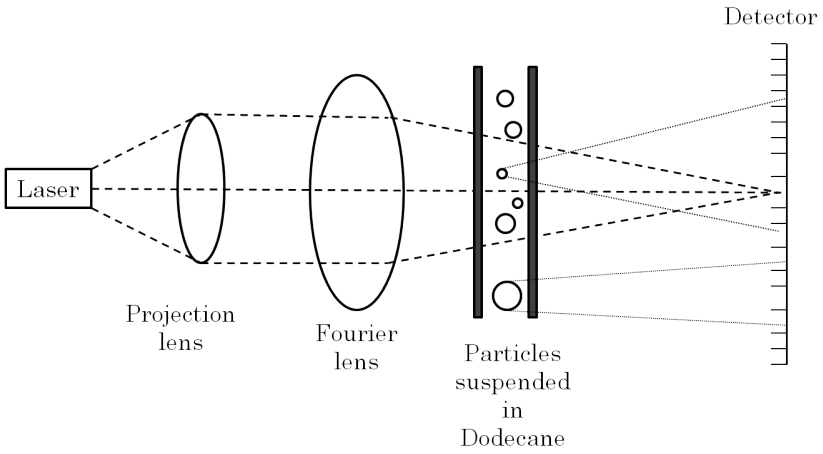

Figure 2.4: Basic schematic of a granulometry setup

The size of the water droplets dispersed in the dispersant is then analyzed using the software Mastersizer 2000. Optical index of the dispersant and the particles are taken into account by the software and using Mie theory, the size of the particles is calculated. The particle size is reported as a volume equivalent sphere diameter.

The volume averaged diameter of the water droplets (d_w) is expressed as

$$d_w = \mathrm{D}(4,3)\,\frac{\sum_i \mathrm{V}_i d_i}{\sum_i \mathrm{V}_i} = \frac{\sum_i \mathrm{N}_i d_i^4}{\sum_i \mathrm{N}_i d_i^3} \tag{2.9}$$

where V_i and N_i are the volume and the number of d_i diameter droplets respectively. The polydispersity can be defined as follow

$$P = \frac{1}{d}\frac{\sum_i N_i d_i |d - d_i|}{\sum_i N_i d_i^3} \tag{2.10}$$

Where P is the polydispersity index and d is the median diameter.

2.1.3 Static light scattering

2.1.3.1 Introduction

The static light scattering (SLS) technique is used to study the scattering properties of the gold NP clusters suspended in a solution. In contrast with DLS, which evaluates the instantaneous fluctuations of the scattered intensity as a function of time, SLS measures the absolute scattering intensity averaged over time. SLS measurements were first performed at a scattering angle $\theta = \pi/2$ to distinguish the scattering due to electric dipolar resonance and magnetic dipolar and/or electric quadrapolar resonances. The setup was then modified to span the scattering angles from $\theta = 20°$ to $140°$, this gave access to measure the complete scattering of the clusters and its directionality. These additional data can give access to the detailed multipolar modes of the scattering of the gold clusters, provided a model is available.

2.1.3.2 Experimental setup

The static light scattering (SLS) setup (shown in Fig: 2.5) includes a supercontinuum white source (SuperK EXB-6 with SuperK Split UV-visible filter from NKT Photonics) used to deliver a light beam covering the 440-900 nm wavelength range onto a dilute suspension of scatterers. The linear polarization plane of the incident light was rotated by a Fresnel rhomb tandem (Thorlabs FR600HM) mounted on a rotation stage. The incident polarization angle is ϕ. The polarization of the scattered light was selected by a Glan-Taylor polarizer (Thorlabs GL10-A) set perpendicular or parallel to the scattering plane. The scattered light was collected through a collimated fiber (NA = 0.25) by a spectrometer (Hamamatsu C10083CA) mounted on a goniometer, in order to span scattering angles θ from $20°$ to $140°$.

2.1.3.3 Data acquisition and analysis

The scattering properties of dilute suspensions of gold Np clusters across the whole visible spectrum were first studied at a scattering angle $\theta = 90°$. The incident field E_i propagating along the z axis is linearly polarized in the (x, y) plane at an angle $\frac{\pi}{2} - \phi$ from the scattering plane (y, z). The light scattered parallel ($E_{\parallel s}$) and perpendicular ($E_{\perp s}$) to the scattering plane is collected using the spectrometer.

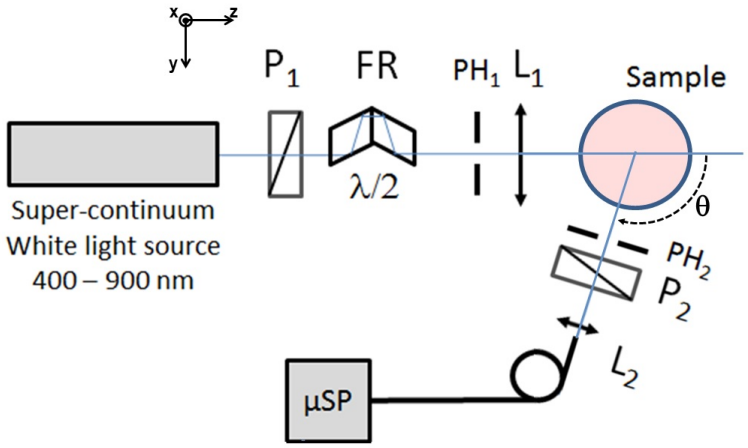

Figure 2.5: Schematic illustration of the static light scattering setup. P1 and P2 are broadband polarizers, FR is a Fresnel rhomb tandem, L1 and L2 are lenses and PH1 and PH2 are pinholes. μSP is a spectrophotometer. θ is the scattering angle and varies from 20 to 140.

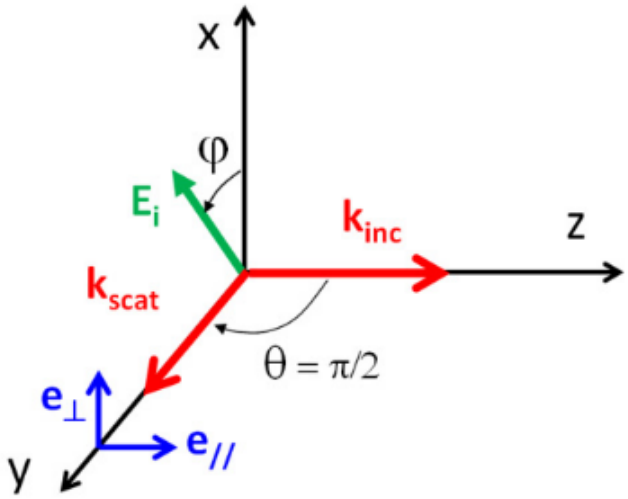

Figure 2.6: Schematic view of the light scattering geometry at θ = 90°

The relationship between the incident field and the scattered field is expressed in a matrix form [6]:

$$\begin{pmatrix} E_{\parallel S} \\ E_{\perp S} \end{pmatrix} = \frac{e^{ikr}}{-ikr} \begin{pmatrix} S_2(\theta,\phi) & S_4(\theta,\phi) \\ S_3(\theta,\phi) & S_1(\theta,\phi) \end{pmatrix} \begin{pmatrix} E_i \cos\phi \\ E_i \sin\phi \end{pmatrix} \tag{2.11}$$

S_j represents the amplitude scattering matrix, and is a function of θ and ϕ. However, for isotropic scatterers S_j does not depend on ϕ and the non diagonal terms S_3 and S_4 vanish [7]. The scattering angle dependence of S_j is expressed using angle dependent

functions π_n and τ_n [6], which read as:

$$\pi_n = \frac{2n-1}{n-1}\mu\pi_{n-1} - \frac{n}{n-1}\pi_{n-2} \tag{2.12a}$$

$$\tau_n = n\mu\pi_n - (n+1)\pi_{n-1} \tag{2.12b}$$

where, $\mu = \cos\theta$. The scattered field is the superposition of the normal modes with coefficient a_n and b_n (also known as Mie coefficients). Therefore for each n, there are two distinctive modes each representing the magnetic (b_n) and electric modes (a_n).

$$S_1 = \sum_n \frac{2n+1}{n(n+1)}(a_n\pi_n + b_n\tau_n) \tag{2.13a}$$

$$S_2 = \sum_n \frac{2n+1}{n(n+1)}(a_n\tau_n + b_n\pi_n) \tag{2.13b}$$

The measurement at a scattering angle of $\theta = 90°$ allows to assess the strength of the optical magnetism of the scatterers. At this scattering angle, the scattering coefficients are simply related to the electric dipole ED (a_1) and magnetic quadrupole MQ (b_2) for S_1, and the magnetic dipole MD (b_1) and the electric quadrupole EQ (a_2) for S_2. Contribution from higher order multipoles were neglected since simulations showed us (for the typical size and volume fraction of clusters under analysis) that other high order multipoles are either too low or absent. Therefore by restricting to only dipoles and quadrupoles ($n \leq 2$), the following expressions of S_1 and S_2 are obtained:

$$S_1 \approx \frac{3}{2}a_1 - \frac{5}{2}b_2 \tag{2.14a}$$

$$S_2 \approx \frac{3}{2}b_1 - \frac{5}{2}a_2 \tag{2.14b}$$

The intensities measured along the two output polarizations for isotropic scatterers then read:

$$I_{\perp S} = I_0(\lambda)\, n_c\, \frac{|S_1(90°)|^2}{k^2}\, \delta\Omega\, T(\lambda)\, g(\lambda, \delta\Omega) \cos^2\phi = A_V(\lambda) \cos^2\phi \tag{2.15a}$$

$$I_{\parallel S} = I_0(\lambda)\, n_c\, \frac{|S_2(90°)|^2}{k^2}\, \delta\Omega\, T(\lambda)\, g(\lambda, \delta\Omega) \sin^2\phi = A_H(\lambda) \sin^2\phi \tag{2.15b}$$

in which $I_0(\lambda)$ is the spectral irradiance of the incident beam, n_c is the number of clus-

ters in the scattering volume, and $\delta\Omega$ is the solid angle of the detection window. $g(\lambda, \delta\Omega)$ is an unknown function that accounts for the spectral sensitivity of the detector and optical transmission or reflection of all optical elements. The spectral transmission $T(\lambda)$ accounts for the absorbance of the suspension.

The intensities in both polarizations is measured with varying ϕ angle from the x direction by steps of 10° for each wavelength ranging from 400 to 800 nm. A model graph representing the measured perpendicular and parallel signal for a cluster of gold NPs at wavelength λ = 660 nm is plotted on Fig: 2.7 (left) and the plots are also fitted to the following simple functions:

$$I_{\perp S} = B_V + A_V \cos^2\phi \tag{2.16a}$$

$$I_{\parallel S} = B_H + A_H \sin^2\phi \tag{2.16b}$$

The background signal B, identical for the two functions, does not exceed a few percent (at most 5% across the wavelength range) of the amplitude A_V, which fully validates the assumption of isotropic scatterers [8]. The values of A_H and A_V are extracted for all studied wavelengths, and their ratio is plotted as a function of the wavelength on Fig: 2.7 (right)

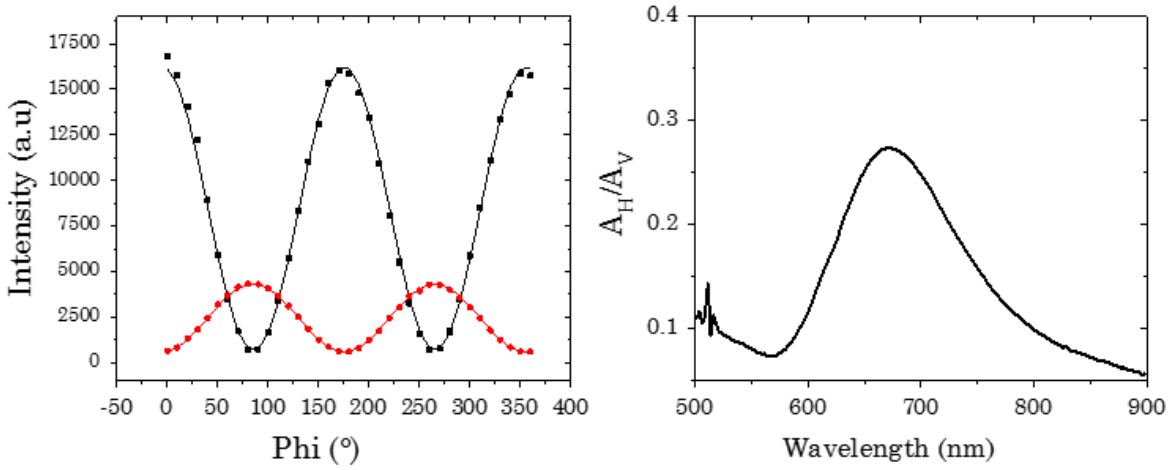

Figure 2.7: (left) Measured intensity (symbols) as a function of the incident polarization angle ϕ with output polarizations perpendicular (black squares) and parallel (red circles) to the scattering plane at a wavelength λ = 660 nm and a scattering angle $\theta = 90°$. Simple fits (lines) of $A_V \cos^2\phi + B$ (black) and $A_H \sin^2\phi + B$ (red). (right) Experimental ratio of A_H (intensity measured parallel to the scattering plane) to A_V (intensity measured orthogonal to the scattering plane) as a function of the wavelength λ.

To extract the contribution of MD+EQ and ED+MQ modes separately, the measured intensities were normalized with a reference dispersion of silica NPs in water or ethanol. Silica NPs were used as the model dispersion due to the ease of their synthesis with a high

precision in their particle size. The scattering cross section of silica NPs for a given size is then calculated using Mie theory [6]. The scattering intensities measured for samples (gold NP clusters) in both polarizations are normalized using the intensity measured for silica in the perpendicular polarization $I_{\perp ref}$, since at scattering angle $\theta = 90°$ silica does not exhibit any MD (from Mie theory).

The reference signals were collected using the same experimental conditions as the ones used for the samples. Therefore the quantities $I_0(\lambda)$, $\delta\Omega$ and $g(\lambda, \delta\Omega)$ are the same for the sample as well as the reference. Dividing Equation 2.15 for measured intensities for the sample by the reference yields the differential scattering cross sections (σ) of the sample along the particular direction (θ,ϕ):

$$\sigma_{\perp}(\theta = 90°) = \frac{\left|S_1(\theta = 90°)\right|}{k^2} = K\frac{A_V(\lambda)T_{ref}(\lambda)}{A_V^{ref}(\lambda)T(\lambda)}\sigma_{ref}^{\theta=90°} \tag{2.17a}$$

$$\sigma_{\parallel}(\theta = 90°) = \frac{\left|S_2(\theta = 90°)\right|}{k^2} = K\frac{A_H(\lambda)T_{ref}(\lambda)}{A_H^{ref}(\lambda)T(\lambda)}\sigma_{ref}^{\theta=90°} \tag{2.17b}$$

where, $K = \frac{n_c}{n_{ref}}$ is the ratio of scatterers concentration in the sample (n_c) and the reference silica system (n_{ref}), it is a constant independent of wavelength. The ratio $\frac{T_{ref}(\lambda)}{T(\lambda)}$ is simply equal to 1 since transmission of highly diluted samples are dominated by the solvent. A model plot of the extracted scattering cross section for both polarizations are shown in Figure 2.8. Their absolute values cannot be extracted from the experimental data because the concentrations of clusters and reference silica beads in the respective suspensions are not known. However, we fully determine the spectral positions and relative amplitudes of the two resonant modes.

The measurements recorded at this scattering angle ($\theta = 90°$) indicate the presence of the MD resonance. The relative amplitude as well as the spectral position of the MD resonance with respect to the ED resonance cannot be estimated due to the significant presence of the EQ mode. As stated in Section 1.2.1, directional scattering properties are only obtained when both the dipolar modes resonate in the same frequency with equal amplitude. Therefore to study the directional scattering properties of the clusters, the SLS setup was modified to allow the scattering angle to be varied between 20° (forward scattering) to 140° (backward scattering).

The precision of the setup at all scattering angles was first checked using the model dispersion of silica NPs in a solvent. The ratio of the scattering intensities A_H/A_V for silica particles (much smaller than the wavelength) as a function of scattering angle θ follows a simple function (from Mie theory):

$$\frac{A_H}{A_V} = \cos^2\theta \tag{2.18}$$

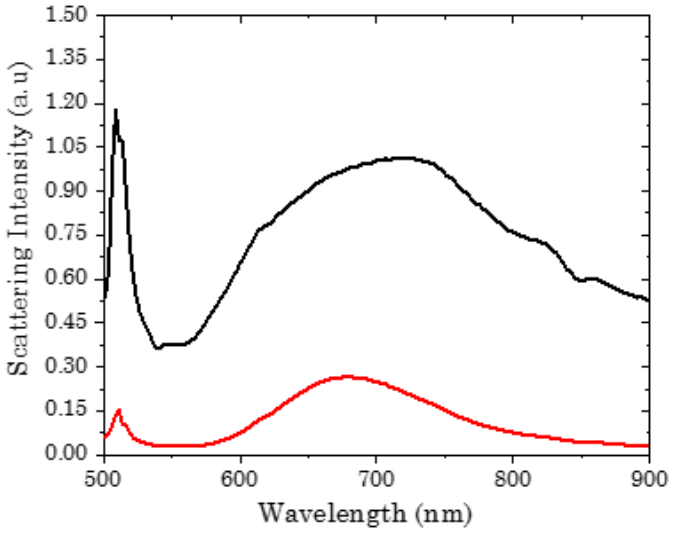

Figure 2.8: The scattering cross section extracted for ED+MQ (black lines) and MD+EQ (red lines) for a suspension of gold NP clusters in dodecane.

The plot representing the experimental ratio and theoretical values are shown in Figure 2.9. The plot indicates a good overlap between the experimental and theoretical data.

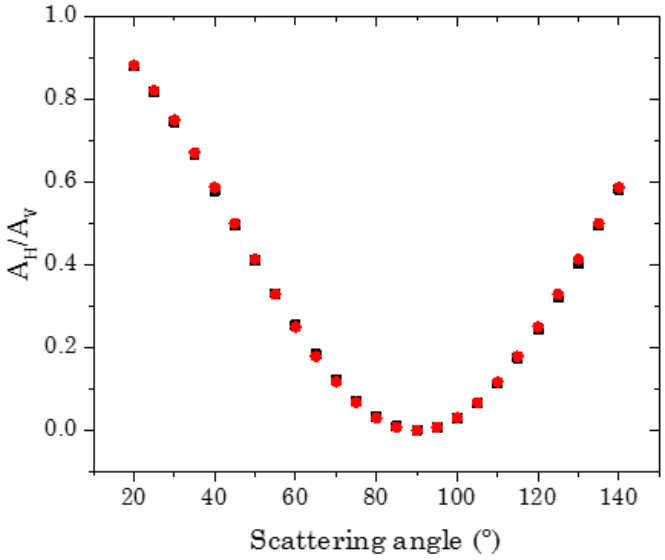

Figure 2.9: Experimental (black square) and expected values (red dots) of the ratio of A_H/A_V.

The scattering intensities for the two polarizations, $I_{SV}(\phi,\theta)$ and $I_{SH}(\phi,\theta)$, for scattering angles $\theta = 20°$ to $140°$ with an interval of $\theta = 5°$ are measured for all values of the wavelength (λ). These measured values were all fitted to Equation 2.16, from which we extract $A_V(\lambda,\theta)$ and $A_H(\lambda,\theta)$, using the same normalization with a model dispersion of colloidal silica as before.

The extracted data are then used to build a polar plot for different wavelengths which will further be explained in Section 4.1.2. It is not possible to measure the scattering in-

tensities below $\theta = 20^\circ$ since the influence from the direct beam is hard to avoid. It is also not possible to go beyond $\theta = 140^\circ$ due to the limit of the setup.

The total scattering intensities ($A_V(\lambda,\theta)+A_H(\lambda,\theta)$) for each angle as a function of wavelength is plotted using a polar plot to indicate the directional scattering properties (also shown in Section 4.1.2).

The directional scattering properties can also be indicated using an assymetry parameter (g) which can be estimated from the polar plots. g is calculated by taking a sum of total scattering intensity (VH+VV) at each scatting angle and multiply with $\cos\theta$. Since the value $\cos\theta$ is positive for $\theta < 90$ and negative for $\theta > 90$, the sign of the summation will indicate the degree of forward scattering.

$$g =< \cos\theta >= \frac{\sum_{20}^{140} (VH + VV) \sin\theta \cos\theta}{\sum_{20}^{140} (VH + VV) \sin\theta} \tag{2.19}$$

where,

- $g = 0$ for all isotropic scatterers,
- g is positive for forward scattering and
- g is negative for backward scattering

2.2 Small Angle X-Ray Scattering

2.2.1 Background

Small angle x-ray scattering (SAXS) is a non-destructive analytical tool used to determine the structure of a system in terms of averaged particles size, shapes and interaction within the system. Systems that can be analyzed using SAXS include solids, liquids or a combination of both materials. In general, an X-ray radiation is passed through the sample and every particle that happens to be inside the beam scatter the incident radiation in all directions. An average is taken over all objects and over all orientations of the objects to produce an average value that depends on their structure. SAXS measures the scattering intensities at scattering angles very close to zero. This angular range contains information regarding the structure of the scattering objects at sizes typically comprised between 0.5 nm and 100 nm, which includes for example nano and microparticles, and macromolecules among others. In this study, SAXS profiles were obtained for gold NPs suspension and clusters of gold NPs suspensions, to study their size and structure.

2.2.2 Working principle

When an X-ray radiation encounters a medium, two main phenomena may occur: scattering and absorption. A fraction of the radiation passes through the sample, a fraction gets absorbed and transferred into other forms of energy (heat, fluorescence, etc.) and a fraction will be scattered into other directions of propagation. Scattering can occur with or without energy loss (inelastic or elastic scattering respectively), that is, the scattered radiation can have the same or different frequency than the incident radiation. The former is known as elastic scattering and the scattered radiation has no phase relation with the incident radiation.

Elastic scattering occurs when the electrons start oscillating at the same frequency as the incident radiation. These oscillating electrons emit a secondary source of radiation with the same frequency as the incident radiation. The scattered waves emitted by the neighbouring atoms interfere at the detector to produce an interference pattern. The interference can be constructive (in phase), destructive (out of phase) or in-between depending upon the scattering angle and the distance r at which they are measured. A constructive interference causes a bright spot at the detector and a destructive interference causes a dark spot at the detector. This results in a 2D interference pattern with varying intensity as a function of position in the detector. This interference pattern contains the information on orientation and distance of atoms relative to each other.

SAXS produces structural information on objects whose size range is typically comprised between 0.5 nm and 100 nm [9]. The scattering intensity (I) in SAXS experiments are measured as a function of the scattering wavevector q that reads:

$$q = \frac{4\pi}{\lambda}\sin(\frac{\theta}{2}) \tag{2.20}$$

where λ [nm] is the wavelength of the incident radiation, θ [°] is the scattering angle (angle between the incident and scattered beam). The dimension of q is $\frac{1}{\text{nm}}$. The scattering intensity $I(q)$ depends upon the electron density ρ of the system. The higher the electron density, the higher is the $I(q)$. For instance, if the sample is composed of a very dilute suspension of particles with a volume V and electron density ρ, the scattering intensity can be expressed as:

$$I(q) = I_o.\rho^2.V^2.P(q) \tag{2.21}$$

where, $P(q)$ is the form factor of the particles, which by definition only depends on the size and shape of the particles (further discussed in Section 2.2.4.1 below), and I_o is the intensity of the incident beam. By "very dilute", we mean a solution in which any incident ray is only scattered once before exiting the sample area. SAXS can also be used to study the interaction between the particles within the suspension in case of a concentrated sample suspension.

2.2.3 SAXS instrumentation and data acquisition

During the course of my PhD, two different SAXS instruments were used to analyse the sample. For each SAXS profile, the instrument used will be indicated as either SAXS 1 or SAXS 2.

SAXS 1:

SAXS profiles were acquired in transmission on a Nanostar-U device (Bruker SAXS) with a copper anode source, Goebel mirrors and a HiSTAR 2-D detector giving access to scattering vector q values from 0.1 to 8 nm^{-1}. The resulting 2D images were found to be isotropic, and the data were azimuthally averaged to yield the scattering curve of the intensity I(q) corrected from experimental background versus $q = (4\pi/\lambda)\sin(\theta/2)$, where $\lambda = 0.154$ nm is the wavelength of the Cu Kα radiation and θ is the scattering angle. The scattering profiles for both individual NPs suspension and gold NP clusters suspension are acquired by exposing the samples for 16 hrs.

SAXS 2:

SAXS profiles were acquired in transmission on a XEUSS device (Xenocs) with a microfocus copper anode source, a scatterless collimation system and a PILATUS 2-D detector, giving access to scattering wavevector q values ranging from 0.08 to 8 nm^{-1}. The scattering intensity of dilute suspensions of gold NPs suspended in water and dilute suspensions of clusters of gold NPs suspended in oil (silicone oil or dodecane) were recorded. The sample suspensions were put in thin glass capillaries. The resulting 2D images were found to be isotropic, and the data were azimuthally averaged to yield the scattering curve of the intensity I(q), corrected from experimental background, versus $q = (4\pi/\lambda)\sin(\theta/2)$, where $\lambda = 0.154$ nm is the wavelength of the Cu Kα radiation and θ is the scattering angle.

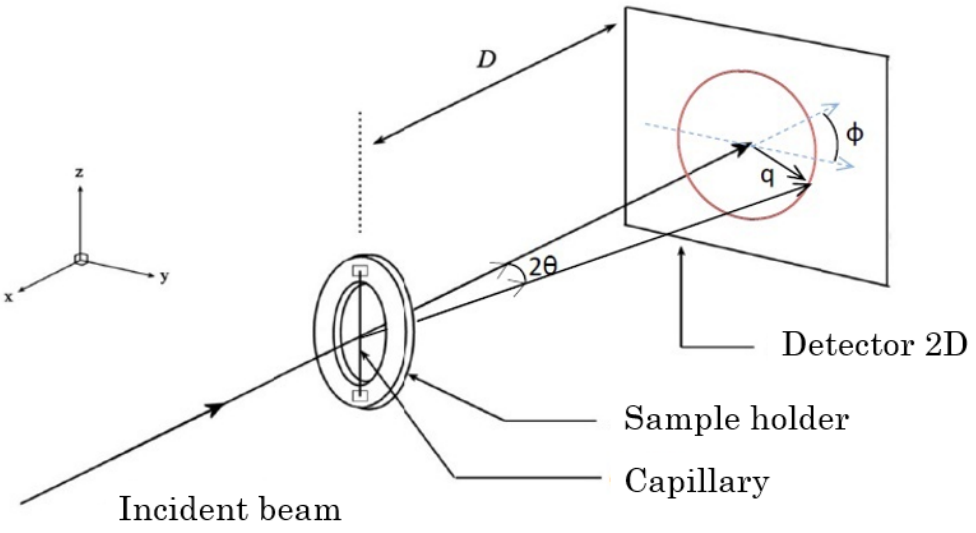

Figure 2.10: Schematic illustration of the SAXS instrument used for data acquisition.

2.2.4 Data analysis

In the case when the concentration of the sample is no longer dilute enough, the recorded scattered intensity may contain some information on the form factor as well on what is called the structure factor of the particles (further in Section 2.2.4.2 below). In that case, the expression of the scattered intensity reads:

$$\mathrm{I}(q) = \mathrm{P}(q).\mathrm{S}(q) \tag{2.22}$$

where $\mathrm{P}(q)$ and $\mathrm{S}(q)$ represent the form and the structure factor of the suspended particles respectively.

2.2.4.1 Form factor

The form factor $\mathrm{P}(q)$ describes the scattering from a single particle, which strongly depends on its size and shape. The scattering of one particle, which is made of many atoms, can be explained as the interference pattern produced at the detector when the scattered wave from each atom/electron interfere. In practice, many particles are illuminated at the same time and thus the theoretical form factor must be scaled to match the experimental data.

The theoretical form factor of a sphere of radius r is expressed as:

$$\mathrm{P}(q,r) = \frac{(\sin(qr) - qr\cos(qr))^2}{q^6}, \tag{2.23}$$

Which can be convoluted with a Gaussian size distribution in order to describe a dispersion of particles

$$\mathrm{D}(r, r_s) = \frac{1}{\sigma\sqrt{2\pi}}\exp\left(-\frac{(r-r_s)^2}{2\sigma^2}\right), \tag{2.24}$$

where r_s is the average size of the particle and σ is the size distribution of the particles. If all the illuminated particles are identical in shape and size, and the particles are far away from each other with no interaction among them, then the scattering pattern is simply the form factor multiplied by the number of particles. In the case of a polydisperse dispersion, the form factor of all the particles are summed to obtain an average scattering pattern.

As an example, we present the calculated scattering intensity $\mathrm{I}(q) \approx \mathrm{P}(q)$ for spherical particles of radius $r_s = 6.7$ nm using Equation 2.23 on Figure 2.11.

2.2.4.2 Structure factor

When a system of densely packed particles are irradiated with x-ray, the correlations between particles give rise to additional contributions to the interference pattern apart from

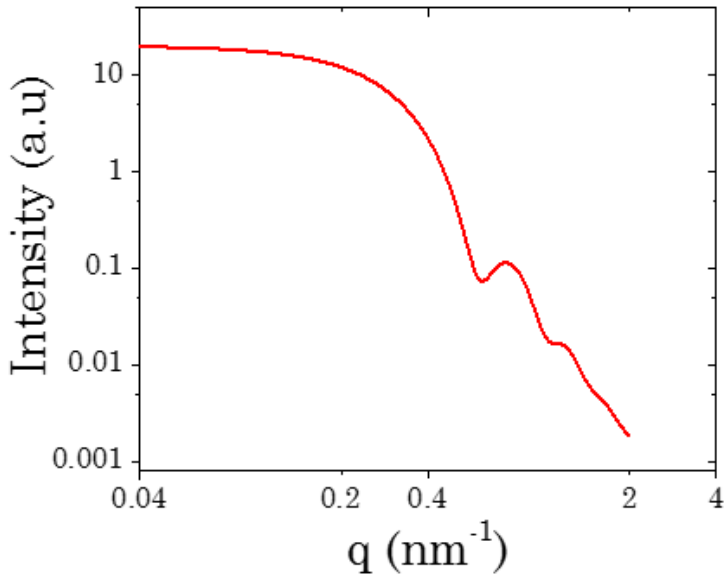

Figure 2.11: Form factor of a sphere with r_s = 6.7 nm and σ = 1nm

the P(q). This additional contribution factor is known as the structure factor and contains information on the position and interactions of the particles with respect to each other. For example, a repulsive interaction between the particles leads to a decrease in the scattering intensity at q values corresponding to the distance between the particles. On the contrary, an increase in the intensity indicates an attractive interaction, which may cause the aggregation of the particles in the solution [10]. The aggregation of particles eventually leads to a sharp scattering peak when the particles align themselves into an ordered (or quasi ordered) arrangement. This peak is known as the Bragg peak and the position of its maximum (q_{peak}) indicates the center to center distance (d_{Bragg}) (nm) between the particles:

$$d_{\text{Bragg}} = \frac{2\pi}{q_{\text{peak}}} \tag{2.25}$$

As gold NPs are assembled in a dense clusters, a Bragg peak is observed that leads to the average aggregating distance of the NPs in the clusters. For example, Fig. 2.12 presents the observed Bragg peak in clusters of gold NPs constituted of methoxy poly(ethylene glycol) thiols (PEG-SH) (800 g/mol) covered NPs. We used this technique to study the internal structure of the gold NP clusters made of NPs capped with different polymers and polymer molecular weights in Chapter 3.

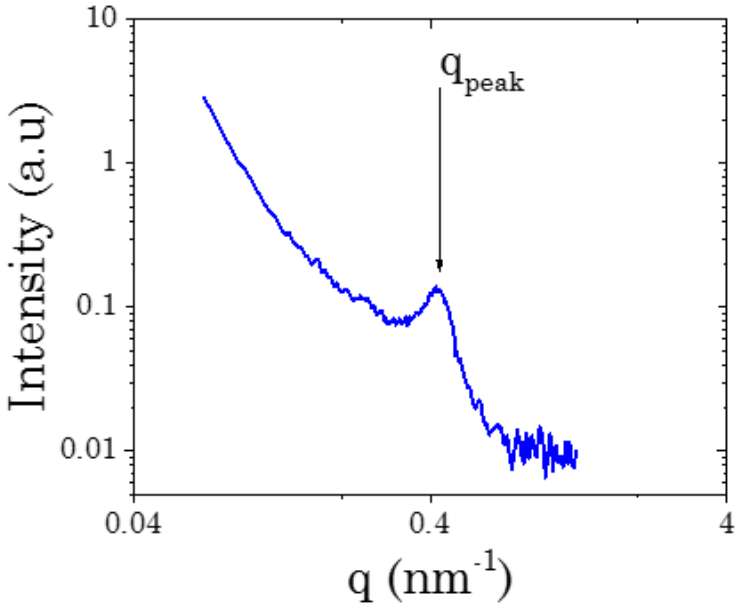

Figure 2.12: Graph indicating the Bragg peak for clusters of gold NPs capped with PEG (800 g/mol). Obtained using SAXS 2

2.3 Spectroscopic techniques

2.3.1 UV-Vis spectroscopy

UV-Visible spectroscopy is a type of absorption spectroscopy which measures the attenuation of a beam of light (in the UV/Vis part of the spectrum) after passing through a sample. The spectrometer works on the principle of Beer-Lambert law which states that the absorbance A of light is directly proportional to the sample path length l and the concentration c of the absorbing specie as follows:

$$A = \log(\frac{I_0}{I}) = \epsilon\, l\, c \tag{2.26}$$

where, ϵ is the molar extinction coefficient of the studied species, I_o and I are the incident and transmitted light intensities respectively.

Due to the presence of a surface plasmon resonance, metallic NPs exhibit a sharp absorption peak in the visible spectrum, which is characteristic of their chemical nature, size, shape and optical index of their environment. Spherical gold NPs have an absorption peak around 520 nm and exhibit a Stokes shift when their size or the refractive index of their surrounding medium is altered. In this study, UV-Vis spectroscopy was used to study the optical characteristics of both gold NPs and clusters of gold NPs suspended in a solution, and to calculate the concentration of gold NPs dispersed in water. The measurements were carried out using a UV-Visible Jasco V-730 spectroscope in the wavelength range from 350 to 800 nm. The sample suspensions were studied in PMMA cells with 1 cm optical path and a pure solvent cell was used as a reference.

2.3.2 ATR-FTIR spectroscopy

Attenuated Total Reflectance-Fourier Transform Infra-Red spectroscopy (ATR-FTIR) is a type of IR spectroscopy where the sample is analyzed directly in the liquid or solid state without any sample preparation. In ATR-FTIR spectroscopy the sample is in contact with the ATR crystal, the IR radiation travels through the crystal and interacts with the sample that is in contact with the ATR crystal. Because of the differences in refractive indices (n_1 and n_2) of both materials, total internal reflection occurs as the ray exhibits an angle larger than the total reflection limit angle $\theta_L = \text{Arc sin}(\frac{n_2}{n_1})$. In such case only an evanescent wave is formed that exponentially decay in the direction perpendicular to the interface.

2.3.2.1 Principle of ATR-FTIR

The sample is placed on the ATR crystal (typically made of a high refractive index material). Upon total reflection of the incident light at the interface where the crystal touches the sample, a small fraction of the light extends into the sample as an evanescent wave. Based on the composition of the sample, a small part of the infrared light is absorbed when the evanescent wave interacts with the sample, resulting in a slightly attenuated total reflection. Therefore by analyzing the totally reflected IR light, information on the composition of the sample can be obtained.

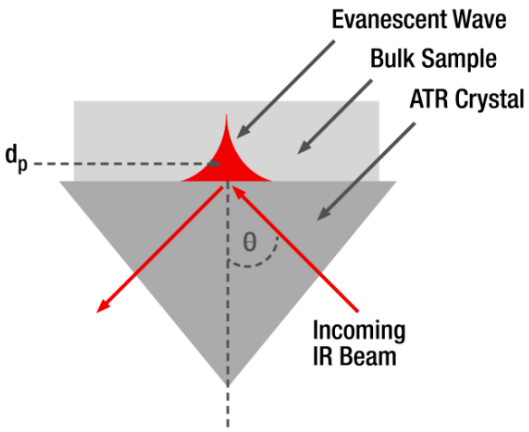

Figure 2.13: Schematic illustration of total internal reflection at the surface of a ATR crystal

The penetration depth is a measure of how far the evanescent wave extends into the sample, it is calculated using the equation shown below:

$$d_p = \frac{\lambda}{2\pi n_1 \sqrt{\sin^2(\theta_i) - (\frac{n_2}{n_1})^2}} \tag{2.27}$$

where, λ denotes the wavelength, n_1 and n_2 are the refractive index of the germanium crystal ($n_1 = 4.052$ at $\lambda = 2.8\mu m$) and the sample respectively. The d_p was calculated to be ≈ 0.14 µm at $\lambda = 2.873$ µm (for both silicone oil, $n_2 = 1.52$, and dodecane, $n_2 = 1.42$).

Infra-red spectroscopy in the ATR-FTIR mode was performed using a Nicolet 6700 spectrometer Thermo Scientific equipped with a MCT detector cooled at 77K. For each spectrum, 200 scans were recorded at a resolution of 8 cm^{-1}. The IR radiation is directed on a germanium crystal at an incidence angle $\theta = 45°$, above the critical angle.

ATR-FTIR setup was used in this study to estimate the volume fraction of water in the emulsion as a function of ripening time. IR was chosen since the influence of scattering is low at high frequency.

2.4 Electron Microscopy

In this thesis, electron microscopy techniques were employed to obtain images of individual NPs as well as clusters of NPs to study their size, shape and structure.

2.4.1 Transmission Electron microscopy

Transmission electron microscopy (TEM) employs a high energy beam of electrons through a very thin sample. The interaction between the electron beam and the sample is used to produce high resolution black and white images. The TEM operates on the same basic principles as the light microscope but uses electrons instead of light. Because the wavelength of electrons is much smaller than that of light, the optimal resolution attainable for TEM images is about 2 to 3 orders of magnitude higher than that from a light microscope. And since the electron beam cross through the sample, TEM can be used to study the inner structure of the sample, such as its crystalline structure, morphology etc.

In order to ensure the transmission of electrons through the sample it has to be very thin and as flat as possible. Therefore, the sample preparation is very crucial in a TEM experiment. To obtain TEM images of individual gold NPs, a few drops of the NPs solution (gold NPs suspended in water), are deposited on a copper grid. Once the water is completely evaporated, the samples are ready to be viewed under the electron beam.

The sample preparation of clusters of gold NPs is more complicated than individual particles. The clusters are dispersed in an oil solution which can be much harder to completely eliminate before its exposure to the electron beam. Therefore a solvent exchange method was employed to completely exchange the oil solution with a volatile fluid such as Hexane. This was achieved by centrifugating the cluster solution and replacing the supernatant with Hexane. This process was repeated twice to ensure the complete exchange of solvents. The final solution of clusters dispersed in hexane is used to prepare the copper grids. Although TEM gives a rough estimate of the structure of the clusters, the harsh treatment of the sample during the sample preparation could have altered the structure. Moreover, the effect of capillary forces on the clusters during the drying process is unclear.

2.4.2 Cryo-Transmission Electron microscopy

Cryo-transmission electron microscopy technique (CRYO-TEM) was employed by Oren Regev and Einat Nativ-Roth at the University of Beer Sheva (Israel) to study the structure of clusters of gold NPs in the liquid phase. Unlike TEM, the samples do not undergo vigorous centrifugation step, instead they are frozen in their liquid state and directly viewed under the electron beam.

Samples for Cryo-TEM imaging were prepared using a fully automated vitrification device (Leica, EM GP). First, 3 µL of the cluster suspension in dodecane was deposited onto a glow discharged 300 Mesh Cu grid covered with a lacey-carbon film (Ted Pella, 01883-F) held inside a 100% humidity chamber. The grid was then mechanically blotted and immediately plunged into liquid ethane cooled by liquid nitrogen in order to vitrify the dodecane. The frozen grid was mounted in a Gatan cryo-TEM holder, and examined at low dose below −175 °C in a FEI Talos S200C microscope operated at 200 kV. Images were collected using a Ceta camera (4k x 4k) and analyzed using Digital Micrograph Gatan Inc. software.

2.5 Synthesis of gold nanoparticles

Colloidal solutions of gold NPs dispersed in water were synthesized using the Turkevich method [11]. Turkevich method is based on chemical reduction of gold salt ($HAuCl_4$,$3H_2O$) to metallic gold atoms which then form nucleation centers and grow into NPs. The synthesis is performed at 100°C and sodium citrate is used as a reducing agent. In fact sodium citrate has two main roles in this synthesis process: 1) it reduces the gold salt ($HAuCl_4$,$3H_2O$) then, 2) it acts as a ligand in order to stabilize the NPs.

The ratio of gold salt ($HAuCl_4$,$3H_2O$) to sodium citrate determines the size of the gold NPs. In this study, a ratio of 3.5: 1 was used, which allows us to obtain objects with a radius of about 6.5 nm and a very narrow size distribution.

2.5.1 Synthesis steps

Cleaning: The glass beakers necessary for the synthesis of gold nanoparticles were first thoroughly rinsed using aqua regia (1/3 HNO_3 ; 2/3 HCL), followed by deionised water.

- 0.5 Molarity solution of gold salt is prepared by adding 0.14 g of $HAuCl_4$ in 0.7 ml of water.
- 500 mL of ultra-pure water is heated using a hot plate until it reaches boiling point,
- 0.246 mL of 0.5M of gold solution is added to the boiling water

- Once the water reaches boiling point again, 3 mL of 0.385 g of sodium citrate in 9 mL of water, is added to the boiling water under vigorous stirring.

The solution initially turns into a dark purple color indicating the formation gold NPs. The temperature and agitation is maintained till the solution reaches a bright red colour. The solution is allowed to cool down and the size and volume fraction is calculated using different methods. Transmission electron microscopy image of the synthesized gold NPs is shown in Figure 2.14.

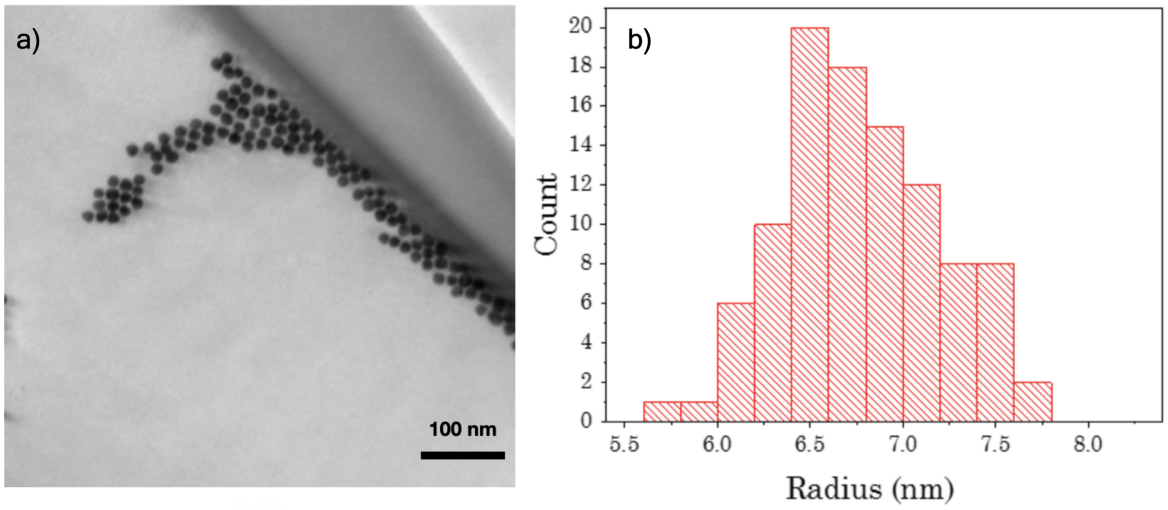

Figure 2.14: a) TEM image of the synthesized gold NPs. b) Size distribution of gold NPs estimated from TEM images.

2.5.1.1 Calculation of volume fraction

Molecular weight of gold salt = 393.83 g/mol

Mass of salt used = 0.14 g x $\frac{0.246\ \text{ml}}{0.7\ \text{ml}}$ = 0.0492 g

$N_{salt} = \frac{0.0492}{393.83} = 1.2\text{x}10^{-4}$ mol = $N_{\mathring{A}u}$

Molecular weight of gold = 196.97 g/mol

Mass of gold used = 1.2 x 10^{-4} x 196.97 = 0.0246 g

Density of gold = 19.32 g/cm^3

Volume of gold = $\frac{0.0246\ \text{g}}{19.32\ \text{g}/cm^3}$ = 1.27x10^{-3} ml

Volume fraction og gold in water = $\frac{1.27x10^{-3}}{500}$ = 2.5x10^{-6}

This synthesis produces a suspension with gold volume fraction approximately 2.5 x 10^{-6}. The experimental value of volume fraction is calculated using Uv-Vis spectroscopy.

2.6 Emulsification Technique

Emulsions are heterogeneous mixtures of at least two immiscible liquids, generally, water and oil, one of which is dispersed as droplets throughout the other liquid phase by an external energy source. The phase existing as small droplets is called the dispersed phase and the surrounding liquid is known as the continuous phase. An emulsion is most often described as either oil-in-water (O/W) or water-in-oil (W/O) where the first phase mentioned, refers to the dispersed phase.

In this thesis, water-in-oil emulsions were used to fabricate clusters of gold NPs. The emulsions were created using two techniques, namely the bulk emulsion technique and microfluidics.

All the bulk emulsions in this study were performed using a Ultraturax mixer (T-18) which creates a mechanical stirring. The speed of agitation was fixed at 1000 rpm for all emulsions. The water-in-oil emulsions were obtained by first mixing the oil solution (continuous phase) with the surfactant. The water solution was then added drop wise under vigorous agitation. The resulting emulsion was characterized using optical microscopy and granulometry.

Monodisperse water-in-oil emulsions were also produced using a glass microfluidic chip. The resulting emulsions were characterized using an optical microscope. The glass chips were purchased from Micronit Microtechnologies.

2.7 Reference

[1] J. Jakeš, “Regularized positive exponential sum (repes) program-a way of inverting laplace transform data obtained by dynamic light scattering,” *Collection of Czechoslovak chemical communications*, vol. 60, no. 11, pp. 1781–1797, 1995. 52

[2] R. Pecora, *Dynamic light scattering: applications of photon correlation spectroscopy*. Springer Science & Business Media, 2013. 52

[3] D. E. Koppel, “Analysis of macromolecular polydispersity in intensity correlation

spectroscopy: the method of cumulants," *The Journal of Chemical Physics*, vol. 57, no. 11, pp. 4814–4820, 1972. 52

[4] P. Fabre, C. Quilliet, M. Veyssié, F. Nallet, D. Roux, V. Cabuil, and R. Massart, "Anisotropy of the diffusion coefficients of submicronic particles embedded in lamellar phases," *EPL (Europhysics Letters)*, vol. 20, no. 3, p. 229, 1992. 52

[5] B. J. Berne and R. Pecora, *Dynamic light scattering: with applications to chemistry, biology, and physics*. Courier Corporation, 2000. 52

[6] C. F. Bohren and D. R. Huffman, *Absorption and scattering of light by small particles*. John Wiley & Sons, 2008. 56, 57, 59

[7] N. L. Sharma, "Nondipole optical scattering from liquids and nanoparticles," *Physical review letters*, vol. 98, no. 21, p. 217402, 2007. 56

[8] S. Gomez-Graña, M. Treguer-Delapierre, E. Duguet, J. Salmon, J. Leng, V. Kravets, A. Grigorenko, A. Peyyety, V. Ponsinet, P. Richetti, *et al.*, "Isotropic 3d optical magnetism in visible light in a self-assembled metamaterial," in *2016 10th International Congress on Advanced Electromagnetic Materials in Microwaves and Optics (METAMATERIALS)*, pp. 52–54, IEEE, 2016. 58

[9] O. M. Londoño, P. Tancredi, P. Rivas, D. Muraca, L. M. Socolovsky, and M. Knobel, "Small-angle x-ray scattering to analyze the morphological properties of nanoparticulated systems," in *Handbook of Materials Characterization*, pp. 37–75, Springer, 2018. 62

[10] H. Singh, *The SAXS Guide- Getting Acquainted with the Principles*. Anton Paar: Graz, Austria, 2013. 65

[11] B. Rodríguez-González, P. Mulvaney, and L. M. Liz-Marzán, "An electrochemical model for gold colloid formation via citrate reduction," *Zeitschrift für Physikalische Chemie*, vol. 221, no. 3, pp. 415–426, 2007. 69

Chapter 3

Formulation of clusters

Contents

Summary: This chapter will provide a detailed account on the fabrication route employed to synthesis clusters of gold nanoparticles which can further be used as optical resonators. The first part of this chapter focuses on the bulk emulsification technique, which results in the production of large quantities of gold NP clusters with a polydispersity in size. The second part of this chapter will detail the challenges faced while using the microfluidic technology to produce a monodisperse cluster suspension.

3.1 Introduction

In this study, clusters of gold NPs were synthesized using a water-in-oil emulsion based formulation route. The fabrication technique employed can be divided into two main steps: the first step involves emulsifying a liquid suspension of gold NPs (water phase, average diameter d_{NP} ≈14 nm) to create droplets (of diameter $d_{droplets}$ ≈8 µm) of this suspension in an oil phase using surfactant molecules. In the second step, the size of the water droplets is reduced in a controlled manner, by evaporating the water using a rotavapor, to bring the NPs closer to each other and form the final clusters. A schematic illustration of the formulation technique is shown in Figure 3.1.

The surface of the individual NPs composing the final clusters were covered by two different polymers namely, polyvinylpyrrolidone (PVP) and methoxy poly(ethylene glycol) thiol (PEG-SH) and their influence on the stability of the NPs suspension as well as on the final volume fraction of the cluster were studied. The surface modification of the NPs is a required step of the process as the polymer layers prevents direct contact between particles within the clusters, which is a condition to retain the SPR properties of the individual NPs [1]. Indeed, the SPR is essential to obtain the targeted optical properties.

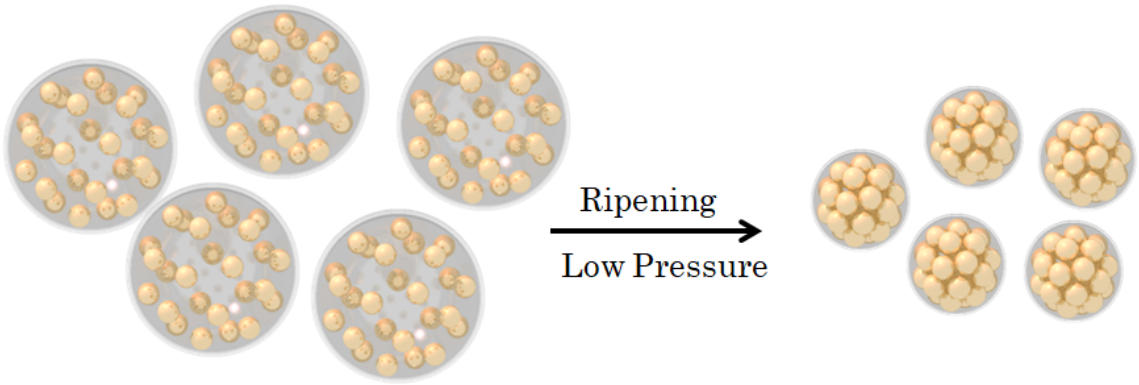

Figure 3.1: Schematic illustration of the NP cluster formulation route.

3.2 Formulation and ripening of the emulsions

3.2.1 Formulation parameters

The first step of the cluster fabrication technique involves the formulation of stable water-in-oil emulsions, which is obtained with the help of adapted surfactant molecules. Surfactants are amphiphilic molecules, which contain both a hydrophilic (polar) head group and a hydrophobic (non-polar) tail. Therefore, surfactants are attracted to both polar and non-polar compounds and adsorb at the oil-water interface. In this way, surfactants lower the interfacial tension between the oil and water phases, stabilizing the droplets and preventing them from coalescing. The stability of emulsions largely depends upon the ability

of the surfactant to cover the water droplet surface.

Continuous phase	Surfactant chemical formula	Surfactant commercial name /and source	Emulsion stability
Polydiméthylsiloxane	Mixture of Cyclopentasiloxane and PEG/PPG-18/18	DC 5225c /Dow Corning	stable
Polydiméthylsiloxane	Polyethylene glycol oleyl ether	Brij 93	unstable*
Polydiméthylsiloxane	PEG 10 Dimethicone	KF6017 / Shin Etsu	stable
Polydiméthylsiloxane	PEG 9 Polydiméthylsiloxane Dimethicone	KF6028 / Shin Etsu	stable
Polydiméthylsiloxane	Polyglyceryl-3 Polydiméthylsiloxane Dimethicone	KF6104 / Shin Etsu	stable
Dodecane	-	KF6104 / Shin Etsu	unstable
Dodecane	-	DC 5225c	stable
Dodecane	Oligomeric ester based surfactant	Hypermer	stable
Hexadecane	Sorbitan mono oleate	Span80	unstable*
Hexadecane	-	Brij 93	unstable
Hexadecane	PEG-PPG-PEG	PL121	unstable

Table 3.1: Table indicating different surfactants and continuous phase used in this study. *Although the water-in-oil emulsion was stable, these surfactants interact with the NPs in the water phase, leading to their unwanted aggregation inside the droplets.

In this study, the stability of water-in-oil emulsions were tested using various commercially available surfactants in different continuous phases. The different surfactants and different continuous phases studied are listed in Table: 3.1. Only the combinations leading to stable emulsions were then tested to fabricate the clusters. One particular difficulty in this study was that some of the surfactant tested (namely Span 80 and Brij 93) interacted with the nanoparticles contained inside the water droplets, which led to their irreversible aggregation. This has of course to be avoided. This can be identified easily by noting the colour of the emulsion, a pink color emulsion means the NPs within the droplets are stable and a blue color means the NPs have aggregated inside the water droplet. The stability of emulsions was studied using macroscopic observations, microscopy investigations and granulometry measurements. From this first screening, it comes that the surfactant DC 5225c, purchased from DOW CORNING, could very efficiently stabilize the water droplets in both PDMS and dodecane and was thus chosen for the clusters fabrication. Thus, it was used to prepare a 20% by volume water-in-silicone oil emulsion. First, the influence of the

surfactant concentration on the water droplet size is studied using granulometry (shown in Figure 3.2). From these measurements, it comes that the optimal surfactant concentration can be set to 15 wt %. Similar results (not shown) were obtained in dodecane in which the surfactant concentration was fixed at 10 wt%.

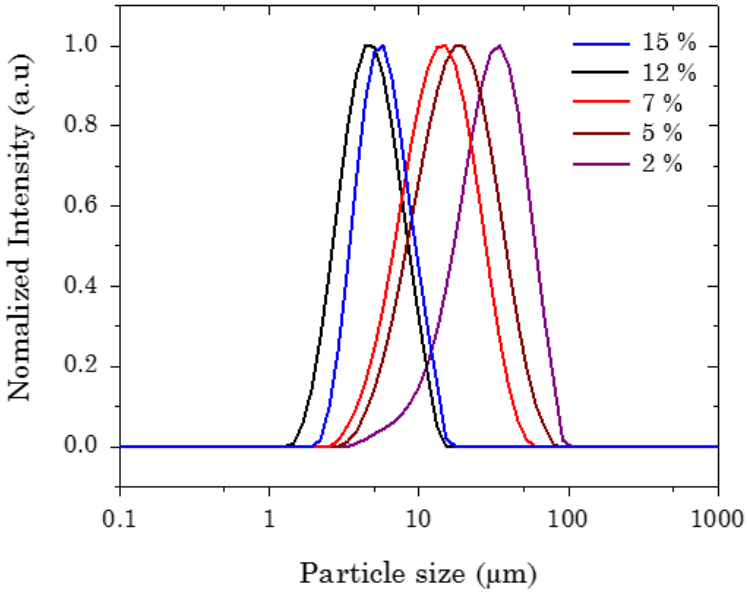

Figure 3.2: Dependence of droplets size distribution on the concentration of surfactant DC 5225c.

At this concentration however, DC 5225c was not completely soluble in silicone oil and, before its use, the DC solutions were centrifuged to get rid of the immiscible part of the surfactant. As a reminder, DC 5225c is a mixture of several compounds and some of them are apparently insoluble in the oil phase. We then used only the supernatant (containing only the miscible part of the surfactant) for the emulsification process. Due to this centrifugation step, the exact concentration of the surfactant in the continuous phase is not precisely known.

Other surfactants were also probed to stabilize water-in-silicone oil emulsions. Three different surfactants labeled KF6017, KF6028, KF6104 were purchased from Shin-Etsu Silicone. These surfactants have been previously used in the literature to produce stable water-in-silicone oil emulsions [2]. Among the three surfactants, except KF6017 the remaining surfactants were completely miscible with silicone oil and therefore did not require an additional centrifugation step. These surfactants, were then used to produce 20 % in volume water-in-silicone oil emulsions and the size of the water droplets were measured using granulometry. All the three sufactants produced a very stable emulsion, but only KF6104 produced a single size distribution of water droplets. All the emulsions were produced with 4 wt% of surfactants in 8 ml of silicone oil. A decrease or increase in the surfactant concentration did not give any significant change in the droplets size distribution. Therefor surfactant KF6104 was found to be more suitable to produce a single size distribution of clusters.

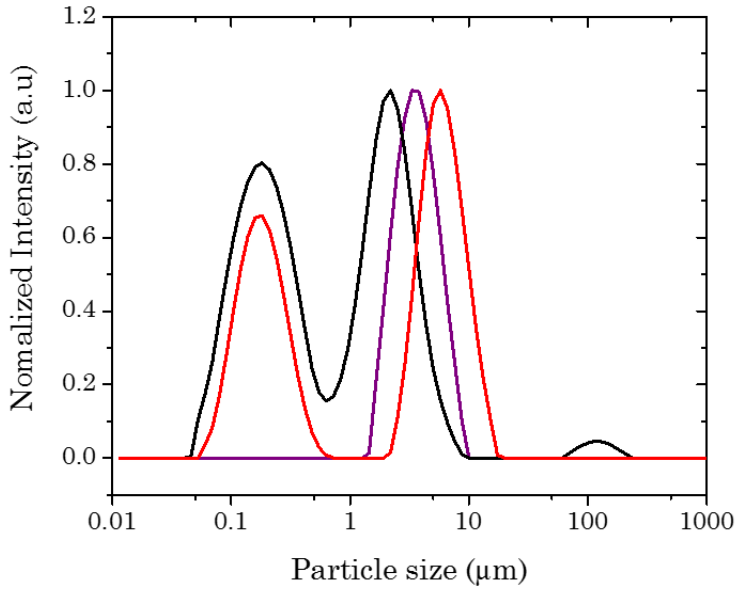

Figure 3.3: Size of water droplets as a function of different surfactants. Red-KF6017, black-KF6028, and violet-KF6104.

Although silicone oil as the continuous phase yielded stable emulsions, we also produced water-in-dodecane emulsions. This is because, once the final clusters are produced in dodecane, it can be exchanged with volatile solvents such as hexane in order to image the clusters using transmission electron microscopy. DC 5225c could also be used to stabilize water-in-dodecane emulsions. Further in the manuscript, we will also use Hypermer as a surfactant since it appeared to be well adapted for the fabrication of water-in-dodecane emulsions using microfluidics.

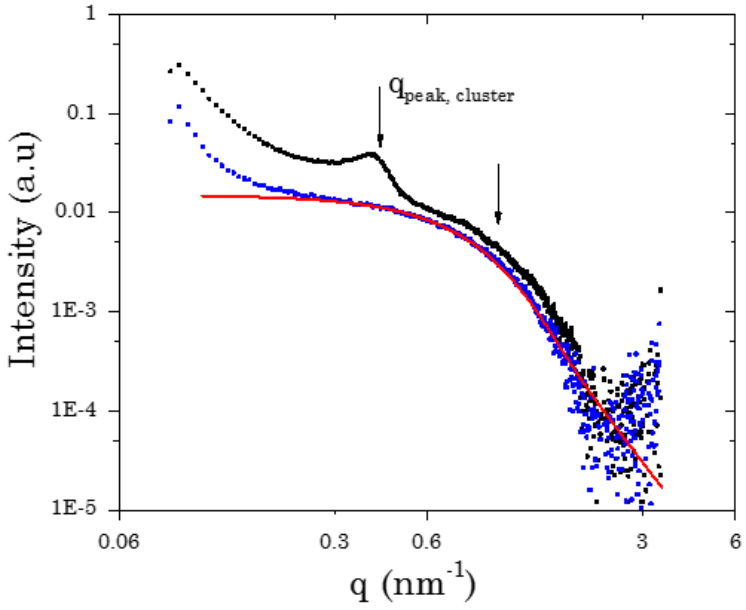

Figure 3.4: SAXS curves of gold clusters (black dots) dispersed in dodecane, hypermer+dodecane solution (blue dots) and theoretical form factor of a sphere with radius 1.3 nm (red line). Obtained using SAXS 2.

Though the Hypermer surfactant produced a stable emulsion, one also observed the appearance of an intense light scattering that we attributed to the presence of micelles in the solvent. Indeed, as time passes, the continuous phase becomes whitish, which we attributed to the swelling of the micelles by the water either coming from the droplets or from the surrounding atmosphere. The presence of these micelles in the final cluster suspension is witnessed using SAXS (Figure: 3.4). From Figure: 3.4 it can be seen that the SAXS curve of a cluster solution has a first peak at about 0.4 nm^{-1} corresponding to the interparticle distance within the cluster and a bump well accounted for by the form factor of spherical objects of radius 1.3 nm. Finally, the presence of these swollen micelles makes it difficult to study the optical properties of the final clusters and, as much as we could, we tried to eliminate this surfactant in our forthcoming system.

Thus, DC 5225c in dodecane and KF6104 in silicone oil were the chosen surfactants+oil solutions to fabricate the clusters in the process used in the forthcoming section.

3.2.2 Ripening process

All the glassware used in this step were first rinsed with aqua regia.

The 20% vol water-in-oil emulsion is transferred to a glass balloon which is then fixed to a rotavapor. The water droplets are ripened at a constant pressure comprised between 2 and 10 mBar and maintained at room temperature. The balloon is also rotated at a constant speed of 240 rpm, to ensure that all the water droplets in the system are ripened at the same time. The rotation of the balloon also keeps the droplets from colliding with each other.

The word “ripening” here describes the evaporation of water from the droplets. The ripening process involves three steps: first, the water from the droplets dissolve into the oil phase. Then, the water molecules diffuse towards the surface of the sample through the continuous phase due to the applied pressure. Finally, they pass from the liquid to the gas phase at the continuous phase/gas interface. The rate of evaporation therefore depends upon several factors: the solubility of water in the oil phase, which itself is a function of temperature, the surface area of contact between the continuous phase and the gas phase and the applied pressure. The solubility of water in the oil phase should be low enough to create a stable emulsion but still high enough to help in the ripening process. The solubility of water is 40 mol/m^3 and 33 mol/m^3 in PDMS and dodecane respectively. The surface area available for the evaporation of water depends upon the size of the glassware used and the rotation speed. In this thesis, a 100 mL round-bottom flask was used to ripen all the systems.

The applied pressure fluctuates between 2 to 10 mbar. Although increasing the temperature will fasten the process, this is avoided for two main reasons: 1) The ripening speed partly determines the final structure of the cluster, going too fast might lead to a

non spherical object [3]. 2) The polymer chains that will be used for the stabilization of gold NPs may exhibit attractive interactions at high temperature, as expected from such LCST systems.

3.3 Fabrication of cluster

3.3.1 First tests

The structure and size of the gold NP clusters largely depend upon the size, the initial concentration, and surface coverage of the NPs in the water phase. The initial NPs suspension in water should of course be stable in order to avoid unwanted aggregation. The stability of the initial dispersion is first checked using different analytical tools such as UV-Vis spectroscopy, DLS and SAXS. These techniques will be also used for the final systems (shown below).

The clusters of gold NPs were first fabricated using the Turkevich solution (gold NPs stabilized with citrate ions in water) as the dispersed phase and silicone oil as the continuous phase. However, the presence of citrate and sodium ions in the water phase complicated the fabrication process. First, the surfactant (Brij, Span 80) used for the stabilization of emulsions interacted with the gold NPs inside the water droplets leading to their unwanted aggregation. Secondly, the presence of ions inside the water droplets create an osmotic pressure, which further prevents the droplets from ripening completely. Thus, the NPs do not come very close to each other to form a final dense cluster.

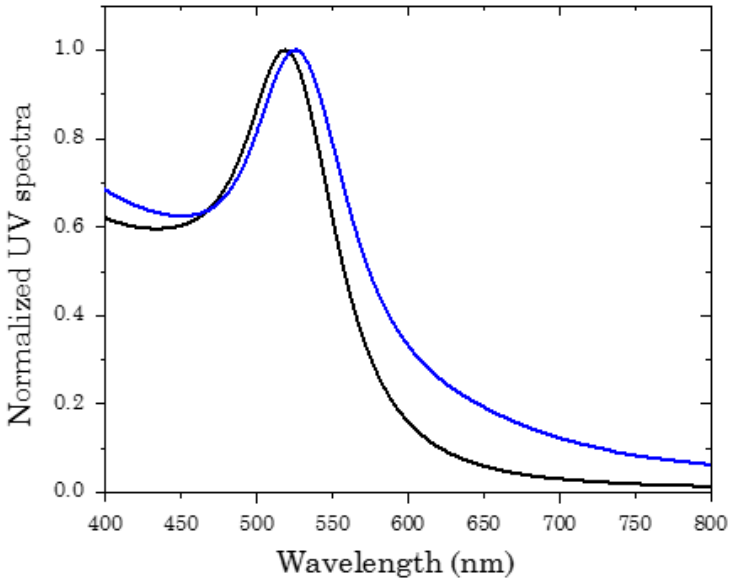

Figure 3.5: UV-Vis spectra of gold NPs stabilized by citrate before (black line) and after ripening (blue line).

This osmotic effect can be deduced from the curves of Figure 3.5, which shows the

evolution of the UV spectra before and after the ripening of water droplets in the solution. As discussed in Section 1.4.1, with the wavelength of the peak λ_{max} one can estimate the distance between the NPs within the cluster. Before ripening, the observed λ_{max} = 519 nm is compatible with the presence of individual NPs. After ripening, the peak slightly shifts to 525 nm.

The red shift in the λ_{max} value is indeed due to the plasmonic coupling between gold NPs inside the cluster. Therefore, this red shift can be used to estimate the edge-to-edge distance between the NPs forming the clusters [4]. In this case, one can deduce a distance of around 17 nm, which corresponds to a NPs volume fraction of around 0.05 in the cluster.

In order to increase the volume fraction of NPs inside the cluster, and also to increase the stability of the NPs in the water phase, the surface of the individual gold NPs were capped with different polymers. The impact of the polymer used as well as its molar mass and surface density was studied using different analytical tools. First, we used poly(vinylpyrolidone) (PVP) at three different molar mass. In a second set of experiments, we used thiol- poly(ethylene glycol) molecules of four different molar mass.

3.3.2 Clusters of Au-PVP NPs

In a first experiment, PVP chains with different molar mass (Mw = 10 kg/mol, 29 kg/mol and 55 kg/mol) were adsorbed on the surface of the gold NPs. The resulting suspensions are labelled as Au-PVP10k, Au-PVP29K and Au-PVP55K respectively. These suspensions were then used as the dispersed phase to create a water-in-oil emulsion.

3.3.2.1 Capping of gold with PVP and ripening of water droplets

The stability of gold NPs in the water phase can be improved by capping the surface of the gold NPs with polyvinylpyrrolidone (PVP) [5]. In such case, the polymer chains physically adsorb at the NPs surface. This will prohibit the surfactants used for the emulsion process from interacting with the NPs and also lead to a repulsive force between the NPs. The surface modification of the NPs surface with PVP is achieved by exchanging the citrate ions adsorbed on the NPs with PVP . In order to completely exchange all of the citrate ions, an excess of PVP (about 5 times the concentration of citrate ions) was added to the NPs solution. The concentration of citrate ions used in the Turkevich method is 0.88 mmol/L (see Section 2.5). Therefore a 0.05 wt% of PVP (in case of 10000 g/mol) in water is used for the ligand exchange process.

The excess of citrate ions present in the Turkevich suspension is first removed by centrifuging the solution at 12000 rpm for 45 min and replacing the supernatant with a solution of PVP molecules in the right concentration suspended in water. This NPs suspension was then stirred at room temperature for 6 hrs. After 6 hrs, the solution is once again cen-

trifuged and the supernatant is replaced with pure water. This step is repeated 2 to 3 times to remove the excess PVP and the remaining citrate ions from the final solution.

The resulting suspensions, addressed as Au-PVP10k, Au-PVP29K and Au-PVP55K, were analyzed using UV-Vis spectroscopy (Figure 3.6).

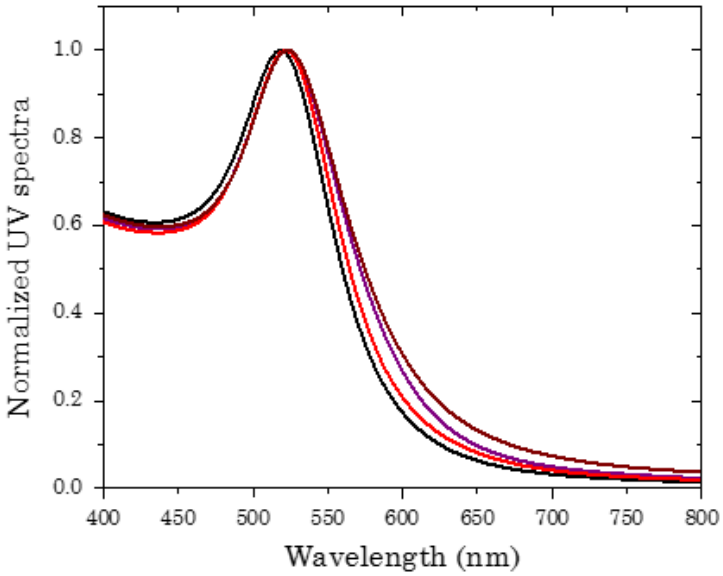

Figure 3.6: UV-Vis spectra of gold NPs stabilized using citrate (black), Au-PVP10k (red), Au-PVP29K (purple) and Au-PVP55K (wine red) dispersed in water.

The UV-spectra of the solutions before ripening is shown in Figure 3.6 and exhibits a small red shift in the resonance wavelength between gold NPs stabilized by citrate (λ_{max} = 519 nm) and PVP (λ_{max} = 523 nm). This shift can be attributed to the change in the refractive index of the immediate surrounding of the NPs. Indeed, in Turkevich suspension, the citrated NPs are surrounded by water molecules, but when the polymer molecules adsorb onto the NPs surface the refractive index changes from water to water-swollen PVP.

The curves obtained for Au-PVP stabilized using different molar mass do not have any prominent shift in the λ_{max} value (see Figure 3.6). However, a small difference is observed at longer wavelengths ($\approx$ 550 nm), this could either be due to the absorption arising from the excess polymer in the solution or due to small NPs aggregates.

These suspensions (Au-PVP10k, Au-PVP29K and Au-PVP55K) were used to create water-in-oil emulsions and ripened to produce clusters. The cluster suspensions are labelled as $C_{Au\text{-}PVP10k}$, $C_{Au\text{-}PVP29k}$ and $C_{Au\text{-}PVP55k}$. The UV spectra of the resulting cluster suspensions are shown in Figure 3.7.

The broadening and red-shift of the UV spectra obtained for the gold cluster ($C_{Au\text{-}PVP10k}$, $C_{Au\text{-}PVP29k}$ and $C_{Au\text{-}PVP55k}$) in comparison to the individual NPs (Au-PVP10k, Au-PVP29K and Au-PVP55K) are due to the electromagnetic couplings between NPs within the cluster. The spectra (Fig 3.7) indicates a clear increase in the value of λ_{max} with decrease in molar mass of PVP. This shows that the edge-to-edge distance between the NPs within

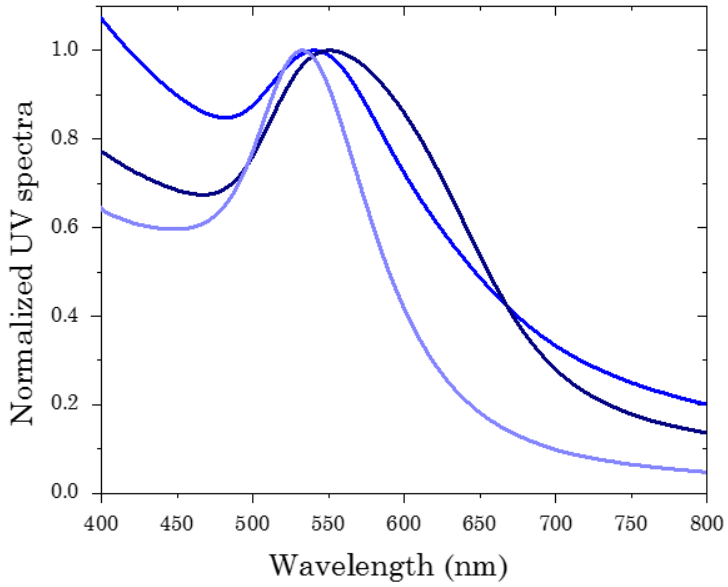

Figure 3.7: UV-Vis spectra of gold NP clusters obtained from Au-PVP10k (dark blue), Au-PVP29K (blue) and Au-PVP55K (light blue).

the cluster increases with the increase in the PVP molar mass. The smallest distance was found for the sample $C_{\text{Au-PVP10k}}$, and is of the order of 3 nm. For samples $C_{\text{Au-PVP29k}}$ and $C_{\text{Au-PVP55k}}$) the edge to edge distance is calculated to be ≈ 4 and 5 nm respectively.

3.3.2.2 Kinetic study of the ripening process

To understand the factors influencing the ripening of the water droplets, the process was studied by sampling aliquots from the rotavapor at regular intervals of time and subjecting them to different analytical tools. For this purpose, water-in-oil emulsions made using Au-PVP10k suspensions as the dispersed phase and silicone oil/DC 5225c solutions as the continuous phase were selected.

The samples were taken at 15 min, 30 min, 45 min, 60 min, and 75 min and the suspension after 75 mins of ripening and two days of stirring in a dry atmosphere at normal pressure. These samples were labelled PVP-R15, PVP-R30, PVP-R45, PVP-R60, PVP-R75 and PVP-R75V2, respectively, and were studied using UV-Visible, IR spectroscopy and small angle X-ray scattering.

ATR-FTIR spectra of the aliquots were obtained to estimate the rate of the ripening process by measuring the volume fraction of the water remaining in the solution as a function of time. This was achieved by measuring the intense band at 1640 and 3480 cm^{-1} which corresponds to the stretching and bending of the O-H bonds of the water molecules. In order to quantitatively estimate the volume fraction of water in the aliquots, a master curve is first created by measuring emulsions with different volume fraction of water in oil phase. The IR spectra obtained for 1, 5 and 10 wt% w/o emulsion are shown in Figure 3.8. The decrease in the intensity of the peaks at 1640 and 3480 cm^{-1} with the

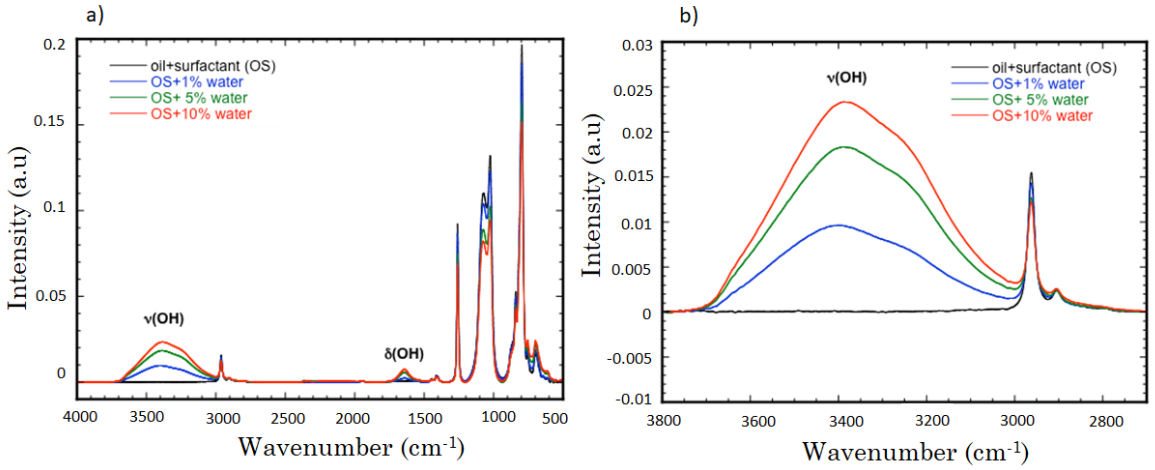

Figure 3.8: ATR-FTIR spectra for different w/o volume fraction. a) Full spectrum b) Zoom of the spectrum in the ν(OH) wavenumber domain.

decrease in water volume fraction is clearly visible. Thus a master curve is produced (Figure 3.9) by measuring the IR spectra for w/o emulsion with volume fraction ranging from 0.5 to 10 wt%. The decrease in water volume fraction gives rise to a linear decrease in the intensity of the peak at 1640 cm^{-1} (refer Figure 3.9).

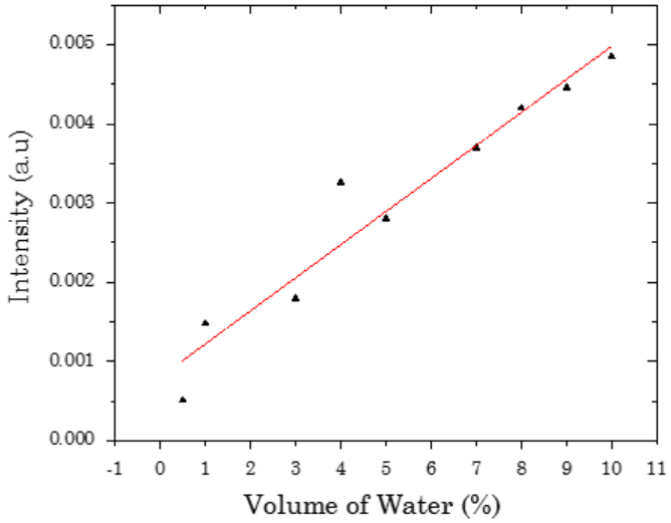

Figure 3.9: Intensity measure at 1640 cm^{-1} (black triangle). Linear fit of the measured intensity (red line).

The IR spectra of the aliquots are show in Figure 3.10 a. An ATR-FTIR spectrum was also taken for sample PVP-R75V2 but did not display the water bands, indicating that water had been fully removed after this level of ripening, at least up to the detection limit of the spectrometer. With the help of the master curve (Fig. 3.9), the water volume fraction remaining in the system as a function of time is quantitatively estimated. The decrease in water volume fraction seems to follow an exponential decay with a function:

$$\phi(t) = \phi(0).\exp(-\frac{t}{\tau}) \tag{3.1}$$

Where ϕ(t) and ϕ(0) are the water volume fraction at time t and time 0, respectively and τ is the characteristic ripening time.

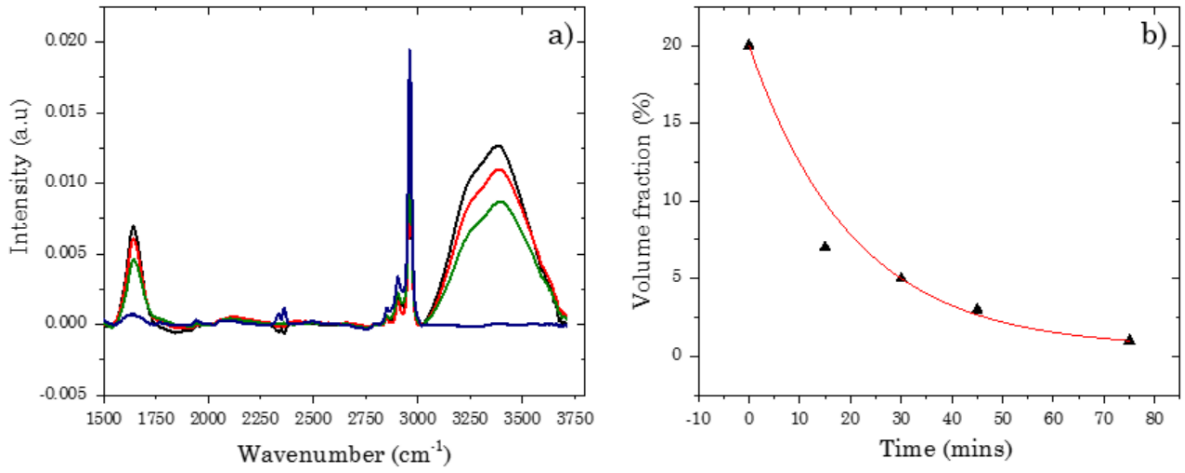

Figure 3.10: a) IR-spectra of samples PVP-R15 (blue), PVP-R30 (green), PVP-R45 (red), and PVP-R75 (black) b) Volume fraction as a function of time (black triangles) with an exponential fit (red line).

The UV-Vis spectra of the aliquots were also obtained to estimate the edge-to-edge distance between the NPs inside the water droplets as a function of ripening time. Figure 3.11 shows the UV-Vis spectra of samples PVP-R60, PVP-R75 and PVP-R75V2 as well as that of the initial gold NPs suspension.

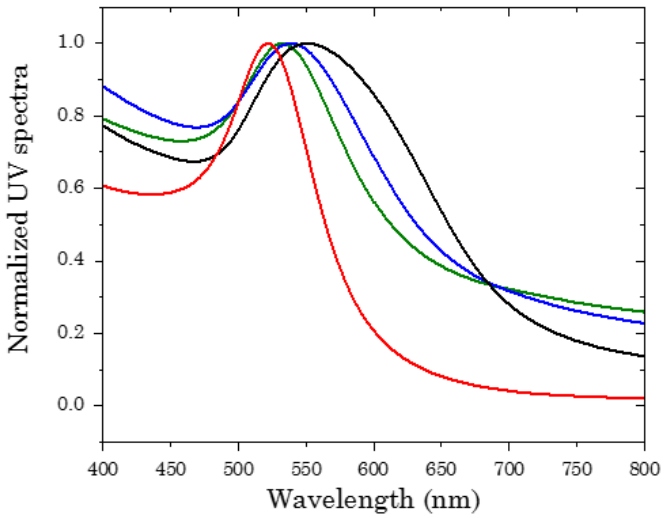

Figure 3.11: UV-Vis spectra Au-PVP10K (red) and samples PVP-R60 (green), PVP-R75 (blue) and PVP-R75V2 (black).

The spectra presents increasing broadening and red-shift of the absorption band as the ripening time is increased. The increasing confinement of the Au NPs within the droplets of reducing size decreases the distance between NPs, resulting in the occurrence of plasmonic couplings and therefore to a red-shift in the LSPR peak. The LSPR band

remains, nevertheless, well-defined, which hints at a good homogeneity of the distance between NPs. This process is accompanied by a color change of the solution from pink to blue. According to Mie theory calculations (see e.g. Fig. 3 in [4]), the broadening and red-shift of the plasmonic extinction band observed for the final sample are compatible with electromagnetic couplings between NPs, with an edge-to-edge distance on the order of 3 nm. The aliquots taken at times before 60 mins could not be analyzed by UV-Vis spectroscopy since they scatter too much light.

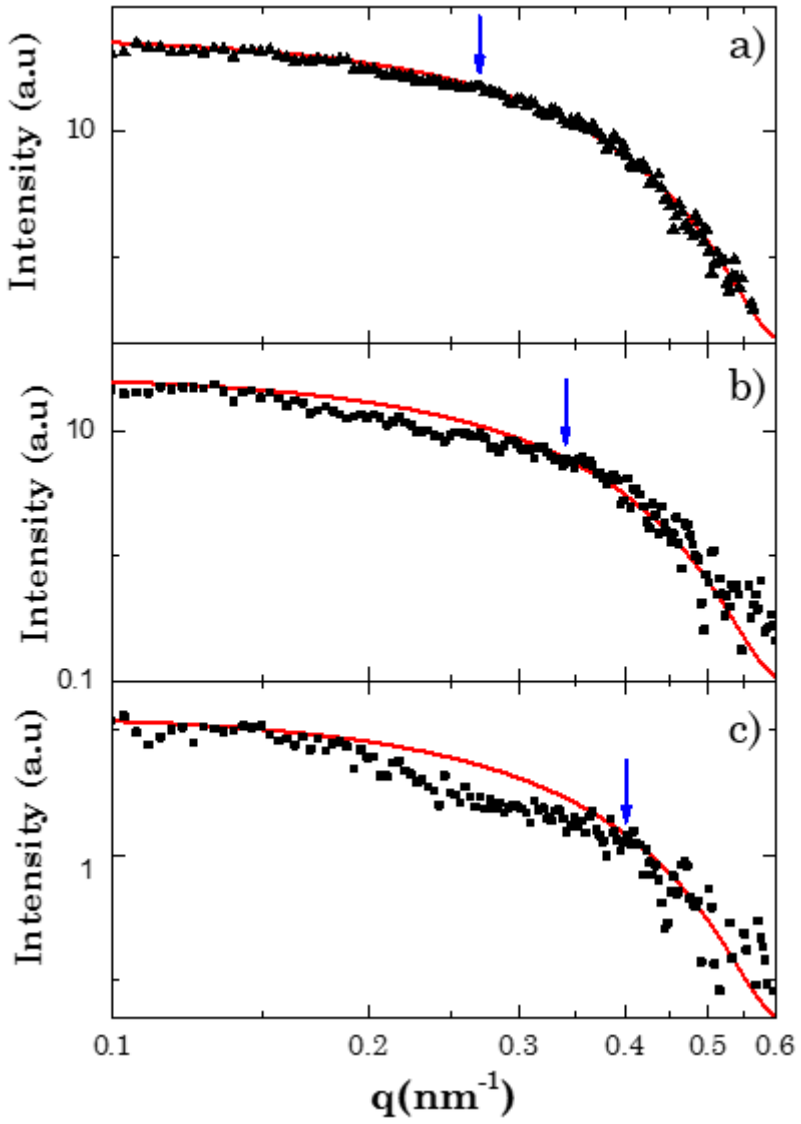

Figure 3.12: SAXS profile for samples (black symbol) a) PVP-R60, b) PVP-R75 and c) PVP-R75V2. The red line denotes the form factor of individual NPs with radius 6.7 nm. The blue arrow indicates the onset of the NPs correlation. Obtained using SAXS 1.

The evolution of the interparticle distance were also studied using small angle X-ray scattering. The SAXS instrument was used to study correlation between the NPs forming the clusters. The SAXS spectra of the aliquots together with the form factor of individual NPs are shown in Figure 3.12. The spectra obtained for aliquots at time 15 min, 30 min and 45 min did not differ much from the form factor of individual NPs, meaning there was

no detectable correlation between the NPs. However, a correlation peak begins to appear from time t = 60 mins at q = 0.27 nm^{-1} and shifts to = 0.3 nm^{-1} at time t = 75 mins. The final correlation peak is obtained for sample PVP-R75V2 at q = 0.37 nm^{-1}. The shift in the correlation curve with time is witnessed from Figure 3.12. The onset of the correlation curve is used to estimate the edge-edge distance between the nanoparticles to be 3.6 nm. This value is in good agreement with the value obtained from UV-Vis spectra.

This dramatic decrease in the interparticle distance is compatible with the evolution of the global size of the objects. Figure 3.13 shows that the size of the initial droplets is decreased by a factor 40 upon ripening, inducing a $\sim 6 \times 10^4$ - fold multiplication of the internal gold volume fraction f. The hydrodynamic size of the final clusters was measured using dynamic light scattering (DLS).

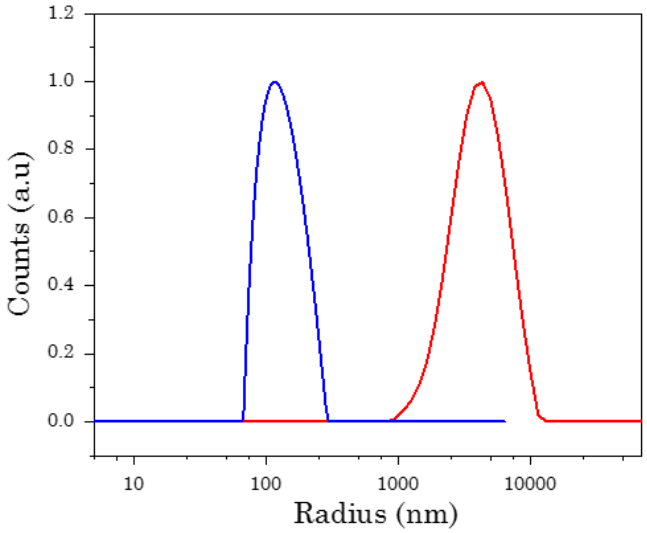

Figure 3.13: Granulometry and DLS measurements, respectively, of the size of the initial emulsion droplets (red curve) and of the clusters in the PVP-R75V2 suspension (black curve).

TEM images of the synthesized clusters were obtained by depositing few drops of the cluster solution (silicone oil) on a TEM grid. The prepared TEM grid was placed under vacuum overnight for drying. The TEM images obtained were very difficult to analyze, since the presence of silicone oil induced scattering when viewed under the electron beam. The clusters were then produced in dodecane (surfactant-DC 5225c) using the same procedure as mentioned above. After ripening, the clusters were washed with hexane by centrifugation cycles and a small portion of the clusters dispersed in hexane were deposited onto a TEM grid. Since hexane evaporates easily, the clusters could be imaged in good conditions using TEM.

The TEM images shown in Figure 3.14 shows the difference in the image resolution when the TEM grids are made using clusters dispersed in silicone oil and hexane. In silicone oil (pictures a-c), the presence of remaining oil on the sample cannot be eliminated using vacuum. Consequently, it is not possible to obtain good focused images of the samples. Nevertheless, we observe spherical objects having the expected average size but

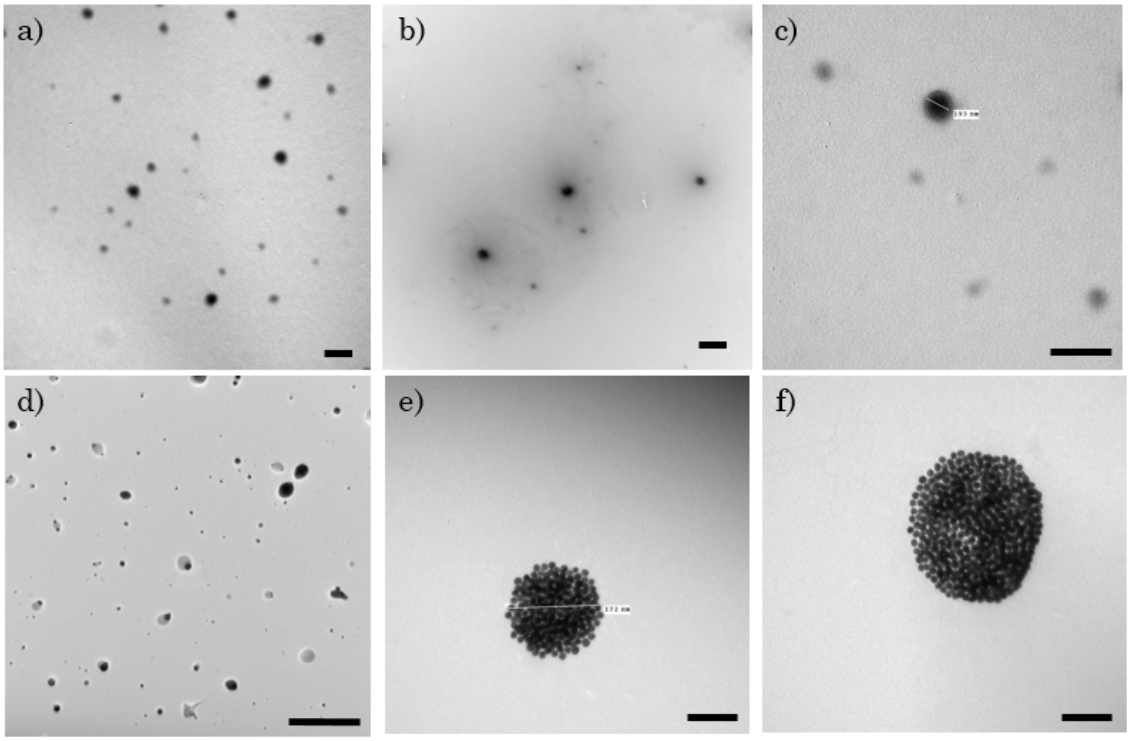

Figure 3.14: Transmission microscopy images of Au-PVP10K NP clusters dispersed in a), b) and c) silicone oil (scale bar 500 nm) and in hexane d) scale bar 10 µm e) and f) scale bar 100 nm.

their internal structure cannot be depicted. When dodecane is used and replaced by hexane, we get much cleaner samples for TEM (pictures d-f) and the internal structure can be resolved. Clearly, the images exhibit rather homogeneous and spherical objects, which seems to indicate that the clusters are not too affected by the centrifugation process and the capillary forces that act on them during drying. However, TEM images may not be considered as a statistical representation of the cluster's suspension.

3.3.3 Clusters of Au-PEG NPs

The gold NPs initially obtained with the Turkevich method were also capped with methoxy poly(ethylene glycol) thiols (PEG-SH). The resulting suspensions are labeled as Au-PEG. The difference between Au-PVP and Au-PEG is that, while PVP chains are physically adsorbed at the surface of the NPs, the PEG chains are covalently bonded to the NPs surface through the thiol group (SH). This creates a polymer brush which extends into the solution when suspended in water. A schematic of the expected structure of the layers in each case is shown on Figure 3.15 b.

3.3.3.1 Peglation of gold nanopartricles

To cap the gold NPs with PEG, four different PEG-SH of molar mass M_w = 800 g/mol, 2000 g/mol, 5000 g/mol and 6000 g/mol were grafted on the gold NPs. The grafting process involved adding a quantity α (mol) of PEG-SH to the aqueous suspension of citrate-coated

gold NPs, so that $\frac{\alpha N_A}{4\pi n_P (d_{NP}/2)^2}$ is the nominal grafting density at the gold surface, with N_A the Avogadro number, n_P the number of NPs in the suspension and d_{NP} the mean diameter of the gold NPs. Several suspensions were produced with the different PEG-SH ligands and different nominal densities ranging between 0.5 and 4 ligand molecules/nm^2. The resulting suspensions are labeled Au-SH-PEGα-X, where X is the number of molecules/nm^2.

Hydrodynamic radius (R_H) of gold NPs capped with different molar mass of PEG and different grafting density were measured using dynamic light scattering. All the measurements were carried out with gold NPs suspended in water with a volume fraction $6x10^{-4}$. Figure 3.15 a) represents the hydrodynamic radius distributions of gold NPs stabilized with citrate, PVP (Mw = 10^4 g/mol), and PEG (Mw = 5000 g/mol). As expected, the R_H of Au-citrate is slightly smaller than the one of Au-PVP and much smaller than the one of Au-PEG, since this length includes both the NP and the polymer layer. The increase R_H in case of Au-PEG when compared to Au-PVP is due to the fact that, in the case of PEG, the polymer molecules extend into the solution to form a brush whereas PVP is randomly adsorbed on the NPs surface (see Fig: 3.15 b). Figure 3.15 a. also shows a small increase in the R_H when the density of PEG polymer grafted onto the NPs surface is increased.

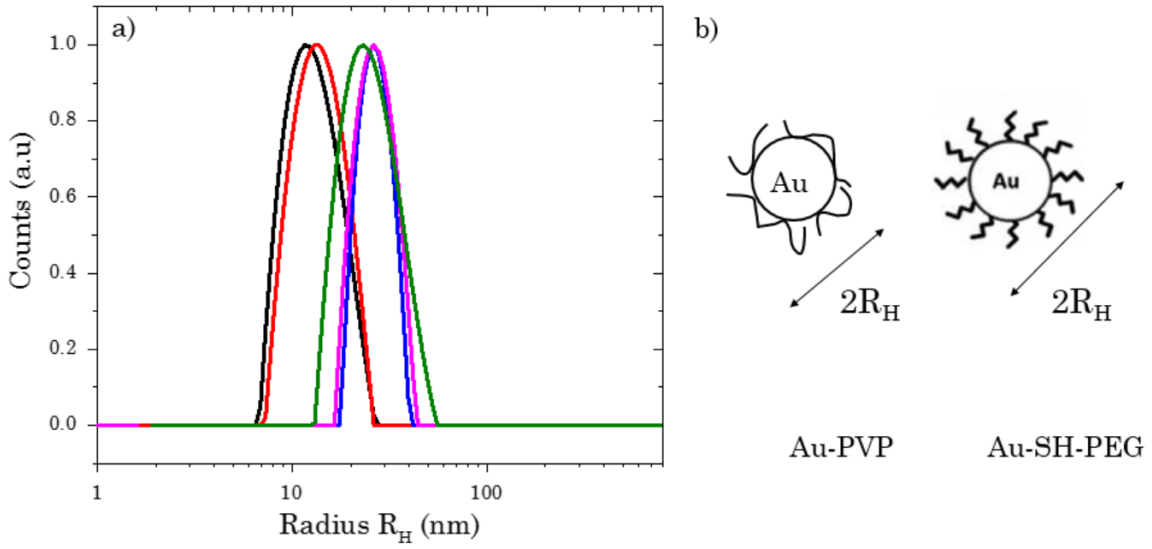

Figure 3.15: a) Hydrodynamic radius of Au-citrate (black), Au-PVP10K (red), Au-SH-PEG5000-2 (green), Au-SH-PEG5000-4 (pink) and Au-SH-PEG5000-7 (blue). b) Schematic illustration of PVP and PEG molecules grafted on the NPs surface.

DLS measurements were also performed to study the influence of the molar mass of PEG used for grafting the NPs surface on R_H. From Figure 3.16, one observes a quasi linear increase of R_H as a function of the molar mass, as expected for such a "brush" geometry [6].

The UV-Vis spectra of the gold NPs stabilized with different molar mass PEG are shown in Figure 3.17. A small shift in the λ_{max} from Au-citrate to Au-PEG is due to the change in the refractive index of the immediate surrounding of the NPs. No prominent difference in the UV spectra is observed for NPs stabilized with different PEG molar mass. This denotes

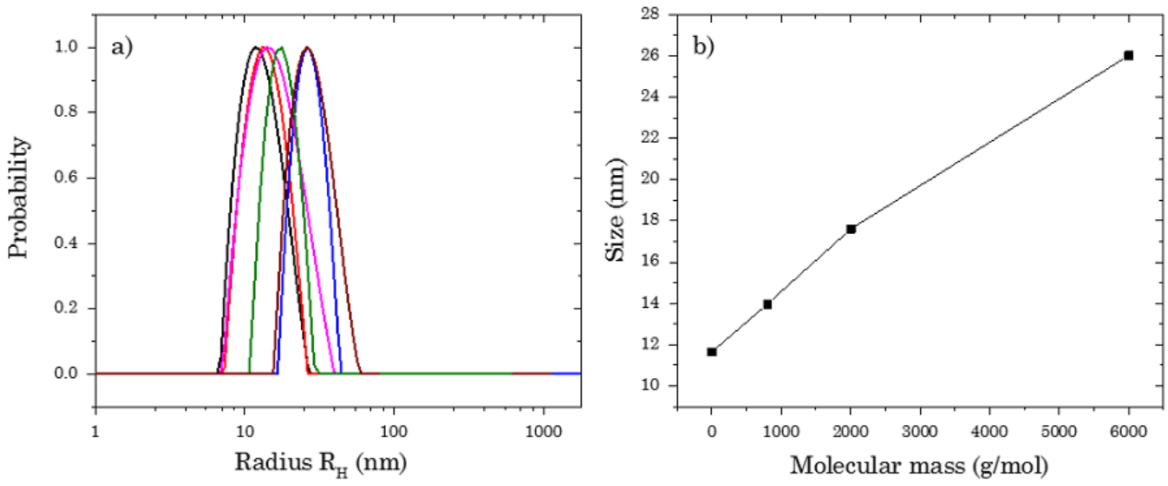

Figure 3.16: a) Hydrodynamic radius of Au-citrate (black), Au-PVP10K (red), Au-SH-PEG800-4 (pink), Au-SH-PEG2000-4 (green), Au-PEG5000-4 (blue) and Au-SH-PEG6000-4 (brown). b) Hydrodynamic radius of gold NPs as a function of polymer molecular weight (black).

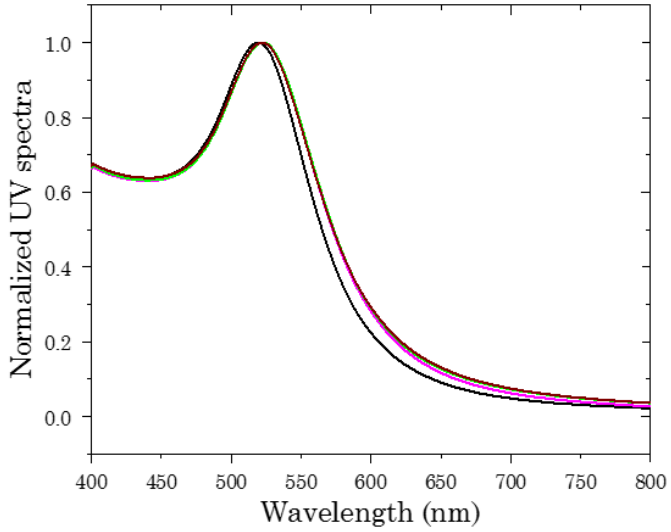

Figure 3.17: UV spectra of gold nanoparticles stabilized with citrate (black), PEG800-4 (pink), PEG2000-4 (green) and PEG6000-4 (brown).

that the NPs capped with PEG with different molar mass and nominal densities are all stable in water without any aggregations.

The size of the PEG stabilized gold NPs were also probed using transmission electron microscopy (Figure 3.18) and small angle x-ray scattering (Figure 3.19). Due to the difference in contrast between gold and PEG, TEM images of the gold NPs stabilized with PEG (shown in Figure 3.18) only show the gold core and not the polymer layer and thus the images obtained for different Au-PEG suspensions were very similar. The SAXS curves of three different Au-PEG suspensions obtained from the same batch of Turkevich solution are shown in Figure 3.19. As expected from the UV spectra, all the gold NPs (Au- PEG) suspended in the water phase are rather monodisperse and fully dispersed in the suspension and exhibit a radius of 6.6 nm and a standard deviation (σ) σ = 0.6 nm.

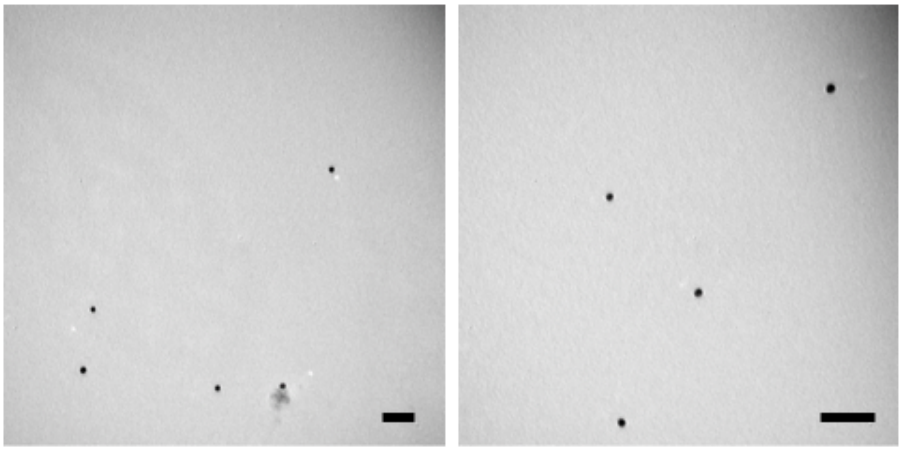

Figure 3.18: TEM images of Au-PEG2000-4 (left) and Au-PEG800-4 (right). The scale bar is 100 nm.

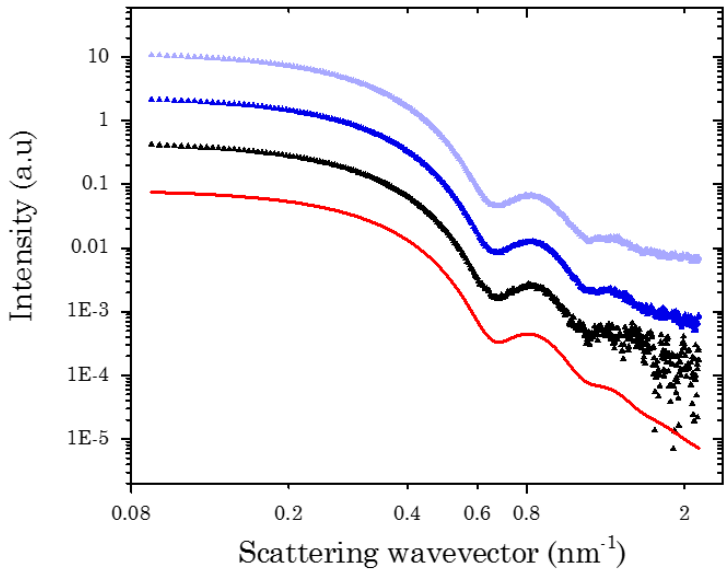

Figure 3.19: SAXS signal of the Au-PEG6000-4 (light blue), Au-PEG2000-4 (dark blue) and Au-PEG800-4 (black). The red line is the theoretical form factor of polydisperse homogeneous spheres (refer Equation 2.23 and 2.24) adjusted to the NPs signal. The curves are vertically shifted for clarity. These SAXS signals were acquired using SAXS 2.

3.3.3.2 Study of the clusters density

The different Au-PEG suspensions were used to fabricate clusters of gold NPs using the rotavapor in the same pressure and temperature conditions as given before. All emulsions were made using dodecane as the continuous phase and DC 5225c as the surfactant.

The resulting clusters were then analysed using UV-Vis spectroscopy and SAXS. Figure 3.20 a and 3.20 b. depict the normalized UV spectra as a function of grafting density and molar mass of the polymer ligands. These spectra clearly indicate that the decrease in the polymer length or the density of the polymer molecules causes a red shift in the resonance wavelength. This red shift is due to the decrease in the interparticle distance between the NPs within the cluster, meaning the volume fraction of gold NPs within the cluster

increases. When the surface density is decreased to a minimal value, the resulting clusters have a shoulder peak in their UV spectra (Figure 3.20 a. black curve - Au-PEG2000-0.5 NP clusters and brown curve - Au-PEG800-1 NP clusters). This type of shoulder peaks has been used to demonstrate the presence of a magnetic dipolar (MD) resonance in addition to an electric dipolar resonance (ED), for instance in [7]. This will further be elaborated in Chapter 4.

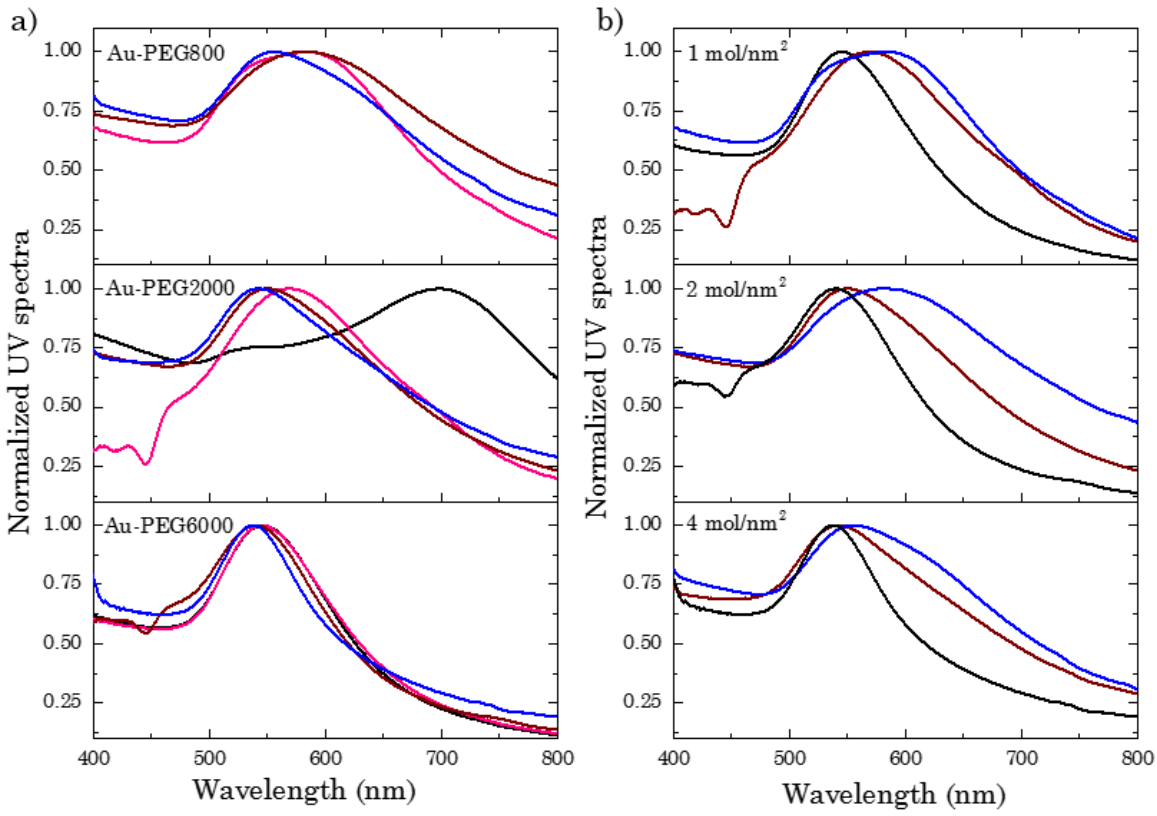

Figure 3.20: Normalized UV spectra of a) Au-PEG800, Au-PEG2000 and Au-PEG6000 NP clusters suspension. The density of polymer molecules used is shown using colour code, 0.5 mol/nm^2 (black), 1 mol/nm^2 (pink), 2 mol/nm^2 (brown) and 4 mol/nm^2 (blue). b) Normalized UV spectra for 1 mol/nm^2, 2 mol/nm^2 and 4 mol/nm^2. The polymer length is shown using colour code, PEG-6000 NP clusters (black), PEG-2000 NP clusters (brown) and PEG-800 NP clusters (blue).

This clearly indicates that the ligand molecules not only help stabilizing the NPs in water and avoid interparticle attraction, which would lead to uncontrolled aggregation, but it is also provides a lever for controlling the final cluster structure. This is also confirmed by the SAXS analysis. Figure 3.21 displays the SAXS signals of three samples with different ligand length: the Au-PEG6000-2 cluster suspension (light blue), the Au-PEG2000-2 cluster suspension (dark blue) and the Au-PEG800-2 cluster suspension (black). They display a clear evolution of the interparticle correlation peak position depending on the length of the NPs ligand, for the same nominal surface density (2 molecules/nm^2): the positions q_1, q_2 and q_3 lead to edge-to-edge distances d_{e-e} of 1.9 nm, 4 nm and 6.9 nm, respectively for the Au-PEG800-2, Au-PEG2000-2 and Au-PEG6000-2 NP cluster systems.

Figure 3.22 displays the SAXS signal of three samples with same ligand length but dif-

ferent nominal densities at the gold surface: the Au-PEG2000-2 cluster suspension (light blue), the Au-PEG2000-1 cluster suspension (dark blue) and the Au-PEG2000-0.5 cluster suspension (black). Again, we see a clear evolution of the interparticle correlation peak position with positions q_1, q_2 and q_3 leading to edge-to-edge distances d_{e-e} of 4.4 nm, 2.7 nm and 1 nm, respectively for the Au-PEG2000-2, Au-PEG2000-1 and Au-PEG2000-0.5 NP cluster systems. These values show that the gold NPs get closer to each other within the clusters when the ligand molecules are shorter or less densely grafted at the gold surface: the choice of the NPs ligand, which defines the thickness of the organic spacer between adjacent nanoparticles, controls the final gold volume fraction within the clusters.

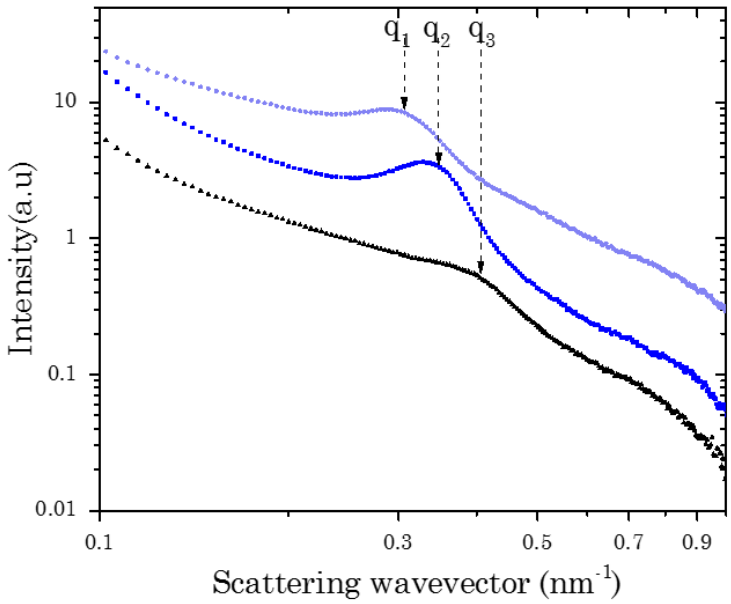

Figure 3.21: Study by SAXS of the internal structure after complete ripening as a function of the length of the polymer ligand grafted onto the NP surface. The curves are vertically shifted for clarity. Interparticle correlation peaks are at positions $q_1 = 0.31$ nm^{-1} (Au-PEG6000-2 NP clusters, light blue), $q_2 = 0.36$ nm^{-1} (Au-PEG2000-2 NP clusters, dark blue) and $q_3 = 0.41$ nm^{-1} Au-PEG800-2 NP clusters, black).

The experimental volume fraction of the clusters can then be estimated using the SAXS data. Assuming a homogeneous packing over the whole cluster volume, the obtained center-to-center distances $d_{c-c} = 2\pi/q^*$ can be related to the gold volume fractions f within the clusters, which can be estimated as close to:

$$f = p\Psi, \text{ with } \Psi = \left(\frac{2r_s}{d_{c-c}}\right)^3, \tag{3.2}$$

where p is the packing density of a close-packed sphere assembly and can typically range between 0.64 for moderately polydisperse spheres [8] and 0.74 for monodisperse spheres, and Ψ is the fraction of gold in the volume of the equivalent packed spheres (gold + ligand shell).

A summary of the SAXS results obtained for different Au-PEG NP clusters is shown in

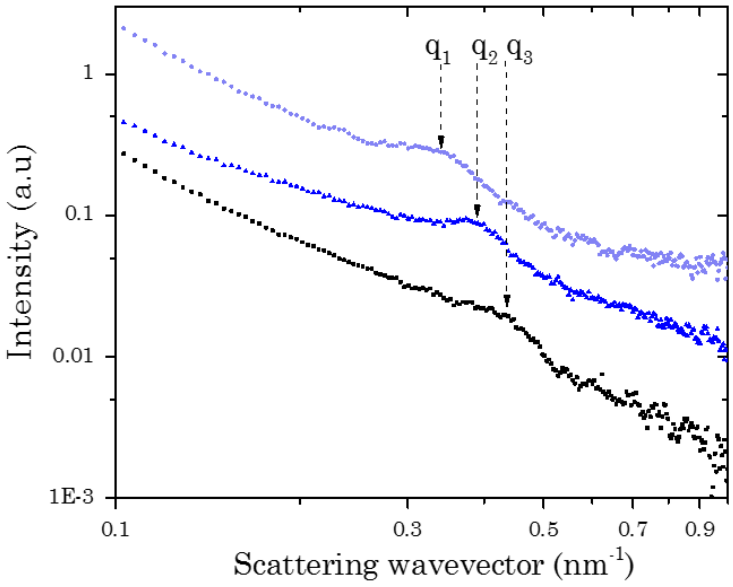

Figure 3.22: Study by SAXS of the internal structure after complete ripening as a function of the surface density of the organic ligand grafted onto the NP surface. The curves are vertically shifted for clarity. Interparticle correlation peaks are at positions $q_1 = 0.35$ nm^{-1} (Au-PEG2000-2 NP clusters, light blue), $q_2 = 0.40$ nm^{-1} (Au-PEG2000-1 NP clusters, dark blue) and $q_3 = 0.44$ nm^{-1} (Au-PEG2000-0.5 NP clusters, black).

Table 3.2. The Table 3.2 gives the values of f obtained from the X-ray study, if we take $p = 0.64$ for all studied samples. The values of the gold volume fraction f, as given by Equation (3.2) with d_{c-c} extracted from the SAXS measurements, range from $f = 0.19$ for sample Au-PEG6000-2 to $f = 0.50$ for sample Au-PEG2000-0.5. Obviously, the cluster density decreases from the top left corner (small ligand quantity) to the lower right corner (large ligand quantity) of the Table 3.2.

In an effort to maximize the cluster density, we have also formulated the samples Au-PEG800-1 NP clusters and Au-PEG2000-0.5 NP clusters, in the upper left corner of the Table 3.2, but these samples showed no peak or a non-reproducible peak in the SAXS study, which indicated that the ligand quantity surrounding the NPs in the initial emulsions is too low to insure their colloidal stability and thus the regular building up of the clusters. These samples were therefore discarded.

	PEG800	**PEG2000**	**PEG6000**
0.5 mol/nm^2	-	0.53	0.24
1 mol/nm^2	-	0.40	-
2 mol/nm^2	0.43	0.27	0.19
4 mol/nm^2	0.46	-	-
8 mol/nm^2	-	-	-

Table 3.2: Experimental values of the gold volume fraction f in the clusters as a function of the length and nominal surface density of the PEG-ligands grafted on the gold NPs, when taking the value 0.64 for the packing factor p in Equation 3.2.

The kinetics of ripening of the clusters were also studied by taking aliquots at regular time intervals. Aliquots extracted during the ripening of the system Au-PEG2000-1 emulsion were also studied by SAXS, and Figure 3.23 displays the SAXS signal of the emulsion at 3hrs 40min, 3hrs 45min and 3hrs 50min (from bottom to top). During most of the ripening process as well as for the 3hrs 40min aliquot, the SAXS signal is dominated by the scattering of the individual NPs. In the 3hrs 40min SAXS signal, an increase in the scattered intensity at the smallest wavevectors can be attributed to the onset of some large-scale correlations between NPs. Clear deviation from the NPs form factor appears for the later ripening times. Peaks are visible at $q_1 = 0.40$ nm^{-1} and $q_2 = 0.41$ nm^{-1}, for 3hrs 45min and 3hrs 50min, respectively, which we interpret as due to a spatial correlation between the NPs inside the droplets.

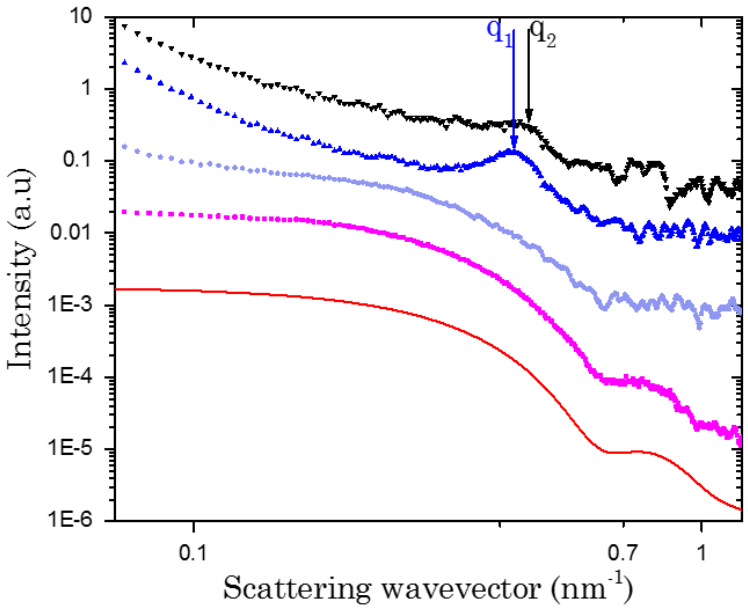

Figure 3.23: SAXS signal of the initial suspension of Au-PEG2000-1 in water (pink dots), and of the Au-PEG2000-1 emulsion after 3hrs40min (light blue), 3hrs45min (dark blue) and 3hrs50min (black). The peaks are at positions $q_1 = 0.40$ nm^{-1} and $q_2 = 0.41$ nm^{-1}, respectively. The red line is the theoretical form factor of polydisperse homogeneous spheres (Equations (2.23) and (2.24)) adjusted to the NPs signal. The curves are vertically shifted for clarity.

Surprisingly, the correlation appears quite suddenly and evolves only slightly between 3hrs 45min and the end of the ripening. The absence of such correlation at earlier stages of the ripening demonstrates that there is no uncontrolled aggregation of the NPs until the confinement of the droplet walls forces it. The characteristic time for the NPs to explore the droplet volume due to Brownian motion is $\tau_s \approx d^2_{\text{droplets}}/d_{\text{NP}}$, where $d_{\text{droplets}} =$ 8 µm is the mean initial droplet size and $d_{\text{NP}} = k_{\text{B}}\text{T}/(6\pi\eta_w r_h)$ is the diffusion coefficient of the NPs of hydrodynamic radius r_h in water of viscosity η_w. d_{NP} was measured by dynamic light scattering to be 0.2 x 10^{-11} m^{2}s^{-1}, which leads to $\tau_s \approx 10$ s, several orders of magnitude smaller than the ripening duration $\tau_r \approx 4$ h, meaning that the NPs can retain their Brownian dynamics essentially unaffected by the droplet walls motion until the last

stages of the ripening.

The observed interparticle correlation at the latest time corresponds to a center-to-center distance of $d_{c-c} = 2\pi/q_2 = 15.3$ nm, i.e. an edge-to-edge distance of $d_{e-e} = d_{c-c} - 2r_s = 1.9$ nm, which is a reasonable value for the thickness of the organic shell produced by the NP ligands. Indeed, $d_{c-c}/2$ can be equated to the radius of the NPs decorated by the dry organic ligand shell, while r_s is the radius of the bare gold spheres.

The homogeneous distribution of NPs within the cluster volume is also witnessed using Cryo-TEM images, provided by E. Nativ-Roth and O. Regev (Ben Gurion University, Israel). Figure 3.24 shows the cryo-TEM images obtained for sample Au-PEG2000-1 NP clusters. The images show that the objects are dense and globular clusters of NPs, with a submicron size. Their internal structure cannot be fully resolved by TEM due to the large NP density, but it appears very regular, and images of the same object at different tilt angles show no evidence of large voids within the object. Cryo-TEM images were also obtained for clusters of Au-PEG6000-2 NPs. However the images could not be understood very clearly. Since the Cryo-TEM images analysis were only carried out once, their repeatability was not checked.

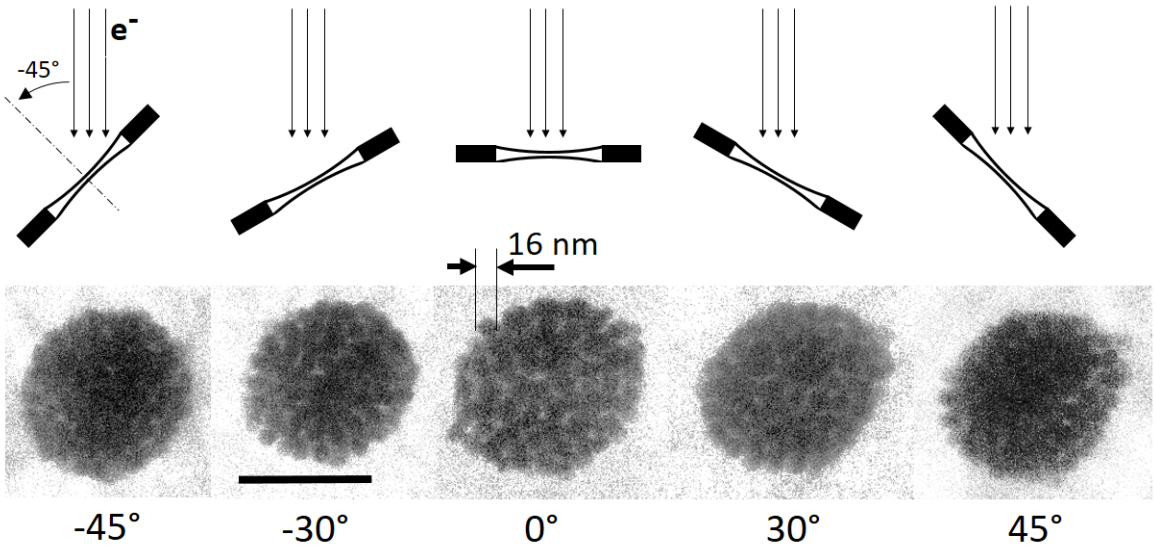

Figure 3.24: Schematic representation (upper part) of how the sample is tilted for observation. Cryo-TEM images (lower part) of Au-PEG2000-1 NP clusters under different observation angles. The scale bar is 100 nm.

In summary, so far we have presented a bulk emulsion based formulation route to fabricate clusters of gold NPs with a polydispersity in size. Control over the final structure of the clusters is attained by varying the molar mass and surface density of the polymer used to stabilise the individual gold NPs, this is demonstrated using SAXS. In the next part, we focus on producing a monodisperse suspension of clusters by employing a droplet based microfluidic technique.

3.4 Introduction to microfluidics

The bulk emulsion based formulation route employed above resulted in a polydisperse suspension of gold NP clusters. Although these clusters showed very promising results in the optical analysis (refer chapter 4), comparing these results to simulations is difficult due to the polydispersity in the cluster size. Therefore in this part of the chapter we detail a droplet based microfluidic technology which can potentially be used to produce a monodisperse water-in-oil emulsions and thus monodisperse clusters.

3.4.1 Droplet-based microfluidic technology

Droplet-based microfluidics involves the generation and manipulation of discrete droplets within an immiscible fluid carrier inside micro-channels. This method has been used to produce highly monodisperse droplets in the nanometer to micrometer size range, at rates of up to twenty thousand per second [9, 10]. More specifically, droplet-based two-phase flow microfluidic devices can be used to control the formation (and/or the merging) of droplets at the nanoliter scale. This feature is ideally suited in the field of chemistry and biology as the reaction time and chemical concentration in each droplet can be precisely controlled [11].

In this project, the key feature of this technology is its ability to produce emulsions with droplets of narrow size distribution [12]. The size of the droplets can also be varied by changing the droplet production parameters such as flow rate and viscosity of the fluids. The droplets are typically generated by a surface induced instability using different device geometries depending on the required droplet fabrication frequency, droplet monodispersity, or variability in droplet size. Similar to bulk emulsions, surfactants are introduced along with the continuous phase to improve the monodispersity of the generated droplets and to guarantee and prevent unwanted coalescence [13].

3.4.2 Chip geometry and material

Microdroplets can typically be generated by using three different microfluidic geometries, namely, the co-flow, T-junction and flow-focusing junction (shown in figure 3.25). In a co-flow chip geometry, the dispersed phase flows into the inner channel, and the continuous phase flows in the outer channel in the same direction [14]. The dispersed phase forms a thin stream that may break into drops away from the orifice (figure 3.25 a).

In the case of a T-junction geometry (figure 3.25 b), the breakup of a continuous stream of one fluid is caused by shear from the cross flow of a stream of a second immiscible fluid [13]. In this geometry the droplet generation is quite robust with respect to identifying appropriate operational parameters.

The flow-focusing geometry is similar to the co-flow geometry but in addition, the two

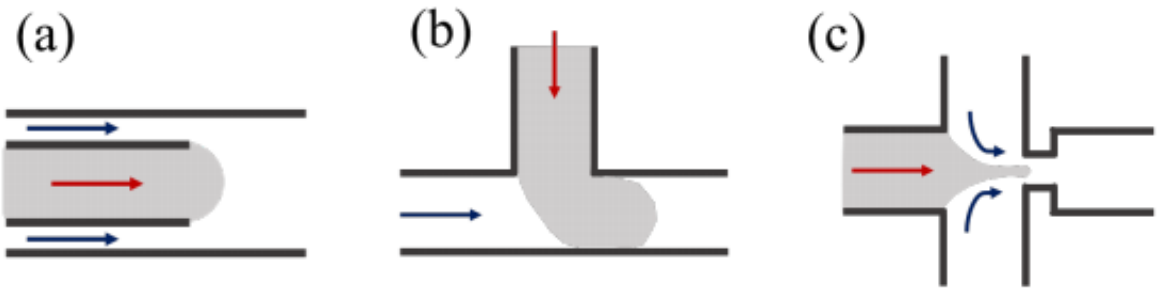

Figure 3.25: Schematic representation of junction geometries for droplet formation: (a) Co-flow, (b) T-junction and (c) Flow-focusing. The arrows indicate the direction of the continuous (blue) and dispersed (red) flow.

co-flowing immiscible liquids are focused through a small orifice or nozzle where they undergo a large elongational flow and thus generate smaller droplets (figure 3.25 c). This geometry provides a larger flexibility in terms of droplets size by adjusting the operational parameters such as viscosity or the flow rates of the fluids etc.

Apart from the geometry of the microfluidic chips, the surface wetting properties of the microfluidic channels should also be adjusted to the type of targeted emulsion (w/o or o/w). For instance, hydrophobic channel walls are required to generate water droplets in an oil phase. And vice versa, hydrophilic channel wall is necessary to generate oil droplets into a water phase. The wetting properties of the channels can be adjusted by coating the channels with either a hydrophobic/ hydrophilic molecules [15].

In this thesis, glass microfluidic chips with a flow-focusing geometry were purchased from Micronit Microfluidics. Glass chips were chosen over PDMS chips since the oil phase (Silicone oil) used in this project tends to swell the PDMS chips [16].

3.4.3 Droplet formation

Regardless of the channel geometry used, several modes of droplet breakup have been observed in shear-based droplet generation, the most common ones are: squeezing [17], dripping and jetting [18]. The three different modes are represented in Figure 3.26.

Among them, the mode 1 (Figure 3.26 a. leads to the formation of droplets which are typically bigger than the nozzle and with a narrow size distribution. As for the mode 2 (Figure 3.26 b), it produces droplets which are a little smaller than the nozzle and with a larger size distribution . However, this mode 2 may lead to the formation of satellite droplets (undesired smaller droplets formed along with the main ones). Finally, the jetting regime (Figure 3.26 c) is characterised by droplets which are much smaller than the nozzle, having a larger size distribution [19, 20].

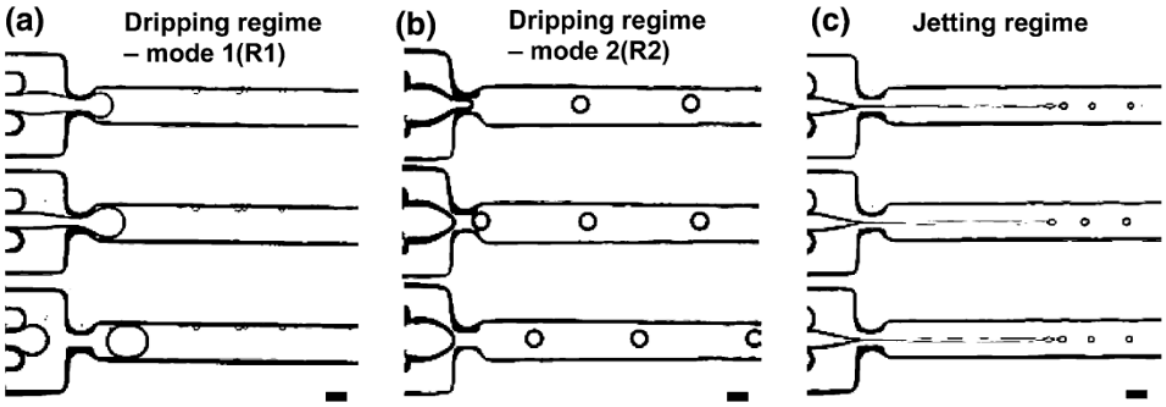

Figure 3.26: Illustration of the different breaking regimes [19].

3.5 Experimental work

In this thesis water-in-oil emulsions were produced using suspensions of gold NPs in water as the disperse phases and different continuous phases were tested to study their ability to stabilize the water droplets.

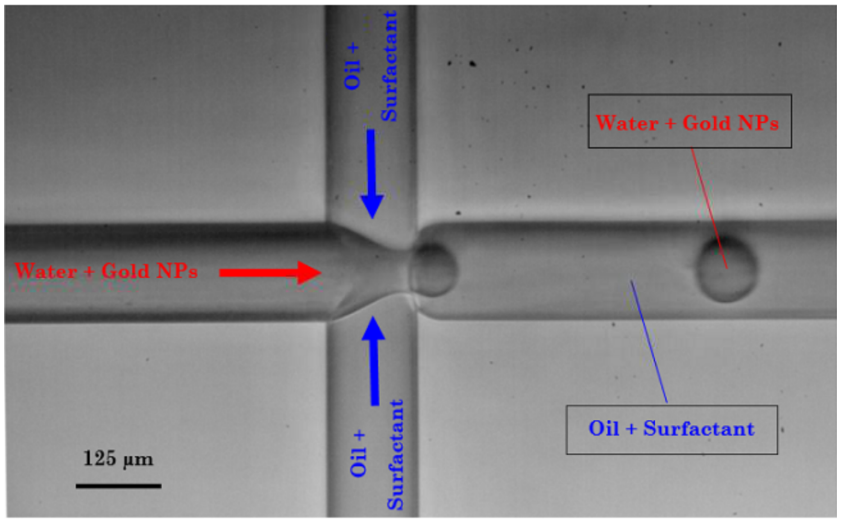

Figure 3.27: Optical microscopy image of the microfluidic chip used as well the droplet production.

Here we will elaborate on three different oil phases (i.e. a surfactant mixed in an oil), namely Hypermer 2296 mixed with dodecane and KF6017 mixed with silicone oil with two kinematic viscosities: 10 and 5 centi-Stokes (cSt). The KF6017 solutions were centrifugated for 10 min at 10,000 rpm to remove the immiscible parts.

The microfluidic chips (DGFF.75.2, Micronit microtechnologies) were purveyed by glass syringes put up on micropumps (NEM-B101-02 B, neMesys UserInterface). The flow rates were fixed at 90 and 10 µL/min for the oil phase and the water phase respectively.

Pictures of the droplets were taken during their formation at regular intervals (100 pics per sec each 10-20 min) with a camera Phantom v411® (16GB Monochrome, software:

PCC 2.14) linked to an optical microscope. From these images, with the software ImageJ, the diameter of the droplets was measured using a macro.

3.5.1 Dodecane-Hypermer

Hypermer mixed with dodecane as the continuous phase was used to produce a stable water-in-oil emulsion using the microfluidic chip. The influence of hypermer concentration in the continuous phase on the droplet size and its polydispersity were first studied. Figure 3.28 shows the evolution of the mean diameter of water droplets as a function of hypermer concentration.

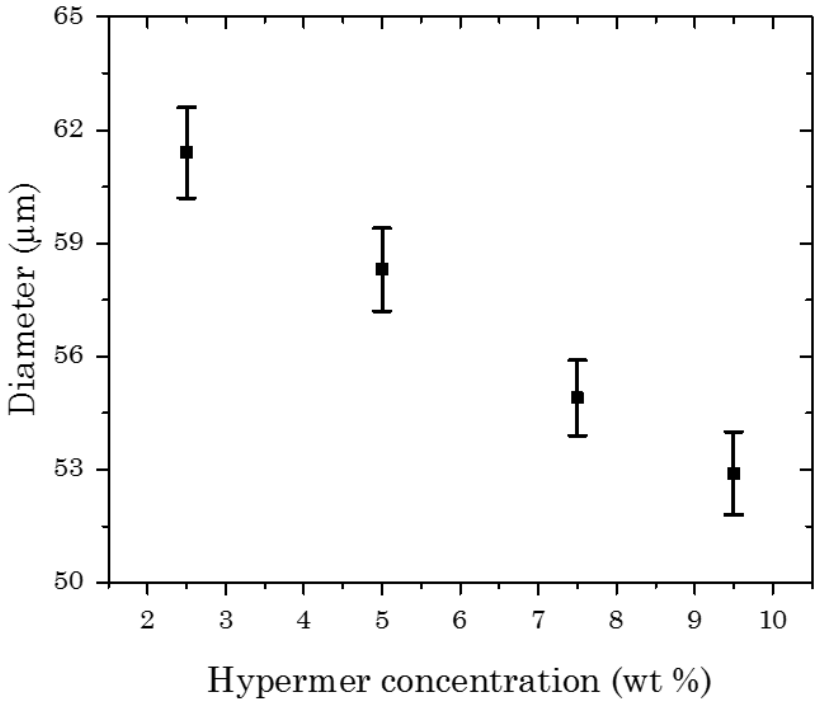

Figure 3.28: Mean diameter of water droplets in the oil phase as a function of hypermer concentration (black squares). The bars around the data points represent the standard deviation from the mean diameter.

For each surfactant concentration, approximately 6000 droplets were considered to estimate the mean diameter and standard deviation (SD). The mean diameter decreases when the surfactant concentration is increased. The size distribution of the droplets is represented by calculating the SD of the droplet size from the mean diameter. Although the mean diameter of the droplets decreased with the increase in hypermer concentration, the estimated SD remains approximately the same.

Before ripening these droplets using the rotavapor, the stability of the water droplets were checked using optical microscopy as a function of time. Figure 3.29 represents the mean diameter of the water droplets measured using optical microscopy after 7days. It can be seen that the mean diameter decreased drastically ($\approx$ 16 µm) without any external influence (pressure or temperature). The estimated SD deviation also increased with the

time. This decrease in size might be due to the presence of excess micelles in the oil phase which seems to pump the water away from the water droplets. A phenomena which was also observed in bulk emulsions when hypermer was used as the surfactant.

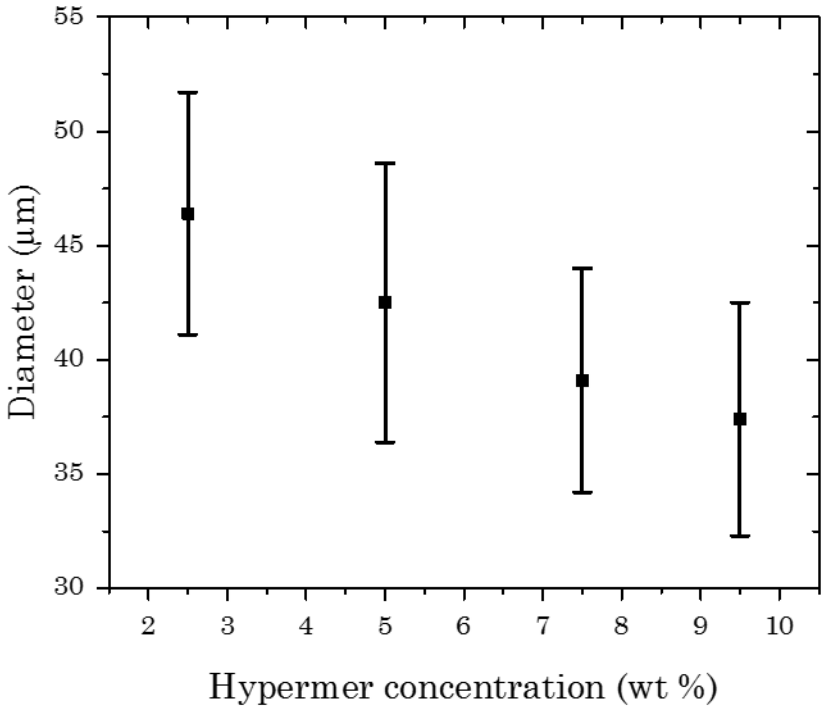

Figure 3.29: Mean diameter and SD of water droplets in the w/o emulsions 7 days after producing using the microfluidic chip.

The resulting water-in-oil emulsion is then transferred to the rotavapor for the ripening of water droplets. Although this system seemed stable before the ripening process, the droplets destabilized in the rotavapor during the ripening process. Thus, this system could no longer be used to produce the clusters.

3.5.2 Silicone oil-KF6017

Silicone oil with two different kinematic viscosities (5 and 10 cSt) mixed with surfactant KF6017 (2.5 wt%) were then used as the continuous phase. The mean diameter and the SD of the resulting droplets are shown in Figure 3.30. The decrease in viscosity led to an increase in the mean diameter, but it also decreased the size distribution of the produced droplets. The stability of the droplets as a function of time were checked using the optical microscope and no drastic changes in the droplet size or SD were observed. The emulsions were then transferred to the rotavapor for the ripening process. During the ripening process, no visible destabilization of the droplets was observed. After ripening, the final solution obtained was transparent unlike the final solution from the bulk emulsion which exhibited a blueish colour. This is due to the low concentration of clusters in the final solution.

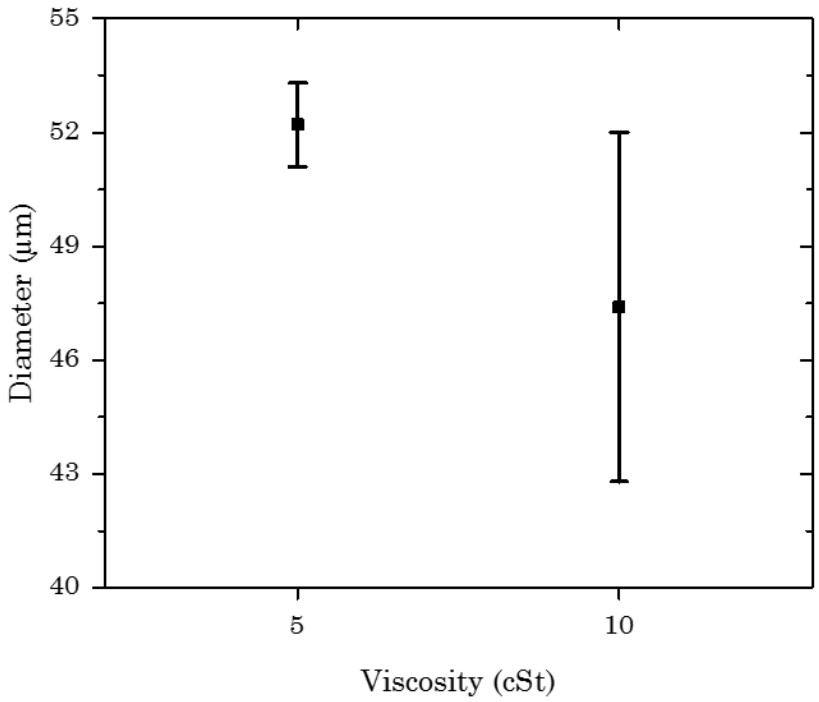

Figure 3.30: Mean diameter and SD of water droplets in the w/o emulsions as a function of silicone oil viscosity.

All the three systems detailed in this chapter led to the formation of satellite droplets with size in the range of 4 μm. The impact of these satellites was neglected since they would contain just about 3 gold NPs when compared to the other water droplets which contain about 3400 to 8000 NPs for droplets with size 47 to 63 μm.

In-order to increase the concentration of water droplets in the oil phase (comparable to bulk emulsions), we produced droplets continuously for about 4 days and the final emulsion was ripened using the rotavapor. Due to the high volume of water in the emulsion it took about 5 days to completely ripen the water droplets. However, the concentration of clusters were still very low to exhibit a visible color difference in the sample.

3.6 Bulk emulsion vs Microfluidics

The droplet based microfluidic method, although it has the advantage of producing a monodisperse system, still lacks many key features which makes it difficult in producing monodisperse NP clusters. One of the main challenge faced in microfluidics was finding the right system to produce the emulsion. Unlike bulk emulsion, for which more than one system was identified to produce a stable emulsion, it was hard to find a surfactant which could stabilize the droplets in the microfluidic chips. Surfactants such as DC5225 which worked well in the bulk method were not good enough to stabilize the droplets produced by the microfluidic method even when the surfactant concentration was increased to 20 wt%. This is due to the key difference between the surfactant adsorption in

the bulk method and microfluidic channels. Depending on the time scale of droplet formation, adsorption of the surfactant has to be fast enough to ensure stabilization before droplet coalescence. Within the microfluidics channels, the surfactant transport towards the droplet occurs by diffusion unlike the convective process which dominates in the bulk emulsion. Therefore the emulsions in the bulk process can be stabilized within minutes which is not the case in microfluidics.

Another key difference is the concentration of clusters that can be produced as a function of time. In a bulk emulsion, approximately 10^9 water droplets per 8 ml of solution can be produced within 20 min. To produce the same number of water droplets using microfluidics it would take about 4 days, even then these droplets would be dispersed in a much higher volume of oil phase when compared to bulk emulsions.

The time taken to ripen the water droplets from the bulk emulsion is also drastically less than the time taken to ripen the droplets from the microfluidics experiments. This is due to the fact that the microfluidics produces much larger droplets ($\approx$ 50 µm in diameter) when compared to bulk emulsion ($\approx$ 7 µm in diameter). It is possible to produce smaller droplets using microfluidics by using microfluidic chips having a smaller nozzel. These chips also come with a filter at the input channel in order to avoid clogging of the channels, however the polymer molecules used for the stabilization of the NPs as well as some insolube part of the surfactant also seemed to get stuck at the filter thus altering the fluid flow rates with time. The change in the flow rates will cause a change in the size of the droplets thus introducing more polydispersity to the final droplet size.

3.7 Conclusion

In conclusion, in this chapter we presented two different methods to produce a water-in-oil emulsion, which was further used to fabricate clusters of gold NPs. The bulk emulsion method resulted in a stable suspension of clusters although the clusters were polydisperse in size. The control on the structure of the clusters were also demonstrated using SAXS.

On the other hand, the droplet based microfluidic method could not be successfully used to produce a monodisperse suspension of gold NP clusters due to many challenges. The first challenge arises in finding a suitable system to produce a stable emulsion. Even though some surfactants succeeded in producing a stable emulsion, most systems destabilized during the ripening process. The systems which did not destabilize, gave rise to a final solution with a very low concentration of clusters that could not be detected by X-ray scattering or UV-Vis spectroscopy.

An alternative approach would be to use an oil-in-water (direct) emulsions instead. The main advantage of direct emulsions is that there are surfactants such as Sodium dodecyl sulfate (SDS) or Polyvinyl alcohol (PVA) which can produce a very stable emulsion.

These surfactants were also tested during this thesis and the stability of the droplets before and ripening were studied. However the challenge in this case is to produce NPs in a volatile oil phase such as hexane. It is also possible to simply buy NPs (gold or silver) dispersed in hexane.

3.8 Reference

[1] W. Chen, J. Guo, Q. Zhao, P. Gopalan, A. T. Fafarman, A. Keller, M. Zhang, Y. Wu, C. B. Murray, and C. R. Kagan, "Designing strong optical absorbers via continuous tuning of interparticle interaction in colloidal gold nanocrystal assemblies," *ACS nano*, vol. 13, no. 7, pp. 7493–7501, 2019. 74

[2] N. Vilanova, C. Solans, and C. Rodríguez-Abreu, "Preparation of novel silicone multicompartment particles by multiple emulsion templating and their use as encapsulating systems," *Langmuir*, vol. 29, no. 49, pp. 15414–15422, 2013. 76

[3] S.-H. Kim, S. Y. Lee, G.-R. Yi, D. J. Pine, and S.-M. Yang, "Microwave-assisted self-organization of colloidal particles in confining aqueous droplets," *Journal of the American Chemical Society*, vol. 128, no. 33, pp. 10897–10904, 2006. 79

[4] S. Mühlig, A. Cunningham, S. Scheeler, C. Pacholski, T. Bürgi, C. Rockstuhl, and F. Lederer, "Self-assembled plasmonic core–shell clusters with an isotropic magnetic dipole response in the visible range," *ACS nano*, vol. 5, no. 8, pp. 6586–6592, 2011. 80, 85

[5] A. Rostek, D. Mahl, and M. Epple, "Chemical composition of surface-functionalized gold nanoparticles," *Journal of Nanoparticle Research*, vol. 13, no. 10, pp. 4809–4814, 2011. 80

[6] S. Alexander, "Polymer adsorption on small spheres. a scaling approach," *Journal de physique*, vol. 38, no. 8, pp. 977–981, 1977. 88

[7] M. R. Bourgeois, A. T. Liu, M. B. Ross, J. M. Berlin, and G. C. Schatz, "Self-assembled plasmonic metamolecules exhibiting tunable magnetic response at optical frequencies," *The Journal of Physical Chemistry C*, vol. 121, no. 29, pp. 15915–15921, 2017. 91

[8] R. S. Farr and R. D. Groot, "Close packing density of polydisperse hard spheres," *The Journal of chemical physics*, vol. 131, no. 24, p. 244104, 2009. 92

[9] S.-Y. Teh, R. Lin, L.-H. Hung, and A. P. Lee, "Droplet microfluidics," *Lab on a Chip*, vol. 8, no. 2, pp. 198–220, 2008. 96

[10] I. Kobayashi, K. Uemura, and M. Nakajima, "Formulation of monodisperse emulsions using submicron-channel arrays," *Colloids and Surfaces A: Physicochemical and Engineering Aspects*, vol. 296, no. 1-3, pp. 285–289, 2007. 96

[11] Y.-C. Tan, J. S. Fisher, A. I. Lee, V. Cristini, and A. P. Lee, "Design of microfluidic channel geometries for the control of droplet volume, chemical concentration, and sorting," *Lab on a Chip*, vol. 4, no. 4, pp. 292–298, 2004. 96

[12] P. Umbanhowar, V. Prasad, and D. A. Weitz, "Monodisperse emulsion generation via drop break off in a coflowing stream," *Langmuir*, vol. 16, no. 2, pp. 347–351, 2000. 96

[13] R. Seemann, M. Brinkmann, T. Pfohl, and S. Herminghaus, "Droplet based microfluidics," *Reports on progress in physics*, vol. 75, no. 1, p. 016601, 2011. 96

[14] A. S. Utada, A. Fernandez-Nieves, H. A. Stone, and D. A. Weitz, "Dripping to jetting transitions in coflowing liquid streams," *Physical review letters*, vol. 99, no. 9, p. 094502, 2007. 96

[15] J. Xu, G. Luo, S. Li, and G. Chen, "Shear force induced monodisperse droplet formation in a microfluidic device by controlling wetting properties," *Lab on a Chip*, vol. 6, no. 1, pp. 131–136, 2006. 97

[16] J. N. Lee, C. Park, and G. M. Whitesides, "Solvent compatibility of poly (dimethylsiloxane)-based microfluidic devices," *Analytical chemistry*, vol. 75, no. 23, pp. 6544–6554, 2003. 97

[17] P. Garstecki, M. J. Fuerstman, H. A. Stone, and G. M. Whitesides, "Formation of droplets and bubbles in a microfluidic t-junction—scaling and mechanism of break-up," *Lab on a Chip*, vol. 6, no. 3, pp. 437–446, 2006. 97

[18] C. Cramer, P. Fischer, and E. J. Windhab, "Drop formation in a co-flowing ambient fluid," *Chemical Engineering Science*, vol. 59, no. 15, pp. 3045–3058, 2004. 97

[19] Z. Nie, M. Seo, S. Xu, P. C. Lewis, M. Mok, E. Kumacheva, G. M. Whitesides, P. Garstecki, and H. A. Stone, "Emulsification in a microfluidic flow-focusing device: effect of the viscosities of the liquids," *Microfluidics and Nanofluidics*, vol. 5, no. 5, pp. 585–594, 2008. xviii, 97, 98

[20] X. Zhang and O. A. Basaran, "An experimental study of dynamics of drop formation," *Physics of fluids*, vol. 7, no. 6, pp. 1184–1203, 1995. 97

Chapter 4

Optical study of the resonators

Contents

Summary: In this chapter, we describe the analytical tools and methods employed to study the optical properties of the synthesized clusters. This chapter will detail on the variable angle SLS measurements and their analysis, which will further be used to show the resonant and directional light scattering properties of the clusters and the influence of multipolar contributions in their scattering pattern.

4.1 Static light scattering technique

The light scattering properties of clusters of gold NPs stabilized using different polymers were studied using the SLS setup described in Section 2.1.3.2. In a first experiment, the clusters were analysed at a scattering angle $\theta = \pi/2$. At this scattering angle, information on the presence of electric and magnetic dipolar and quadrupolar modes can be extracted [1, 2, 3]. This setup was then modified to measure the scattering intensities at angles ranging from 20 to 140°. This modification not only allows one to study the directional scattering properties of the synthesized clusters, but also the influence of higher order multipoles in their scatttering pattern.

4.1.1 Static light scattering measurements at 90°

The optical measurements were performed using the setup shown in Figure 2.5. As explained in Section 2.1.3.3, the light scattering properties of a dilute suspension of particles (NPs or clusters) are studied across the wavelength range from 440 to 900 nm, at a scattering angle $\theta = \pi/2$. The light scattered with polarization parallel and perpendicular to the scattering plane is collected using a spectrophotometer through a polarizer. The relationship between the incident and the scattered light for an isotropic scatterer is shown below:

$$\begin{pmatrix} E_{\parallel S} \\ E_{\perp S} \end{pmatrix} = \frac{e^{ikr}}{-ikr} \begin{pmatrix} S_2(\theta,\phi) & 0 \\ 0 & S_1(\theta,\phi) \end{pmatrix} \begin{pmatrix} E_i \cos\phi \\ E_i \sin\phi \end{pmatrix} \tag{4.1}$$

S_j represents the amplitude scattering matrix, and is a function of θ and ϕ. However, for isotropic scatterers S_j does not depend on ϕ and the non diagonal terms S_3 and S_4 vanish [4].

For $\theta = 90°$, the scattering multipoles split up into two separate series as:

$$S_1 = \frac{3}{2}a_1 - \frac{5}{2}b_2 - \frac{7}{8}a_3 + \ldots \tag{4.2a}$$

$$S_2 = \frac{3}{2}b_1 - \frac{5}{2}a_2 - \frac{7}{8}b_3 + \ldots \tag{4.2b}$$

Where, a_n and b_n stands for the different polar orders of the electric and magnetic contributions respectively. For the systems studied in this thesis, S_1 collects essentially the electric dipole (ED, a_1) and magnetic quadrupole (MQ, b_2) contribution and S_2 corresponds to the magnetic dipole (MD, b_1) and electric quadrupole (EQ, a_2) contributions.

By neglecting the high order terms, S_1 and S_2 can be written as the following:

$$S_1 \approx \frac{3}{2}a_1 - \frac{5}{2}b_2 \tag{4.3a}$$

$$S_2 \approx \frac{3}{2}b_1 - \frac{5}{2}a_2 \tag{4.3b}$$

The intensities measured along the two output polarizations for isotropic scatterers then read:

$$I_{\perp S} = I_0(\lambda)\, n_c\, \frac{|S_1(90°)|^2}{k^2}\, \delta\Omega\, T(\lambda)\, g(\lambda, \delta\Omega) \cos^2\phi \tag{4.4a}$$

$$I_{\parallel S} = I_0(\lambda)\, n_c\, \frac{|S_2(90°)|^2}{k^2}\, \delta\Omega\, T(\lambda)\, g(\lambda, \delta\Omega) \sin^2\phi \tag{4.4b}$$

in which $I_0(\lambda)$ is the spectral irradiance of the incident beam, n_c is the number of clusters in the scattering volume, and $\delta\Omega$ is the solid angle of the detection window. $g(\lambda, \delta\Omega)$ is an unknown function that accounts for the spectral sensitivity of the detector and optical transmission or reflection of all optical elements. The spectral transmission $T(\lambda)$ accounts for the absorbance of the suspension. The two intensities are then fitted to a simple function to obtain,

$$I_{\perp S} = B_V + A_V \cos^2\phi \tag{4.5a}$$

$$I_{\parallel S} = B_H + A_H \sin^2\phi \tag{4.5b}$$

The background (B_V and B_H) was measured to be very weak with, $B_V \approx B_H \leq 0.05 A_V$, stipulating that the optical response of the clusters is isotropic [5]. The amplitudes A_V and A_H are then normalized using a model dispersion of silica NPs (refer Equation 2.17) measured using the same experimental parameters as the sample. This is done to eliminate the unknown experimental parameters ($I_0(\lambda)$, $\delta\Omega$ and $g(\lambda, \delta\Omega)$) in Equation 4.4. A simple way to access the presence or absence of MD and/or EQ is by calculating the ratio of the two measured amplitudes (A_H/A_V) which can even be done without any normalization step. Gold NPs suspension is a good example of a system exhibiting only electric dipolar mode as shown in Figure 4.1.

The scattering properties of gold NPs dispersed in water are first measured and normalized with the silica NPs (refer Equation 2.17). The scattered light measured for the two output polarization (A_V and A_H) are shown in Figure 4.1. The measured A_V scattering intensity exhibit a resonance at 610 nm. From Figure 4.1, it is obvious that the gold NPs dispersion does not exhibit any MD mode, since A_H is zero.

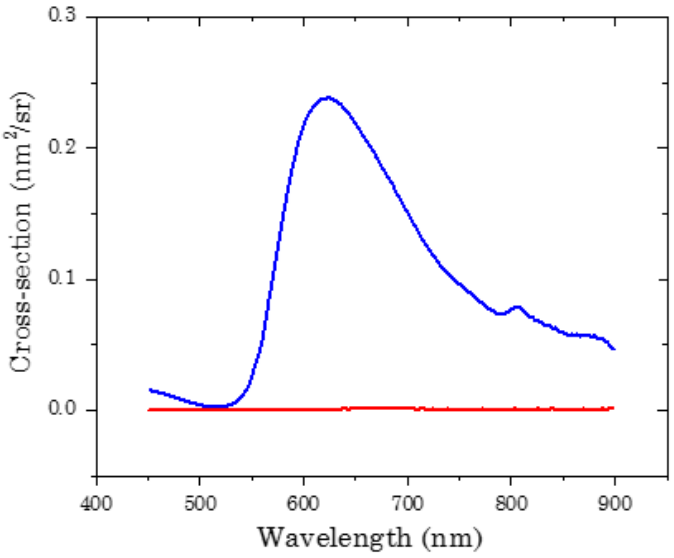

Figure 4.1: Experimental normalized scattering intensities of A_V (intensity measured with polarization orthogonal to the scattering plane, blue line) and A_H (intensity measured with polarization parallel to the scattering plane, red line) at a scattering angle $\theta = 90°$ for a suspension of gold NPs of diameter 13.6 nm in water.

The MD mode can be introduced into the system by bringing the NPs together to form a cluster as shown through simulations [6, 7]. Simulations performed by Romain Dezert [7] show the influence of the size of the gold clusters and the volume fraction (f) of gold NPs inside the cluster on the final scattering efficiency of the clusters, see Figure 4.3 and 4.2 respectively. The scattering efficiency (Q) is defined as the scattering cross-section of the scatterer divided by its geometrical cross-section. For an isotropic scatterer, the scattering (Q_s), extinction (Q_{ext}) and absorption (Q_{abs}) efficiency are expressed as :

$$Q_s = \sigma_s / \pi.R^2 \tag{4.6a}$$

$$Q_{ext} = \sigma_{ext} / \pi.R^2 \tag{4.6b}$$

$$Q_{abs} = \sigma_{abs} / \pi.R^2 \tag{4.6c}$$

Where, σ_s, σ_{ext} and σ_{abs} represent scattering cross-section, extinction cross-section and absorption cross-section respectively. R is the radius of the scatterer. Simulations performed using the Maxwell Garnet model and assuming a monodisperse cluster made of gold NPs with radius 6.8 nm are shown in Figure 4.3 and 4.2. The refractive index of the material in between the NPs is assumed to be 1.5 and that of the medium surrounding the cluster is 1.33. These simulations indicate that both the increase in volume fraction (f) as well as the radius of cluster (R) lead to a strong MD contribution along with a red shift in their spectral position. Nevertheless, both MD and ED contributions occur at approximately the same wavelength, which is a key feature to obtain Huygens scattering.

Figure 4.3 also indicates that an increase in the size of the cluster induces an increase in the quadrupolar contribution to the total scattering efficiency.

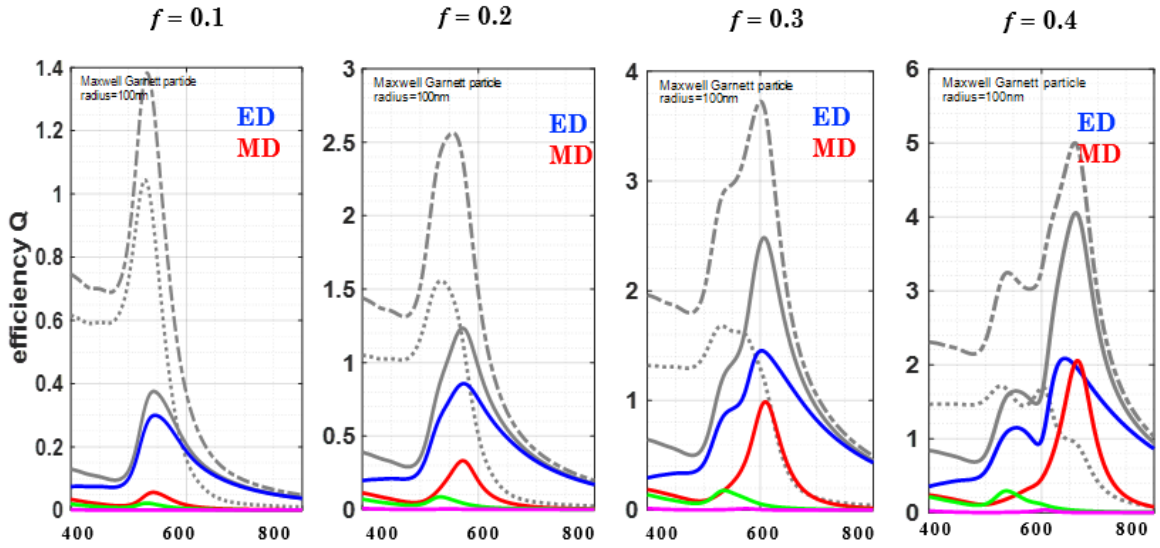

Figure 4.2: Simulated scattering efficiency of a gold cluster with radius R_C = 100 nm as a function of volume fraction (f) of gold NPs in the cluster. The curves show the contribution of the ED (blue line), MD (red line), EQ (green line) and MQ (pink line) to the total scattering cross section (grey line). The absorption cross section (dotted line) and extinction cross section (dashed line) are also shown.

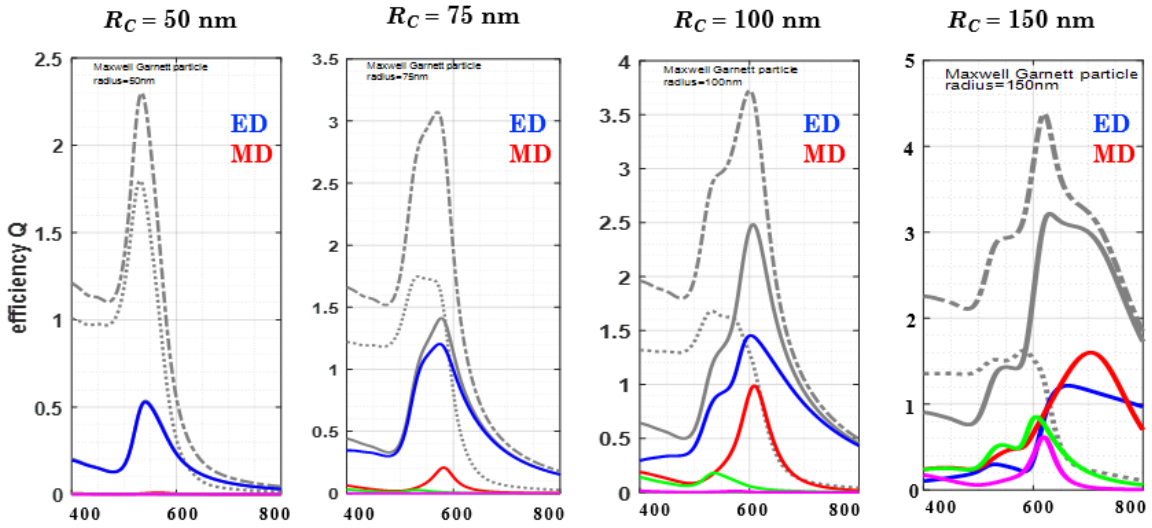

Figure 4.3: Simulated scattering efficiency of a gold cluster with f = 0.3 as a function of cluster radius. The curves show the contribution of the ED (blue line), MD (red line), EQ (green line) and MQ (pink line) to the total scattering cross section (grey line). The absorption cross section (dotted line) and extinction cross section (dashed line) are also shown.

The optical properties of the clusters formulated using the emulsion formulation route were then experimentally analyzed using the SLS setup. Figure 4.4 shows the results obtained with the gold clusters made from NPs stabilized with citrate ions. The measured intensities once again indicate no MD contribution. The absence of a resonance peak in

A_V could signify the destabilization of the NPs leading to their uncontrolled aggregation within the NP cluster. This further shows the importance of the stability of the gold NPs through the emulsification and ripening process.

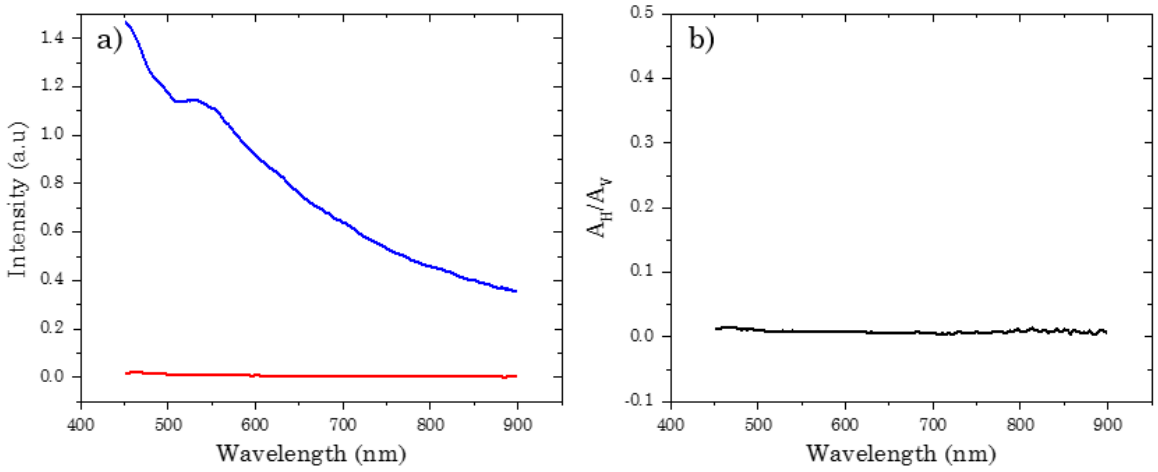

Figure 4.4: a) Experimental normalized scattering intensities of A_V (blue line) and A_H (red line) for the gold clusters made from citrate-NPs at a scattering angle $\theta = 90°$. b) Experimental ratio of A_H to A_V as a function of wavelength λ.

We performed the same measurements for clusters made with various ligands of gold NPs. The experimental maximum A_H/A_V ratios measured for these clusters are shown in Table 4.1. These results are discussed in detail in the following.

Sample name	**Polymer**	**Molar mass (g/mol)**	**Surface density (mol/nm^2)**	**Max A_H/A_V**	**f**
$C_{Au\text{-}PVP55k}$	PVP	55,000	-	0.063	-
$C_{Au\text{-}PVP29k}$	PVP	29,000	-	0.07	-
$C_{Au\text{-}PVP10k}$ (1)	PVP	10,000	-	0.15	-
$C_{Au\text{-}PVP10k}$ (2)	PVP	10,000	-	0.6	-
PEG6000-2	PEG	6,000	2	0.23	0.19
PEG6000-0.5	PEG	6,000	0.5	0.23	0.24
PEG5000-4	PEG	5,000	4	0.06	-
PEG2000-2	PEG	2,000	2	0.24	0.27
PEG2000-1	PEG	2,000	1	0.3	0.40
PEG2000-0.5	PEG	2,000	0.5	0.12	0.53
PEG800-4	PEG	800	4	0.65	0.46
PEG800-1	PEG	800	1	0	-

Table 4.1: Experimental A_H/A_V ratio obtained for clusters of gold NPs stabilized using different polymer ligand.

4.1.1.1 SLS results for clusters of Au-PVP NPs

Gold NPs stabilized with three different molar mass (55k, 29k, 10k g/mol) of PVP were used to fabricate gold clusters. Table 4.1 shows that the increase in molar mass decreased the experimental A_H/A_V ratio measured using the SLS setup. The value attained using PVP 10 Kg/mol ranged between 0.15 to 0.6. This differences in the ratio value even though the molar mass was kept constant is due to the difference in the volume fraction of gold NPs inside the cluster. The measured A_V and A_H intensities along with the TEM image for two samples (which are named as $C_{Au\text{-}PVP10k}$ (1) and $C_{Au\text{-}PVP10k}$ (2) in Table 4.1) are shown in Figure 4.5. The TEM image in Figure 4.5 c, shows the presence of small apparent voids within the spherical cluster. These voids are most probably due to the presence of excess PVP molecules in the initial NPs suspension. Therefore, in order to increase the NPs volume fraction within the cluster, the initial gold NPs solution is washed several times by centrifugation and pure water addition to remove the excess polymer. The resulting suspension was then used to fabricate the gold NP clusters ($C_{Au\text{-}PVP10k}$ (2)) with a higher f. As it can be seen from Figure 4.5 f, the additional washing steps helped in removing the excess polymer molecules thus increasing the NPs volume fraction within the cluster.

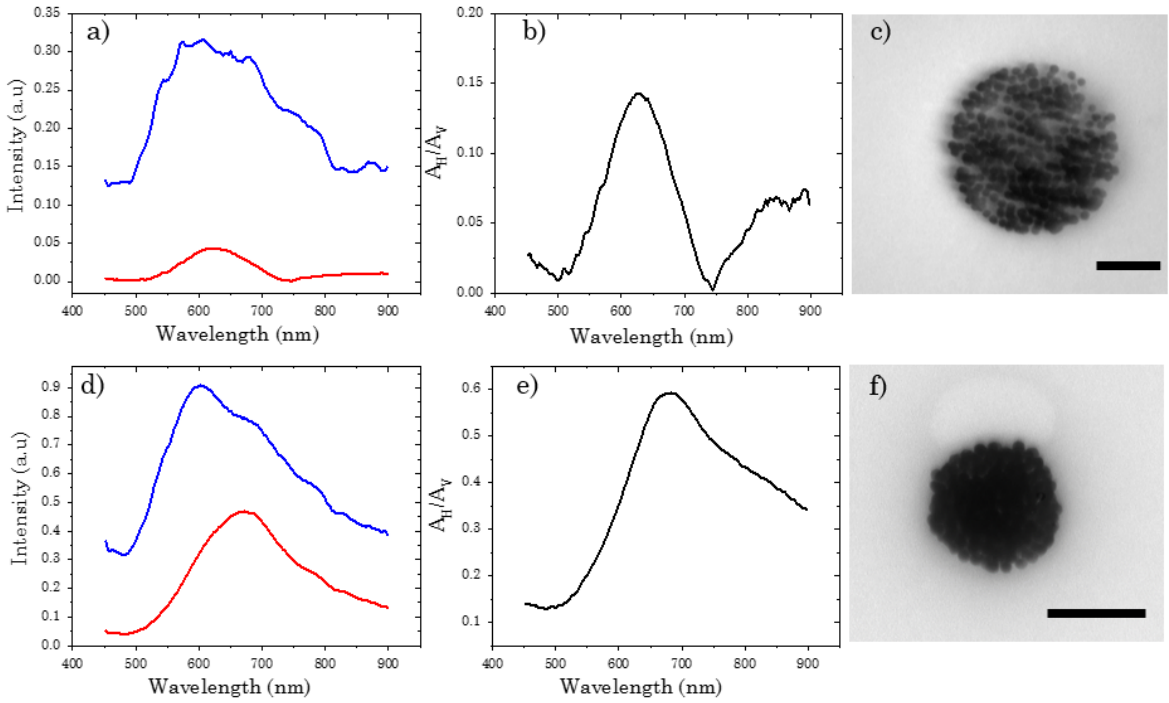

Figure 4.5: Scattering intensities of A_V (blue line) and A_H (red line) at a scattering angle $\theta = 90°$ for sample a) $C_{Au\text{-}PVP10k}$ (1) and d) $C_{Au\text{-}PVP10k}$ (2); b) Ratio of A_H to A_V as a function of wavelength λ for sample $C_{Au\text{-}PVP10k}$ (1) b) and $C_{Au\text{-}PVP10k}$ (2) e). TEM images of the synthesized clusters for sample $C_{Au\text{-}PVP10k}$ (1) c) and $C_{Au\text{-}PVP10k}$ (2) f). The scale bar is set to 100nm.

The increase in volume fraction not only increased the contribution from MD (and EQ) but also caused their resonance frequency to red shift. This behaviour is also witnessed in the simulations shown in Figure 4.2 when increasing the gold volume fraction f inside the clusters. Although the Au-PVP system gave good results, the additional washing

step sometimes led to the aggregation of the initial NPs suspension. Moreover, a precise control over the quantity of PVP molecules adsorbed onto the surface of the gold NPs did not seem possible to reach. For this reason PEG-SH molecules were chosen to be grafted onto the NPs surface instead of PVP.

4.1.1.2 SLS results for clusters of Au-PEG NPs

SLS measurements were also performed on gold clusters fabricated using PEG-SH as the NP stabilizing agent. The advantage of PEG-SH stabilized NPs over PVP, is that, the quantity of PEG-SH molecules adsorbed onto the NPs surface can be controlled more precisely. As discussed in Chapter 3 Section 3.3.3.2, we were able to extract the gold volume fraction f within the clusters from the SAXS data, as a function of the ligand molar mass and surface density. The volume fraction of the synthesized clusters as a function of PEG polymer molar mass and surface density is shown in Table 3.2 and also reported in Table 4.1. The predicted increase in A_H/A_V ratio value is not obvious from the results shown in Table 4.1, which means that other parameters (possible presence of voids in the cluster) also influence the optical scattering response of the clusters.

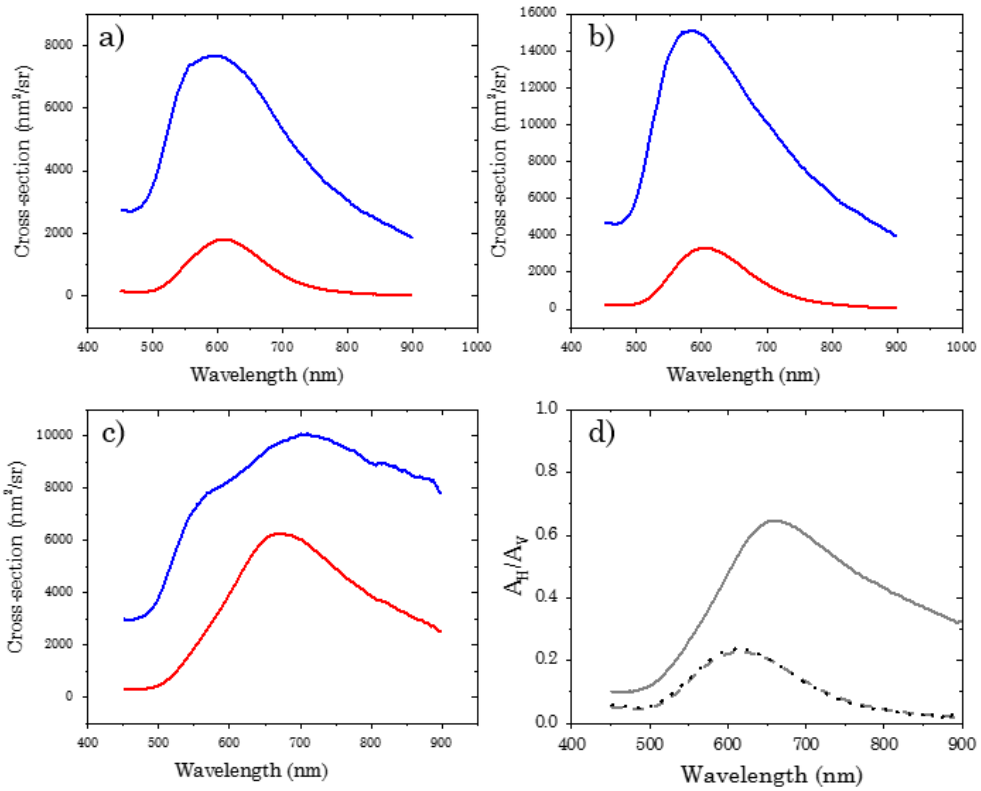

Figure 4.6: Differential scattering cross-section of σ_V (blue line) and σ_H (red line) at a scattering angle $\theta = 90°$ for sample a) PEG-6000-2 and b) PEG-2000-2 and c) PEG-800-4. d) Ratio of A_H to A_V as a function of wavelength λ for PEG-800-4 (grey solid line), PEG-2000-2 (grey dashed line) and PEG-6000-2 (black dots).

The experimental A_H/A_V ratio measured for three different polymer molar mass are shown in Figure 4.6 d. The absolute scattering cross-section values for the three sam-

ples were extracted by introducing the concentration of cluster (n_c) and reference silica beads (n_{ref}) in their respective suspension into the Equation 4.7. Due to the experimental uncertainties on the cluster concentrations ($6.8 \times 10^{10} \leq n_c \leq 8.8 \times 10^{10}$ particles/L), the minimum value of the concentration ratio, $\frac{n_{\text{ref}}}{n_c} = 2160$ was used, to extract a *lower bound* of the clusters scattering cross-sections.

$$\sigma_V(\theta = 90^\circ) = \frac{n_{\text{ref}}\, A_V(\lambda)\, T_{\text{ref}}(\lambda)}{n_c\, A_V^{\text{ref}}(\lambda)\, T(\lambda)}\, \sigma_{\text{ref}}^{\theta=90^\circ} \tag{4.7a}$$

$$\sigma_H(\theta = 90^\circ) = \frac{n_{\text{ref}}\, A_H(\lambda)\, T_{\text{ref}}(\lambda)}{n_c\, A_H^{\text{ref}}(\lambda)\, T(\lambda)}\, \sigma_{\text{ref}}^{\theta=90^\circ} \tag{4.7b}$$

The spectral position and relative amplitudes of the two resonant modes are shown in Figure 4.6. As shown in Fig.4.6, the differential scattering cross-sections (σ_V and σ_H) measured at $\theta = 90^\circ$ increases significantly between the PEG6000-2 (Figure 4.6 (a), gold volume fraction $f \approx 0.19$) and the PEG2000-2 (Figure 4.6 (b), $f \approx 0.27$). Surprisingly, the value of σ_V is decreasing upon increasing f further to 0.46, while σ_H increases strongly (Figure 4.6 (c)), which will be explained in the next section. It is evident from the graphs that increasing the cluster gold volume fraction f leads to a red shift, from $\lambda \approx 590$ nm for PEG6000-2 to $\lambda \approx 670$ nm for PEG800-4, and to a spectral broadening of the resonances. This trend is once again witnessed when the volume fraction is further increased from 0.46 to 0.53 (refer Figure 4.7). Although this sample exhibits a very low A_H/A_V ratio, it nevertheless leads to interesting directional scattering results (further explained in Section 4.1.2).

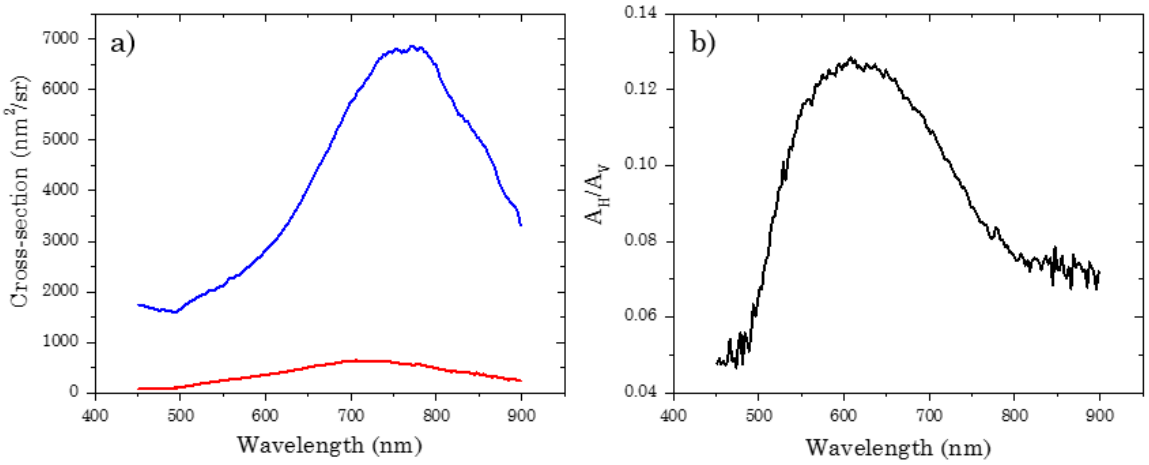

Figure 4.7: a) Differential scattering cross-section of σ_V (blue line) and σ_H (red line) at a scattering angle $\theta = 90^\circ$ for PEG-2000-0.5 NP clusters. b) Ratio of A_H to A_V as a function of wavelength λ for PEG-2000-0.5 NP clusters.

The influence of the size of the clusters on the optical scattering properties was also studied by synthesizing clusters of varying mean radius. This can be achieved by either

varying the size of the initial water droplets in the water-in-oil emulsion or by varying the concentration of NPs in the water phase. The latter method was chosen to produce clusters of three different mean radius namely, ≈ 60 nm, ≈ 120 nm and ≈ 140nm. The differential scattering cross-section for the three samples are shown in Figure 4.8. First, there is a significant increase of the MD contribution to the total scattering as the size of the cluster increases. Secondly, there is no significant shift in the spectral position of MD (A_H) resonance with the increase in the cluster size however, the spectral position of the ED resonance seems to have blue shifted when the size of the clusters is increased from 120 to 140 nm. Hence the ratio A_H/A_V (shown in Figure 4.8 d) increases from 0.02 to 0.71 when the radius of the clusters varies from 60 to 140 nm.

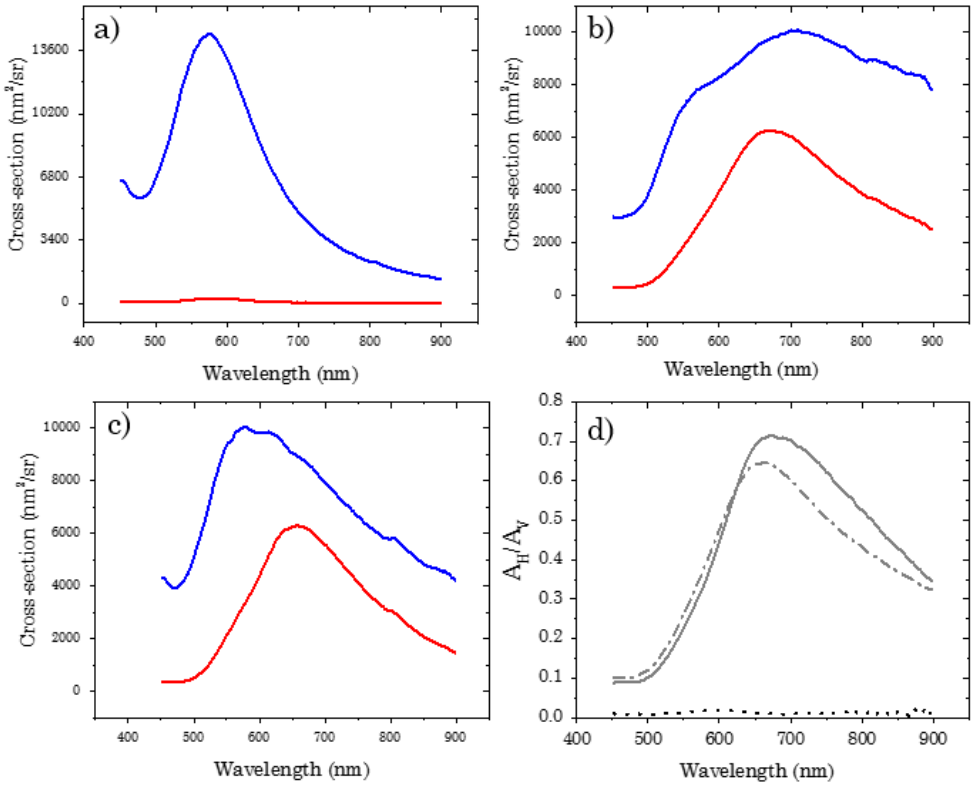

Figure 4.8: Differential scattering cross-section of σ_V (blue line) and σ_H (red line) at a scattering angle $\theta = 90°$ for PEG-800-4. a) 60 nm b) 120 and c) 140nm. d) Ratio of A_H to A_V as a function of wavelength λ for PEG-800-4 with average radius 140 nm (grey solid line), 120 nm (grey dashed line) and 60 nm (black dots).

4.1.2 Variable angle static light scattering

The directional scattering properties of the produced clusters along with the influence of higher order multipoles in the total scattering were analyzed by measuring the scattering amplitudes for different scattering angles θ ranging from 20 to 140 ° with intervals of 5°.

The measured data for the samples are indicated as:

$I_{\perp S(\text{cluster})}(\phi, \theta, \lambda)$ - scattering intensities measured with polarization orthogonal to the

scattering plane as a function of polarization of incident light (ϕ), scattering angle (θ), and wavelength (λ) of incident light for the gold clusters.

$I_{\parallel S(cluster)}(\phi,\theta,\lambda)$ - scattering intensities measured with polarization parallel to the scattering plane as a function of polarization of incident light (ϕ), scattering angle (θ), and wavelength (λ) of incident light for the gold clusters.

Similarly, for the reference silica sample $I_{\perp S(silica)}(\phi,\theta,\lambda)$ and $I_{\parallel S(silica)}(\phi,\theta,\lambda)$ were measured.

Similar to the analysis at 90° the scattering intensities measured with polarization orthogonal and parallel to the scattering plane are first fitted to a simple function as shown below,

$$I_{\perp S(cluster)}(\phi,\theta,\lambda) = B + A_{V,cluster}(\theta,\lambda)\cos^2(\phi+\phi_{o,setup}) \tag{4.8a}$$

$$I_{\parallel S(cluster)}(\phi,\theta,\lambda) = B + A_{H,cluster}(\theta,\lambda)\sin^2(\phi+\phi_{o,setup}) \tag{4.8b}$$

$$I_{\perp S(silica)}(\phi,\theta,\lambda) = B + A_{V,cluster}(\theta,\lambda)\cos^2(\phi+\phi_{o,setup}) \tag{4.8c}$$

where, B, the background is small and can be neglected. The fits allow us to extract the scattering amplitudes $A_V(\theta,\lambda)$ and $A_H(\theta,\lambda)$ for all wavelengths, which then reads as,

$$A_{V,(cluster)}(\theta,\lambda) = I_0(\lambda)\; n_c\; \delta\Omega\, T(\lambda)\; g(\lambda,\delta\Omega)\; \sigma_{V,cluster}(\theta) \tag{4.9a}$$

$$A_{H,(cluster)}(\theta,\lambda) = I_0(\lambda)\; n_c\; \delta\Omega\, T(\lambda)\; g(\lambda,\delta\Omega)\; \sigma_{H,cluster}(\theta) \tag{4.9b}$$

$$A_{V,(silica)}(\theta,\lambda) = I_0(\lambda)\; n_{silica}\; \delta\Omega\, T(\lambda)\; g(\lambda,\delta\Omega)\; \sigma_{V,silica}(\theta) \tag{4.9c}$$

where, $I_0(\lambda)$ is the spectral irradiance of the incident beam, n_c is the number of clusters in the scattering volume, and $\delta\Omega$ is the solid angle of the detection window. $g(\lambda,\delta\Omega)$ is an unknown function that accounts for the spectral sensitivity of the detector and optical transmission or reflection of all optical elements. The spectral transmission $T(\lambda)$ accounts for the absorbance of the suspension which is dominated by the solvent (water in case of silica reference and oil in case of cluster suspension). The differential scattering cross sections of the cluster and silica are denoted by $\sigma_{V,H,cluster}$ and σ_{silica} respectively, and are expressed in nm^2/sr, where sr stands for steradians. The scattering cross-section of silica beads for a given radius as a function of scattering angle was also calculated using Mie theory.

Similar to the analysis at $\theta = 90°$, extracted scattering intensities (A_H and A_V) of the clusters are normalized with that of reference silica beads to eliminate the unknown pa-

rameters shown ($I_0(\lambda)$, $\delta\Omega$ and $g(\lambda,\delta\Omega)$) in Equation 4.9. The normalized data are further treated by multiplying the resultant with the calculated cross-section of silica ($\sigma_{th,V,silica(\theta,\phi)}$). This is done to extract the scattering cross section of the cluster (shown in Equation 4.10). The normalization then reads:

$$\text{Normalized } A_{V,cluster}(\phi,\theta,\lambda) = \frac{A_{V,cluster}(\phi,\theta,\lambda)}{A_{V,silica}(\phi,\theta,\lambda)}\,\sigma_{th,V,silica(\theta,\phi)} = \frac{n_c}{n_{silica}}\,\sigma_{V,cluster} \tag{4.10a}$$

$$\text{Normalized } A_{H,cluster}(\phi,\theta,\lambda) = \frac{A_{H,cluster}(\phi,\theta,\lambda)}{A_{V,silica}(\phi,\theta,\lambda)}\,\sigma_{th,V,silica(\theta,\phi)} = \frac{n_c}{n_{silica}}\,\sigma_{H,cluster} \tag{4.10b}$$

where, $\sigma_{th,V,silica(\theta,\phi)}$ is the theoretically calculated scattering cross section of silica NPs Mie scattering. If the concentration of clusters and the silica beads are known, it is then possible to determine the differential scattering cross-section $\sigma_{cluster}$ quantitatively.

The total normalized scattering cross-section ($\sigma_V(\lambda,\theta)+\sigma_H(\lambda,\theta)$, represented as $\sigma_{cluster}$ from here), as a function of scattering angle and wavelength, for three samples (PEG-6000-2, PEG-2000-2 and PEG-800-4) with different volume fraction but identical cluster radius ($R_c \approx 120$ nm) is shown in Figure 4.9. As can be seen, the scattering broadens spectrally, increases in strength and is directed towards smaller angles as the cluster density increases (from (a) to (c) in Fig: 4.9), in accordance with an increase of σ_H relative to σ_V (Figure 4.6). In particular, sample PEG-800-4 (Figure 4.6 c)) presents a narrow angle range of strong scattering, which explains why the maximum of σ_V at 90° for this sample is lower than the one of the less dense sample PEG-2000-2 (Fig: 4.6 b).

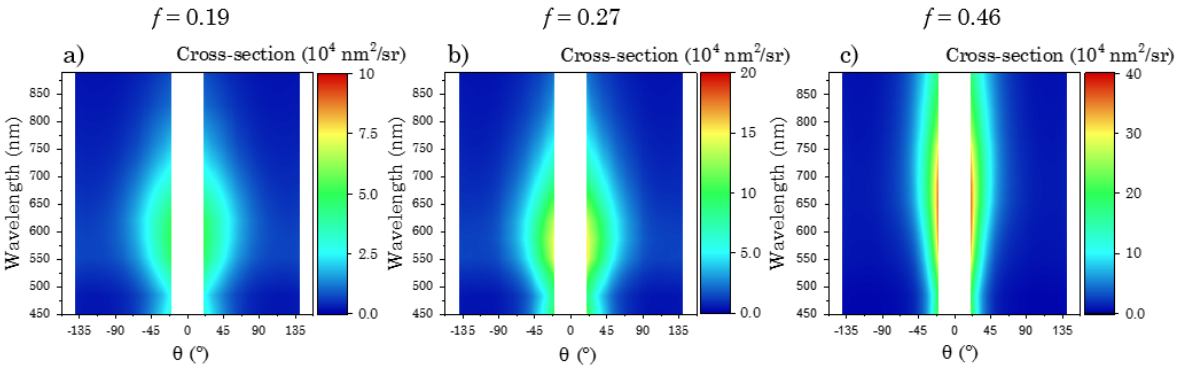

Figure 4.9: Experimental scattering patterns: values of the differential scattering cross-sections ($\sigma_{cluster}$) as a function of the wavelength λ and the scattering angle θ, for cluster samples a) PEG-6000-2 (gold volume fraction estimated at $f \approx 0.19$), b) PEG-2000-2 ($f \approx 0.27$) and c) PEG-800-4 ($f \approx 0.46$). We measured only for $\theta > 0$, but assumed that $\sigma_V(\lambda,-\theta)+\sigma_H(\lambda,-\theta) = \sigma_V(\lambda,\theta)+\sigma_H(\lambda,\theta)$. Note that the nm^2/steradian color scale is enhanced by a factor 2 going from (a) to (b) and by 2 again from (b) to (c).

The scattering intensity in the forward direction and the broad range of wavelength for which forward scattering is achieved both increases with the gold volume fraction. This is clearly shown with the help of the guide lines in Figure 4.10 and Figure 4.11. In case of the

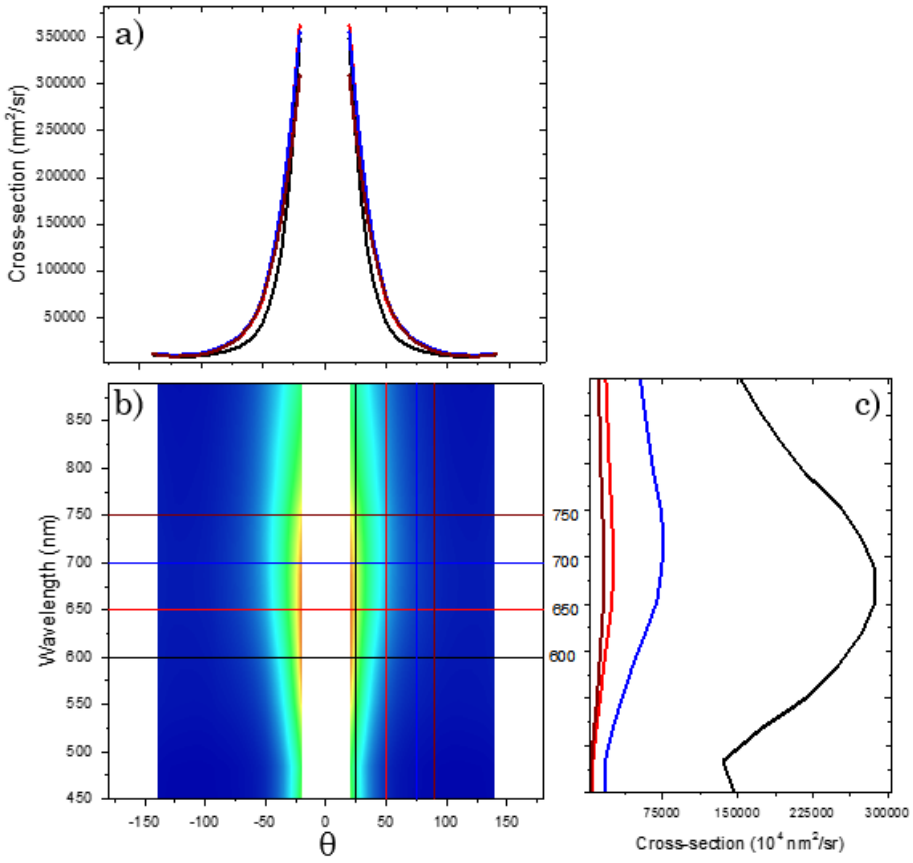

Figure 4.10: Experimental scattering patterns: values of the differential scattering cross-sections ($\sigma_{cluster}$) as a function of the a) wavelength λ and c) the scattering angle θ, for PEG-800-4 ($f \approx 0.46$). The color code in graph a) is used to indicates the scattering wavelength λ = 600 (black), 650 (red), 700 (blue) and 750nm (wine red) and in c) the scattering angle at θ = 25 (black), 50 (blue), 75 (red) and 90° (wine red).

denser sample (Fig. 4.10) the scattering intensity decreases drastically (>10 times) when the scattering angle is moved from 25 to 50 ° (at constant λ) as can be seen in Figure 4.10 c. For sample PEG-6000-2 the intensity decreases much more gradually (≈ 2 times)) with increasing the angle (Fig 4.11 c). As a function of the wavelength, the scattering intensity remains approximately the same from λ = 550 to 800 nm for sample PEG-800-4 (Fig 4.10 a) whereas, in case of PEG-6000-2, there is a rather narrow peak at λ ≈ 600 nm and the differential scattering cross-section is highly dependent on λ (Fig 4.11 a).

Another way to represent the forward scattering properties of the produced clusters is to plot a polar graph to indicate the scattering pattern as a function of angle at a fixed wavelength, as shown in Figure 4.12. Figure 4.12 a. also includes the scattering pattern of silica beads of radius 120 nm calculated from Mie theory for comparison, in a water solvent. The computed scattering intensity of silica beads is multiplied by a factor 100 (cyan line on Figure 4.12 a) so that it can be displayed on the same scale as the clusters scattering intensities. The evolution of scattering intensities as a function of wavelength for PEG-2000-2 is also shown in Figure 4.12 b. The scattering increases from λ = 520 to 620 nm, then decreases from λ = 620 to 750 nm, with the highest and most forward scattering

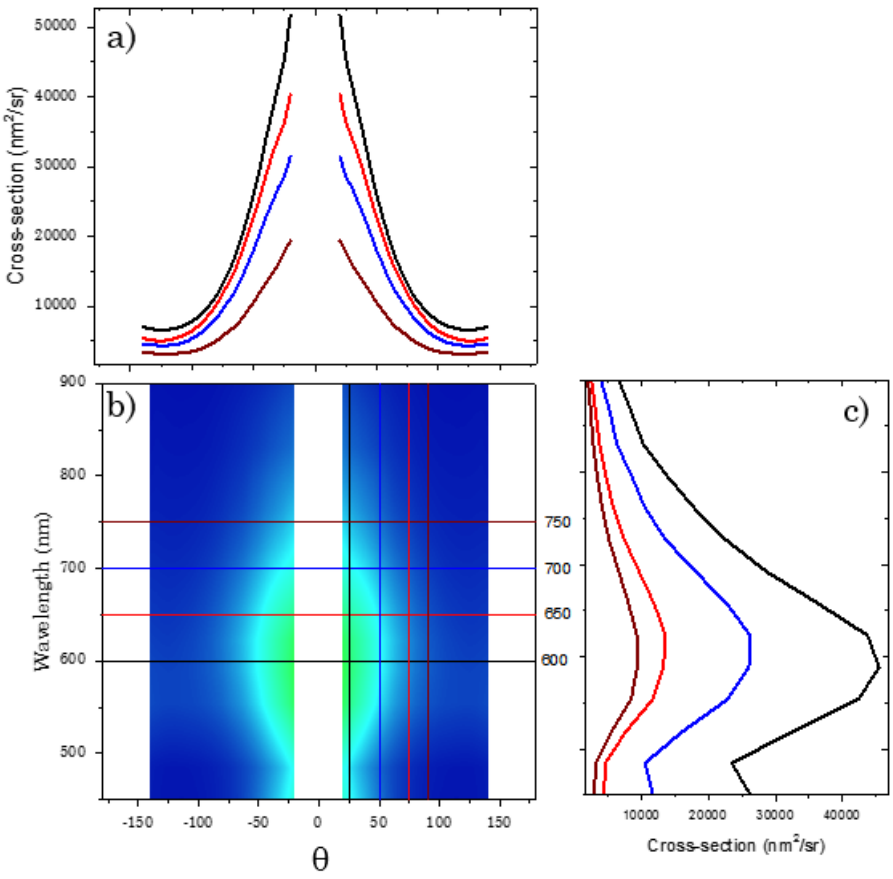

Figure 4.11: Experimental scattering patterns: values of the differential scattering cross-sections ($\sigma_{cluster}$) as a function of the a) wavelength λ and c) scattering angle θ, for cluster PEG-6000-2 ($f \approx 0.19$). The color code in graph a) is used to indicates the scattering wavelength at λ = 600 (black), 650 (red), 700 (blue) and 750nm (wine red) and in c) the scattering angle at θ = 25 (black), 50 (red), 75 (blue) and 90° (wine red).

occurring at λ = 620 nm, where the A_H/A_V ratio is maximum.

Both Figures 4.9 and 4.12 show that the scattering of the NP-clusters is strongly directed forward and increases in strength as the cluster density increases. For the three samples shown in Figure 4.12, the whole back hemisphere scattering, beyond 90°, is very low compared to the forward scattering (below 90°), and even more so for the denser clusters of sample PEG-800-4. Samples PEG-6000-2 ($f = 0.19$) and PEG-2000-2 ($f = 0.27$) have approximately the same A_H/A_V ratio at 90° (shown in Figure 4.6 d), but they exhibit significantly different scattering patterns: clusters of PEG-2000-2 NPs have a stronger forward scattering. This indicates that the results obtained at scattering angle 90° do not always accurately indicate if the sample is scattering forward or not.

This anomaly is also witnessed in sample PEG-2000-05: this sample presents a high volume fraction $f = 0.53$ (estimated from SAXS), exhibits a low A_H/A_V ratio at theta = 90° (shown in Fig. 4.7) but still exhibits a very strong forward scattering, as can be seen on Figure 4.13. The resonance frequency is shifted towards the longer wavelength, as is expected for high volume fraction clusters (see the numerical predictions in Figure 4.2). This

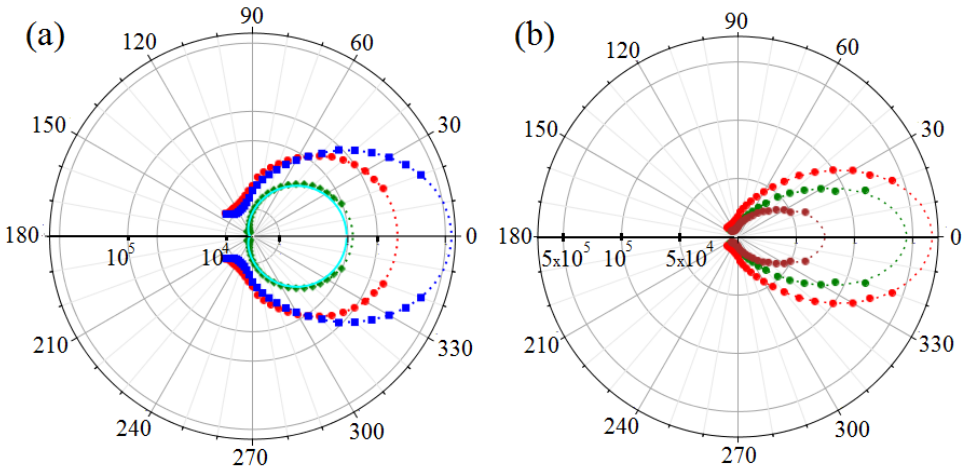

Figure 4.12: (a) Logarithmic polar plot of the experimental differential scattering cross-section ($\sigma_{cluster}$) for the three gold clusters PEG-6000-2 (gold volume fraction estimated at $f \approx 0.19$, green diamonds), PEG-2000-2 ($f \approx 0.27$, red circles) and PEG-800-4 ($f \approx 0.46$, blue squares) recorded at the maximum of the A_H/A_V ratio (620, 620 and 650 nm respectively). The full cyan line is the scattering of a silica nanoparticle of comparable size ($r_s = 110$ nm) computed from the Mie theory and multiplied by a factor 100 for a better visibility. (b) Linear polar plot of the differential scattering cross section for PEG-2000-2 NP clusters ($f \approx 0.27$) recorded at three wavelengths: 520 nm (green circles), 620 nm (the red circles show the same PEG-2000-2 NP clusters data at same wavelength on both polar plots) and 750 nm (brown circles). Note that the highest and most forward scattering occurs at 620 nm where the A_H/A_V ratio is maximum. Dotted lines are guides for the eye. The radial scales are in nm^2/sr.

sample scattering has a strong forward directionality, as sample PEG-800-4 NP clusters, but its differential scattering cross-sections are about 5 times less than the one of sample PEG-800-4.

The A_H/A_V ratio, although a good indicator for the presence of MD, is only valid in cases where the samples have contributions coming mostly from lowest order multipoles (dipoles and quadrupoles). From the simulations, we know that the contribution from the lowest order multipoles ($n \leq 2$) occur at longer wavelength when compared to higher order, and thus it seems that for sample-2000-0.5 NP clusters, the dipoles occur at wavelength longer than 900 nm. This could explain the low A_H/A_V ratio obtained in the visible range even though the obtained volume fraction is high (f=0.53).

The increase in forward scattering for a broad range of wavelength, together with a modest value of A_H/A_V, with an increase in volume fraction could be due to the presence of higher order multipoles (refer to Figure 4.2). As explained in Chapter 1, Section 1.2.1 (Figure 1.12), forward scattering is achieved not only due to the overlap of magnetic and electric dipoles (in both spectral position and intensity), but also due to the influence of higher order multipoles. In fact, the influence of higher order multipoles increases the directionality of the scattering pattern (as is the case for PEG-800-4 NP clusters and PEG-2000-2 NP clusters). Thus, the overlap of the amplitudes of dipoles (a_1 and b_1) at longer wavelengths and of multipoles at shorter wavelengths gives rise to a system, which

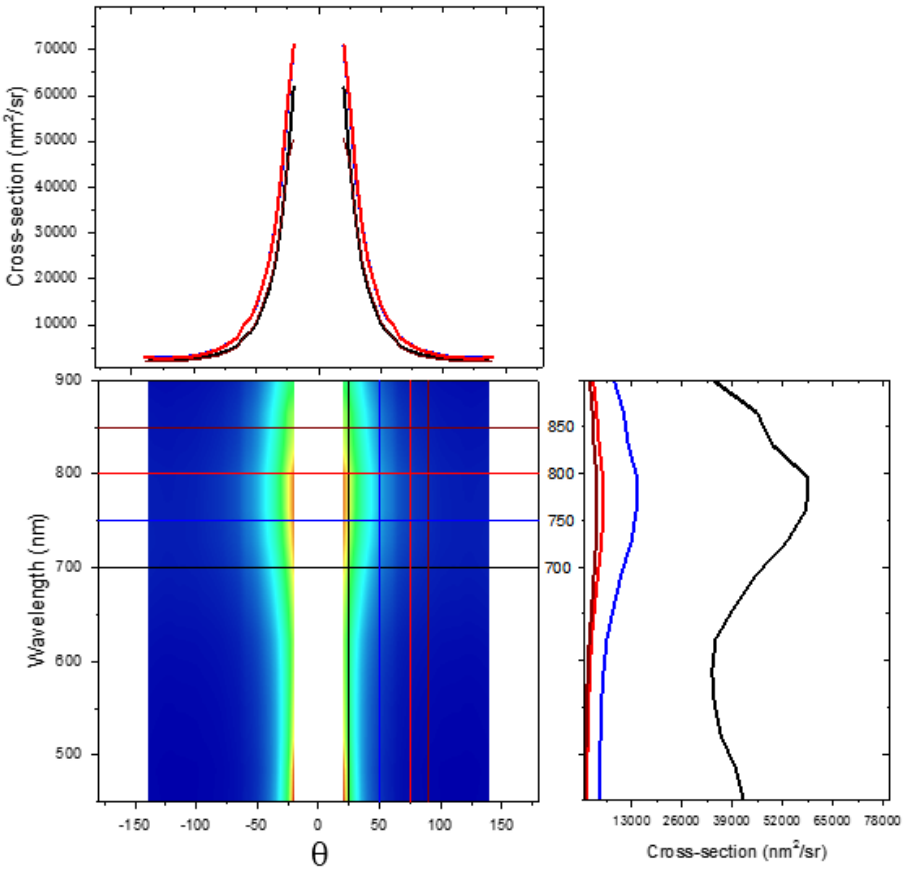

Figure 4.13: Experimental scattering patterns: values of the differential scattering cross-sections ($\sigma_{cluster}$) as a function of the a) wavelength λ and c) the scattering angle θ, for clusters of PEG-2000-0.5 NPs ($f \approx 0.53$). The color code in graph a) is used to indicates the scattering wavelength at λ = 700 (black), 750 (red), 800 (blue) and 850nm (wine red) and in c) the scattering angle at θ = 25 (black), 50 (red), 75 (blue) and 90° (wine red).

exhibits forward scattering for a broad range of wavelengths. In order to confirm this hypothesis, the multipolar contribution to the scattering pattern of the clusters were extracted.

4.1.3 Determination of multipoles

The influence of the higher order multipoles in the scattering pattern of the produced clusters can be witnessed from the polar plots of the respective sample. From Figure 4.12. a. it is evident that with the increase in the volume fraction, a clear increase in the directionality of the scattering pattern is obtained (scattering cross-section decreases drastically with increase in scattering angle). This is especially true at shorter wavelengths. In order to extract the number and orders of multipoles present in the scattering pattern for different samples, the polar plots were fitted to a polynomial function.

From Equation 2.17, we know that the normalized differential cross-section compo-

nents can be written as:

$$\sigma_V = \left\langle \frac{\left|S_1(90°)\right|^2}{k^2} \right\rangle = \frac{1}{k^2}\int_{R_{min}}^{R_{max}} \rho(R)dR \left| \sum_n^{max} (a_n(R)\pi_n(\theta) + b_n(R)\tau_n(\theta)) \right|^2 \tag{4.11a}$$

$$\sigma_H = \left\langle \frac{\left|S_2(90°)\right|^2}{k^2} \right\rangle = \frac{1}{k^2}\int_{R_{min}}^{R_{max}} \rho(R)dR \left| \sum_n^{max} (a_n(R)\tau_n(\theta) + b_n(R)\pi_n(\theta)) \right|^2 \tag{4.11b}$$

where, R is the radius of the clusters, a_n and b_n are the Mie scattering coefficients and $\rho(R)$ is the number density of clusters with a given radius R. Since the clusters are not monodisperse in size, it is considered that the radius are comprised between R_{min} and R_{max}. The angle dependent scattering of the cluster is a series of terms π_n and τ_n, which can be expressed as:

$$\pi_n = \frac{2n-1}{n-1}\mu\pi_{n-1} - \frac{n}{n-1}\pi_{n-2} \tag{4.12a}$$

$$\tau_n = n\mu\pi_n - (n+1)\pi_{n-1} \tag{4.12b}$$

with $\pi_0 = 0$ and $\pi_1 = 1$, and n defines the order of multipole in μ defined as:

$$\mu = Cos\theta \tag{4.13}$$

We call $2n_{max}$, highest multipole taken in the Equation 4.11. From Equation 4.12 it is easy to show that π_n is of order (n-1) in μ and τ_n of order $2n_{max}$, and that we can write:

$$\sigma_V = A_o + A_1\mu + ... + A_{2n}\mu^{2n} \tag{4.14a}$$

$$\sigma_H = B_o + B_1\mu + ... + B_{2n}\mu^{2n} \tag{4.14b}$$

Where, the exponent of μ in the series (Equation: 4.14) can range from 0 to $2n_{max}$ and A_x and B_x depend on the size of the particles.

The order $N = 2n$ should be high enough to fit the experimental data used to produce the polar plots with A_x and B_x as adjustable parameters. From the simulations, we also know that the higher order multipoles occur at lower wavelengths and the dipoles occur at higher wavelengths, therefore the polar plots obtained for different samples at different wavelengths were fitted with different orders of N and the best fit was chosen to determine the order of multipoles.

Here, we represent the fits with an increasing order of multipoles. First, Figure 4.14 represents the fit obtained for sample PEG-6000-2 (f=0.19) for two different wavelengths, λ = 750 nm (a) and 520 nm (b). At λ = 750 nm, excellent fits were obtained by only considering the dipoles and quadrupoles (n = 2). But at shorter wavelengths for the same sample (λ = 520 nm), higher order multipoles (octupole) up to n = 3 had to be included to get a good fit. These fits clearly are in good agreement with the predictions from the simulation which indicated that dipoles contribute more at the longer wavelengths.

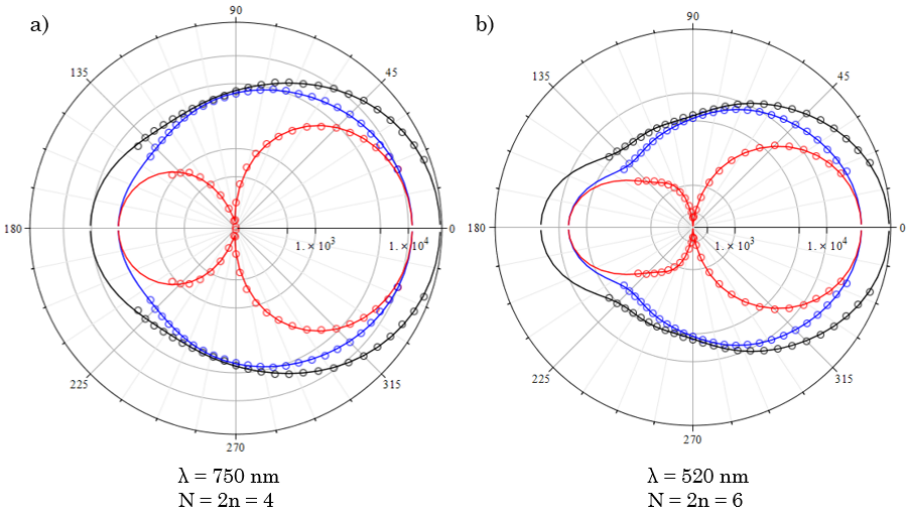

Figure 4.14: Logarithmic plots of experimental scattering patterns: $\sigma_{cluster}$ (black circle), σ_V (blue circles) and σ_H (red circles). Polynomial fit of experimental values : $\sigma_{cluster}$ (black line), σ_V (blue line) and σ_H (red line), Sample PEG-6000-2 at wavelength a) 750 nm and b) 520 nm.

Fitting the experimental data obtained for high volume fraction samples was more complicated than for low volume fraction samples. Indeed, as f increases, an increasing number of multipolar contribution must be taken into account, which introduces more fitting parameters to describe the experimental data. This makes the fits less reliable. Figure 4.15 represents the fit obtained for sample PEG-800-4 (f = 0.46) for two different wavelengths. At λ = 750 nm, a good fit was obtained with n = 3. This fit can be trusted since the number of fitting parameters are reasonably low (14). However at shorter wavelength (λ = 520 nm), the experimental data could only be fitted when N = 12, indicating the presence of multipoles a_n and b_n up to n = 6. This fit is less reliable since the number of fitting parameters (4n+2) used is very high (26). It is hard to differentiate if the obtained fit is good due to the presence of higher order multipoles or to the increase in the number of fitting parameters. This can be improved by introducing more points in the experimental data (specially with measurements >140 °).

Figure 4.15 a also shows a big loop at the backward direction, this is due to the presence of multiple loops in the backward direction for higher order multipoles (as explained in Chapter 1 Figure 1.9 and 1.11). But again, as mentioned above this would need to be confirmed by introducing more points to the experimental data.

It should however be noted that, although in the forward direction we collect data till

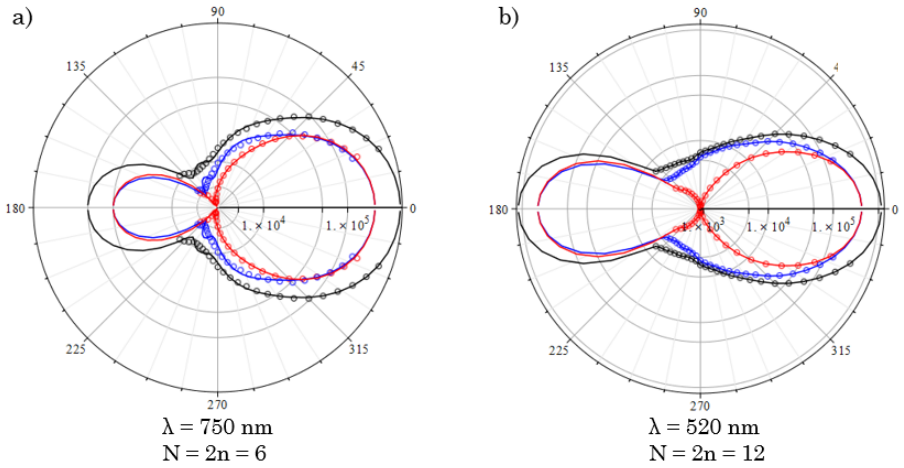

Figure 4.15: Logarithmic plots of experimental scattering patterns: $\sigma_{cluster}$ (black circle), σ_V (blue circle) and σ_H (red circle). Polynomial fit of experimental values : $\sigma_{cluster}$ (black line), σ_V (blue line) and σ_H (red line), Sample PEG-800-4 at wavelength a) 750 nm and b) 520 nm.

20 °, in the backward direction the experimental data is obtained only until 140 °, and including more points in both direction would make the fits shown in Figure 4.15 more reliable. Nevertheless, the increase in multipole order as λ decreases is clearly demonstrated by this approach.

The presence of higher order multipoles not only increases the directionality of the forward scattering pattern, but also broadens the wavelength range for which the forward scattering is obtained. As explained previously in Chapter 1 section 1.2.1, a complete forward scattering occurs when an odd and an even multipole overlap in wavelength and amplitude, and since the multipoles occur at different wavelengths, under right conditions, their overlap leads to forward scattering at different wavelengths. This could explain the broad range of wavelengths for which the forward scattering is obtained in the case of the high volume fraction sample PEG-800-4 (see Fig 4.10) (f=0.46), which is not the case for a low volume fraction sample PEG-6000-2 (f=0.19) (see Figure 4.11).

Finally, to compare the directionality of different samples, the average cos θ value is estimated from the polar plots using the Equation shown below:

$$g = <\cos\theta> = \frac{\sum_{20}^{140} (VH + VV) \sin\theta \cos\theta}{\sum_{20}^{140} (VH + VV) \sin\theta} \tag{4.15}$$

This helps us to determine the asymmetry factor 'g', which can further be used to estimate the wavelength range corresponding to the strong forward scattering. The highest value of g obtained is 0.7 for the two high volume fraction samples, namely PEG-2000-0.5 and PEG-800-4. The presence of loops at the backward direction in the scattering diagram for higher order multipoles explains why the asymmetry factor cannot go higher than 0.7 [8]. These high volume fraction samples behave like Huygens sources with a strong for-

ward scattering property together with a high scattering cross-section (σ).

For most samples (with the exception of gold NPs) the asymmetry parameter is slightly larger at shorter wavelengths. This could be due to the presence of higher order multipoles, which increases the directionality of the scattering pattern. The asymmetry parameter is more or less the same for wavelength ranging from 550 to 750 nm, indicating the broad range of wavelength at which forward scattering is achieved. Once again, it is important to note that the asymmetry parameter is only calculated for experimental data measured from θ = 20 to 140°. By including more points mainly in the backward direction (>140°), the complete asymmetry parameter could be assessed more accurately.

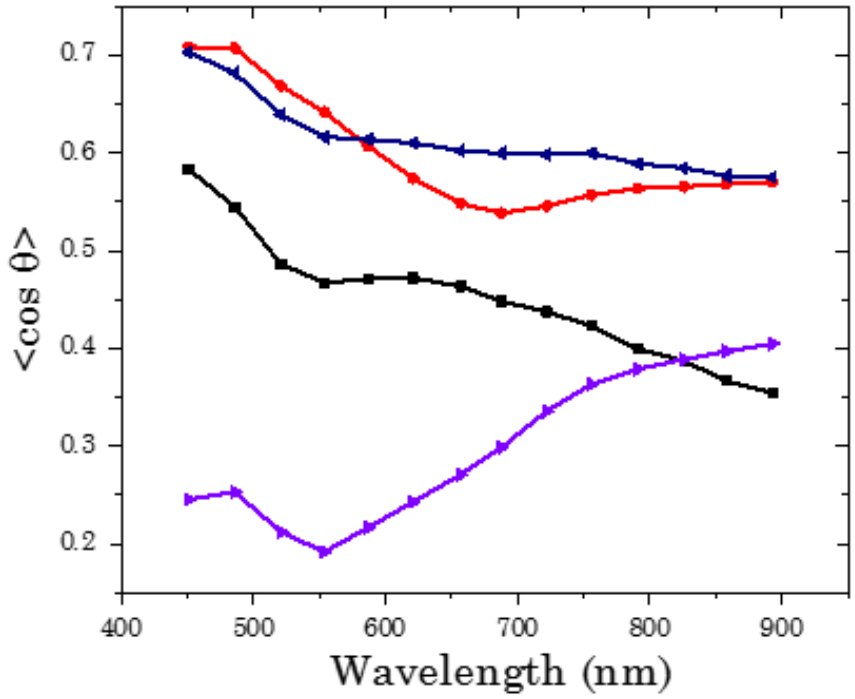

Figure 4.16: Asymmetry factor 'g' for samples PEG-2000-0.5 (Red), PEG-800-4 (dark blue), PEG-2000-2 (black), PEG-6000-2 (pink), PEG-800-4 (R=140 nm)(green),and gold NPs (purple).

4.2 Conclusion

In conclusion, this chapter detailed a new method by using a polarization-resolved multi-angle light scattering setup, to probe the optical scattering patterns of gold NP clusters. We have measured absolute values of the scattering efficiencies on a large assembly of resonators and in a spectrally and angularly resolved manner. This large body of experimental data evidences in particular strong resonant magnetic dipolar responses. We showed the influence of volume fraction f of gold NPs inside the cluster and cluster radius R on their scattering properties.

The differential scattering cross-section of the clusters for different volume fraction

f of gold NPs was calculated. The calculated value for clusters with volume fraction f = 0.46 was approximately 10 times larger than the clusters with volume fraction f = 0.19 at scattering angle $\theta = 20°$. The increase in volume fraction f also led to the broadening of the wavelength range for which forward scattering is achieved.

The experimental data obtained was further used to extract the order of the multipolar contribution to the scattering of the gold Np clusters. The results obtained in this thesis are in good agreement with the simulations and indicate that dense clusters of gold NPs could behave like Huygens sources, with a dominantly forward scattering in the visible wavelength range, making them excellent candidates for functional meta-devices.

4.3 Reference

[1] V. Ponsinet, P. Barois, S. M. Gali, P. Richetti, J.-B. Salmon, A. Vallecchi, M. Albani, A. Le Beulze, S. Gomez-Grana, E. Duguet, *et al.*, "Resonant isotropic optical magnetism of plasmonic nanoclusters in visible light," *Physical Review B*, vol. 92, no. 22, p. 220414, 2015. 106

[2] S. Gómez-Graña, A. Le Beulze, M. Treguer-Delapierre, S. Mornet, E. Duguet, E. Grana, E. Cloutet, G. Hadziioannou, J. Leng, J.-B. Salmon, *et al.*, "Hierarchical self-assembly of a bulk metamaterial enables isotropic magnetic permeability at optical frequencies," *Materials Horizons*, vol. 3, no. 6, pp. 596–601, 2016. 106

[3] V. Many, R. Dézert, E. Duguet, A. Baron, V. Jangid, V. Ponsinet, S. Ravaine, P. Richetti, P. Barois, and M. Tréguer-Delapierre, "High optical magnetism of dodecahedral plasmonic meta-atoms," *Nanophotonics*, vol. 8, no. 4, pp. 549–558, 2019. 106

[4] N. L. Sharma, "Nondipole optical scattering from liquids and nanoparticles," *Physical review letters*, vol. 98, no. 21, p. 217402, 2007. 106

[5] S. Gomez-Graña, M. Treguer-Delapierre, E. Duguet, J. Salmon, J. Leng, V. Kravets, A. Grigorenko, A. Peyyety, V. Ponsinet, P. Richetti, *et al.*, "Isotropic 3d optical magnetism in visible light in a self-assembled metamaterial," in *2016 10th International Congress on Advanced Electromagnetic Materials in Microwaves and Optics (METAMATERIALS)*, pp. 52–54, IEEE, 2016. 107

[6] C. Rockstuhl, F. Lederer, C. Etrich, T. Pertsch, and T. Scharf, "Design of an artificial three-dimensional composite metamaterial with magnetic resonances in the visible range of the electromagnetic spectrum," *Physical review letters*, vol. 99, no. 1, p. 017401, 2007. 108

[7] R. Dezert, P. Richetti, and A. Baron, "Isotropic huygens dipoles and multipoles with colloidal particles," *Physical Review B*, vol. 96, no. 18, p. 180201, 2017. 108

[8] W. Liu, J. Zhang, B. Lei, H. Ma, W. Xie, and H. Hu, "Ultra-directional forward scattering by individual core-shell nanoparticles," *Optics express*, vol. 22, no. 13, pp. 16178–16187, 2014. 123

General conclusion and prospects

The main objective of this thesis was to fabricate resonators which possess directional scattering properties. This was achieved by employing an emulsion based formulation route: a nanoparticles (NPs) suspension is confined into emulsion droplets and dried to produce controlled NP-clusters. A brief insight on the main results and their future perspectives are given below:

Bulk emulsion formulation route:

Results:

- A water-in-oil emulsification route was successfully established to fabricate clusters of gold NPs suspended in dodecane. This two-steps fabrication route proved to be less expensive and less time consuming when compared to techniques such as lithography. This fabrication route allows to produce approximately 10^{12} clusters per 1 liter of dodecane. The structural stability of these clusters was demonstrated using small angle x-ray scattering and electron microscopy.
- The ripening process of the water droplets to form the final clusters was probed using IR spectroscopy, UV-VIS spectroscopy, dynamic light scattering and small angle x-ray scattering. The results clearly indicate that the NPs inside the water droplets do not undergo any uncontrolled aggregation and retain their brownian dynamics until the final stages of the ripening process. In the final stage of the ripening process, the droplet wall forces the NPs to come together to form the clusters.

Outlook:

- In this thesis we mainly focused on water-in-oil emulsions, it could be interesting to fabricate clusters using oil-in-water emulsions. In this case, the final clusters will be suspended in a water phase. The challenge however would be to synthesize the gold NPs in a suitable organic solvent. Hexane would be an ideal choice since its boiling point is lower than water and can therefore be easily ripened at room temperature.
- The formulation route detailed in this thesis can also be adapted to other NPs such as silver or silicon particles. Simulations have shown that such clusters (made of Ag NPs or Si NPs) show promising optical properties.

Droplet based microfluidics:

Results:

- We implemented the droplet based microfluidic technique to potentially improve the results obtained with the bulk emulsion by diminishing the polydispersity of the emulsion droplets size. However, this technique faced many problems starting

from the stability of the emulsions. The surfactants used in the bulk emulsion such as DC 5225 or Hypermer were shown to be inappropriate to stabilize the droplets in the microfluidic channels.

- Even though a stable emulsion was obtained using the surfactant KF 6017 in silicone oil, this system produced very few objects and therefore could not be probed using small angle x-ray scattering and static light scattering. This system also took days to ripen in contrast to the bulk system which merely took 4 hours to ripen completely.

Outlook:

- The microfluidic chips were also used to test the stability of hexane-in-water emulsions. Due to the availability of various surfactants such as sodium dodecyl sulfate (SDS) etc, these emulsions were easily stabilized unlike the water-in-oil emulsions. This serves as a very good alternative to produce a monodisperse suspension of clusters.

- The main advantage of microfluidics over bulk emulsions is its ability to produce monodisperse emulsions which can then be used to produce monodisperse clusters. However, it might be worth to simply try and improve the dispersity of water droplets in the bulk emulsions by using different methods of emulsification such as ultrasonic probes or using a controlled shear geometry (in a Couette cell for example [T.G. Mason, J. Bibette, Phys. Rev. Lett. 77, 3481 (1996)]).

Control over cluster structure

Results:

- We have shown that the gold volume fraction f of the synthesized clusters can be controlled by varying the molar mass or the surface density of the polymer ligands used for the NPs stabilization. In this thesis work, we varied the volume fraction f from 20 to 50 %, which was determined using small angle x-ray scattering. The thickness of the organic layer (polymer ligand) separating the neighboring NPs within the cluster is estimated to vary from 6.9 to 1 nm.

- For this purpose, we used two different polymers namely polyvinylpyrrolidone (PVP) and poly(ehylene glycon) thiols (PEG-SH). Due to the presence of covalent bonds between the gold and PEG-SH molecules, they provide better control against aggregation and over the final f of the gold NP clusters.

Study of optical properties of gold NP clusters

Results:

- We presented an experimental technique to study the angular and spectral light scattering properties of a colloidal suspension of resonators. This technique was used to experimentally demonstrate the influence of the volume fraction f and of the cluster size R on the scattering properties of the clusters. It is shown that dense gold NP clusters with $f \approx 0.46$ and R $\approx$ 120 nm act as strong Huygens sources, with a dominantly forward scattering in the visible wavelength range, making them excellent candidates for functional meta devices.

- The scattering directionality was demonstrated by the angular measurements, which were also used to extract the multipolar contribution to the scattering pattern of the clusters. As predicted by simulations, the contributions from the dipoles occur at longer wavelengths and that of higher order multipoles occur at shorter wavelengths. The number of multipoles contributing to the scattering pattern increased gradually when the volume fraction f of gold NPs within the cluster is increased from 20 to 50 %.

- In addition we estimated the amplitude of the differential scattering cross-section for clusters with three different volume fraction f. The experimental ratio of the differential scattering amplitude in the forward direction (20°) for the two extreme f (0.46 and 0.19) at their respective maximum resonance wavelength is $\approx$ 10, whereas at 90° it is $\approx$ 1.7. This clearly shows the influence of the volume fraction on the directionality of the scattering pattern.

- We have shown that the increasing multipolar contribution to the scattering pattern of the clusters not only improved their forward scattering directionality but also increases the range of wavelength for which the forward scattering is occuring.

Outlook:

- The gold NP clusters analyzed in this thesis work were polydisperse in size R, which made it difficult to compare the experimental results with the simulations. Therefore it could be very interesting to measure the scattering pattern of a monodisperse suspension of these clusters to make a clear comparison with the simulation data. This might be achieved by either producing a monodisperse suspension or by sorting the clusters using techniques such as centrifugation.

- With the increase in the number of multipoles contributing to the scattering pattern of the cluster, the number of fitting parameters used to fit the experimental data also increases, making it difficult to rely on the polynomial fit. This could however be overcome by increasing the range of angles for which the experimental data are obtained.

In summary, in this thesis we established a simple, cost-effective method based on emulsification process to produce a large quantity of gold NP clusters which exhibit very interesting optical properties. This method can also be adapted to produce clusters made of other NPs. Silver and silicon NPs are expected to provide resonant clusters with interesting optical responses.

The next challenge would be to assemble these clusters on a surface to build a metasurface, with phase- and direction-specific scattering. It should be noted that the spatial arrangement of these clusters have to be considered depending upon the application of the metasurface. Simulations performed by Dezert *et al*, have shown that metasurfaces built by arranging plasmonic NP clusters while producing a given spatial organization, can achieve functionalities such as flat prisms and perfect absorption.

The assembly of these clusters to form a metasurface might be possible by applying existing thin film colloid technologies such as Langmuir Blodgett self-assembly, spin coating, dip coating etc. Another interesting possibility is to employ nanopatterned template assisted self-assembly to deposit these clusters on a surface while simultaneously controlling their spatial arrangement.